

RICE UNIVERSITY

**Quantum Plasmonics: A first-principles investigation of
metallic nanostructures and their optical properties**

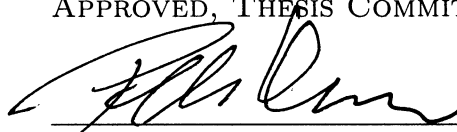
by

Jorge Zuloaga

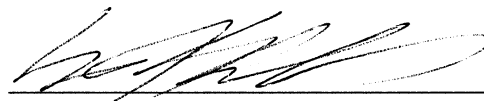
A THESIS SUBMITTED
IN PARTIAL FULFILLMENT OF THE
REQUIREMENTS FOR THE DEGREE

Doctor of Philosophy

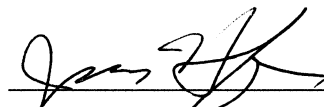
APPROVED, THESIS COMMITTEE:



Peter J.A. Nordlander, *Chair*
Professor of Physics and Astronomy, Pro-
fessor of Electrical and Computer Engi-
neering



Naomi J. Halas
Stanley C. Moore Professor of Electrical
and Computer Engineering, Professor of
Chemistry, Professor of Biomedical Engi-
neering



Jason H. Hafner
Associate Professor of Physics and Astron-
omy, Associate Professor of Chemistry

HOUSTON, TEXAS

AUGUST 2011

ABSTRACT

Quantum Plasmonics: A first-principles investigation of metallic nanostructures and their optical properties

by

Jorge Zuloaga

The electronic structure and optical properties of metallic nanoparticles are theoretically investigated from first principles. An efficient implementation of time-dependent density functional theory allows a fully quantum mechanical description of systems large enough to display collective electron oscillations and surface plasmon modes. The results are compared with traditional classical electrodynamical approaches. Different regimes of interest are identified, both where classical electrodynamical models yield accurate descriptions, and where quantum effects are indispensable for understanding plasmonic properties in nanostructures. The limits of validity of classical electrodynamics are clearly established for the study of a variety of relevant geometries.

ACKNOWLEDGEMENTS

I would like to thank the members of my thesis committee: Peter Nordlander, Naomi Halas, and Jason Hafner. I am exceedingly lucky to have had Peter as my PhD adviser. His contagious enthusiasm for science, and for life, has made graduate school an inspiring and most enjoyable experience. I thank all the members of the Nordlander group for providing a wonderfully helpful and friendly work environment. I am very grateful to my colleague and collaborator, Emil Prodan, from whom I have learned so much. I deeply thank my friends for making life in Houston awfully charming. I also thank my whole family for loving so hard.

My most special gratitude goes to my parents, who still gleefully cheer for me as they did, by the tennis court, when I was a little boy.

To Peri and Lexi.

Contents

Abstract	ii
Acknowledgements	iii
1 Introduction	1
2 Electronic Structure	3
2.1 Density Functional Theory	3
2.2 The Kohn-Sham Equations	5
2.3 Calculating Electronic Structure	7
3 Optical Absorption	17
3.1 Independent electron induced charge density	17
3.2 Total induced charge density	22
4 Single Particle Systems: Nanorods	25
4.1 Optical Absorption	27
4.2 Field Enhancements	30
4.3 Quantum Size Effects	38
4.4 Extrapolation to larger particles	40
5 Dimers	44
5.1 Optical Absorption	47
5.2 Field Enhancements	50

6 Other Geometries	58
6.1 Nanoeggs to Nanocups	59
6.2 Nanomatryoshkas	63
7 Conclusions	72
8 Epilogue	74
8.1 Enhancements are red, absorption is blue, their shift is deciphered and quantified too	74
8.2 The Harmonic Oscillator Model	75
References	85

List of Figures

2.1	Electron density as a function of radius for a gold nanoshell of inner radius 10 Bohr, outer radius 20 Bohr, and a vacuum core.	10
2.2	Electron density as a function of radius for a gold nanoshell of inner radius 10 Bohr, outer radius 20 Bohr, and a vacuum core. The solid black line shows the electron density calculated using the one dimensional procedure for systems with spherical symmetry. The red circles mark the electron density calculated using the two dimensional procedure for systems with azimuthal cylindrical symmetry.	13
2.3	Electron density for a non concentric gold nanoshell with a vacuum core. The core radius is 12 Bohr, the shell radius is 24 Bohr, and the core is displaced 9 Bohr from the center.	14
2.4	Electron density for an $R = 24$ Bohr sphere dimer. The separation distance is 5 Bohr.	15
2.5	Effective Kohn-Sham potential $U_{KS}(\vec{r})$ for an $R = 24$ Bohr sphere dimer. The separation distance is 5 Bohr.	16
4.1	Optical absorption spectra calculated using TDDFT for nanorods of different aspect ratios ζ . The top panel shows the longitudinal mode for nanorods with $\zeta = 3, 2.5, 2, 1.5, 1.2, 1.1$, and 1 with the labeling going from left to right. The bottom panel shows the transverse mode for the same ζ , but with a labeling from right to left. The length b of the nanorod is scaled so that each nanorod contains the same number of electrons (510). The spectra have been normalized to the cross sectional area of the nanorod.	29

4.2	Longitudinal and transverse dipolar plasmon energies of a silver nanorod as a function of inverse aspect ratio $1/\zeta$ for the nanorods discussed in Fig. 4.1. The TDDFT results are shown in blue and the classical electromagnetic results obtained using an equivalent dielectric permittivity for Ag are shown in black.	31
4.3	The upper graph shows a comparison of the maximum electromagnetic field enhancements calculated using classical electromagnetic theory (red) and TDDFT (blue) for a nanorod as a function of ζ . The lower panels compare the field distributions calculated using classical electromagnetic theory (top panels) and TDDFT (bottom panels) for $\zeta = 1$ (A), $\zeta = 1.5$ (B), $\zeta = 2$ (C), and $\zeta = 3$ (D). The field enhancements were calculated for the resonant frequency of the longitudinal dipolar plasmon using a broadening of $\delta = 0.27$ eV. The overall size b of each nanorod has been adjusted so it contains 510 electrons.	33
4.4	Electric field enhancements as a function of distance d from the particle tip for an aspect ratio of $\zeta=1$ (top) and $\zeta=3$ (bottom). The classical calculations are shown with red lines and the TDDFT results are shown with black lines.	35
4.5	(A) Equilibrium electron density calculated using TDDFT as a function of distance from the particle surface along the long axis for nanorods of aspect ratios $\zeta = 1$ (blue curve) and $\zeta = 3$ (red curve), and perpendicular to the long axis for nanorods of $\zeta = 3$ (black curve). (B) Induced screening charge calculated using TDDFT as a function of distance from the particle surface along the long axis for nanorods of aspect ratios $\zeta = 1$ (blue curve) and $\zeta = 3$ (red curve), and perpendicular to the long axis for nanorods of $\zeta = 3$ (black curve). The insets show the definitions of the coordinate d	37
4.6	Top panel: Absorption spectra calculated using TDDFT for five nanorods of the same aspect ratio ($\zeta = 3$) but different major axis b : 17 Bohr (19 electrons), 20 Bohr (63 electrons), 33 Bohr (151 electrons), 42 Bohr (294 electrons), and 50 Bohr (510 electrons) from bottom to top. The absorption spectra have been scaled so the absorption maxima are the same for each nanorod. Bottom panel: Plasmon-induced electric field enhancements for the $b=17$ Bohr (A), 33 Bohr (B), and 50 Bohr (C) nanorods.	39

4.7	Electromagnetic field enhancements as a function of $\hat{d} = d/b$ along the rod axis for rods of $\zeta = 3$. The dashed line represents the scale-invariant classical result. The solid lines show the quantum mechanical results for rods of different sizes: 19, 63, 151, 294, 882, and 2171 electrons (from bottom curve and up).	42
5.1	Equilibrium electron density (left) and self-consistent effective Kohn-Sham potential (right) for a nanosphere dimer of sphere radii $R = 12$ Bohr and interparticle separation $d = 1$ Bohr.	53
5.2	TDDFT absorption spectra for the $R=16$ Bohr (upper panel) and $R=24$ Bohr (lower panel) for different separations $d=0, 1, 2, 3, 4, 5, 6, 7, 8, 10, 16$ and 24 Bohr (from bottom curve and up). The spectra were calculated using an energy broadening of $\delta=0.27$ eV.	54
5.3	The dipolar (full circles) and quadrupolar (open circles) dimer plasmon energy as a function of d/R for of $R=16$ Bohr (red) and 24 Bohr (blue) sphere dimers calculated using TDDFT. The PH result is shown with solid (dipolar) and dashed (quadrupolar) lines.	55
5.4	The self-consistent effective Kohn-Sham potential U_{KS} (upper row) and electron charge density $n(z)$ (lower row) along the symmetry axis, for $R=24$ Bohr and $d=16$ (left), 5 (middle) and 2 Bohr (right). The red horizontal lines mark the Fermi level. The solid horizontal lines are the energies of the the 60th and 30th occupied state below the Fermi energy. The dashed horizontal lines are the energies of the 30th and 60th unoccupied states above the Fermi level.	56
5.5	The upper panel show a comparison of the maximum electromagnetic field enhancements calculated using PH (red) and TDDFT (blue) for $R=24$ Bohr dimers of separations $d=24$ (A), 8 (B), 4 (C) and 2 Bohr (D). The lower panels compares the field distributions calculated using PH (top panels) and TDDFT (bottom panels). The field enhancements were calculated for resonant excitation of the dipolar dimer plasmon using a broadening of $\delta=0.27$ eV.	57
6.1	Calculated electron density for a nanoshell to nanoegg to nanocup transition. We start with a perfectly concentric nanoshell of inner radius 12 Bohr and outer radius 24 Bohr and gradually increase the core displacement: $d = 0, 9, 14, 27$ (from left to right).	66

6.2	Lowest plasmon energy as a function of core displacement parameter $d/(R_{out} - R_{in})$ for a core-shell particle with outer radius $R_{out} = 24$ Bohr, inner radius $R_{in} = 12$ Bohr, and a vacuum core. The excitation polarization is aligned with the azimuthal axis of symmetry of the particles. The number of electrons in the particle ranges from 444 for the $d = 0$ concentric nanoshell to 507 for $d = 36$ solid sphere. The red curve shows the classical calculations and the blue curve shows the quantum results.	67
6.3	Electromagnetic field enhancements as a function of core displacement parameter D for a core-shell particle with outer radius 24 Bohr and core radius 12 Bohr. The red curve shows the classical calculations and the blue curve shows the quantum results. The enhancements are plotted for a point 0.5 Bohr outside the particle surface in the direction of core displacement.	68
6.4	Optical Absorption (left panels) and field enhancements (right panels) as a function of frequency for core-shell particles with core displacement $d = 0$ (top), $d = 6$ (middle), and $d = 10$ (bottom). The quantum results are shown in black and the classical results are shown in red.	69
6.5	Field enhancements for a core-shell particle with outer radius 24 Bohr, core radius 12 Bohr, and core displacement of $d = 0$ Bohr (left panels) and $d = 10$ Bohr (right panels). The top panels show the classical results and the bottom panels show the quantum results.	70
6.6	Schematic illustration of a nanomategyoshka. This particle consists of a metallic sphere surrounded by a dielectric layer, which in turn is surrounded by a spherical metallic shell.	71
6.7	Calculated electron density (left panels) and optical absorption spectra (right panels) for nanomategyoshkas of size $(r_c, R_{s1}, R_{s2})/\lambda = (14, 18, 24)/\lambda$ Bohr, for $\lambda = 1, 2, 3$	71
8.1	Mie extinction cross section (blue curve) and NFE (black curve) as a function of energy for a 12 nm radius gold (DM) sphere. Both spectra have been normalized to unity.	79

-
- 8.2 Mie extinction spectra (blue) and NFE (black) as a function of energy for a 150 nm radius gold (DM) sphere. The fit of the far-field peak to Eq. (8.7) is shown in red. The vertical black and blue lines denote the peak positions in the near-field and far-field spectra, respectively. The red dashed line denotes the energy ω_{NF} obtained using Eq. (8.5). The spectra have been normalized to unity. 80
- 8.3 Extinction cross section (blue) and NFE (black) as a function of energy for a metallic nanorod of aspect ratio 3 for longitudinal polarization (left panels) and transverse polarization (right panels). DMs with artificially large damping are used: $\gamma = 2$ (top panels), $\gamma = 4$ (bottom panels). The fits of the far-field peaks to Eq. (8.7) are shown in red. The vertical black and blue lines denote the peak positions for the calculated near-field and far-field, respectively. The red dashed lines denote the energy ω_{NF} obtained using Eq. (8.5). The spectra have been normalized to unity. 82
- 8.4 Mie extinction spectra (blue) and NFE (black) as a function of energy for a gold (DM) nanoshell of inner radius 75 nm and outer radius 150 nm. The fits of the far-field peak to Eq. (8.7) are shown in red. The vertical black and blue lines denote the near-field and extinction peak energies, respectively. The red dashed line denote the energy ω_{NF} obtained using Eq. (8.5) The spectra have been normalized to unity. 83

Introduction

The fascinating optical properties of metallic nanoparticles have captured the interest of people since antiquity. [1] In recent years, large research efforts have yielded a more fundamental understanding of nanophotonics. [2] It is now well established that the optical properties of metallic nanoparticles are determined by the collective oscillations of their conduction electrons, known as plasmon resonances. [3, 4] This plasmonic response of nanoparticles has often been found to be accurately described by classical electrodynamics. [5, 6, 7, 8] Theoretical investigations based on first-principles calculations have confirmed that the plasmon resonances in simple single-particle systems are in good agreement with classical electrodynamic calculations and experimental results. [9, 10] More recent *ab initio* studies [11] have shown, however, that electromagnetic field enhancements near particle surfaces may be significantly screened by realistic electron density distributions at the interface between a metal and the surrounding medium. Moreover, in geometries where two metallic surfaces are in close proximity to each other, quantum effects such as electron tunneling and screening, may drastically reduce electromagnetic field enhancements and significantly modify plasmon resonant frequencies. [12] These important effects are neglected by purely classical descriptions of plasmonic particles based on discontinuous

dielectric models at particle-medium interfaces.

The objective of this work is to provide a thorough first-principles investigation of a variety of metallic nanostructure geometries of interest. Electronic structure and optical properties are described within a fully quantum mechanical framework, and the results are compared with classical electrodynamical predictions. In chapter 2 we elaborate on the formalism used for electronic structure calculation. Chapter 3 discusses the theory of electronic linear response, which is used for the investigation of nanoparticle optical properties. Chapters 4, 5, and 6 are devoted to the detailed study of different nanoparticle geometries of interest.

Electronic Structure

In this chapter we describe the theoretical formalism used to investigate the electronic structure of nanoparticles. We present a general overview of the theory, followed by a discussion of how it is applied to the systems we are interested in. We then develop the formalism in a framework that is appropriate for particles with different symmetries. The chapter concludes with examples of applications and calculations of electronic structure for different nanostructure geometries.

2.1 Density Functional Theory

Density functional theory (DFT) is a variational formulation of quantum mechanics that is particularly useful for the study of the electronic structure in condensed matter physics. In the Schrödinger picture, the many-body problem for a general N -electron system subject to an external potential V_{ext} , is described by the many-electron time-independent Schrödinger equation

$$\hat{H}\Psi = - \left[\sum_i^N \frac{\hbar^2}{2m} \nabla_i^2 + \sum_i^N eV_{ext}(\vec{r}_i) - \frac{1}{2} \sum_{i \neq j}^N \frac{e^2}{|\vec{r}_i - \vec{r}_j|} \right] \Psi = E\Psi. \quad (2.1)$$

The third summation in the Hamiltonian, which describes the electron-electron interactions, makes the numerical solution of the problem nontrivial. This computational obstacle is circumvented by the key insight of density functional theory, which is contained in the Hohenberg-Kohn theorems.[13] These theorems place the theory in firm theoretical footing by guaranteeing the existence of an effective, position dependent, single-particle potential V_{eff} that captures the dynamics of electron interactions. In other words, the potential energy term in the many-electron Schrödinger equation (2.1) may be described by a single-particle effective potential with which electrons interact individually. The problem is then cast as a system of non interacting particles:

$$-\left[\sum_i^N \frac{\hbar^2}{2m} \nabla_i^2 + \sum_i^N eV_{eff}(\vec{r}_i) \right] \Psi = E\Psi, \quad (2.2)$$

where the equation becomes separable. We may now write the many-electron wave function as a product of single-electron wave functions

$$\Psi(\vec{r}_1, \vec{r}_2, \dots, \vec{r}_N) = \psi(\vec{r}_1)\psi(\vec{r}_2)\cdots\psi(\vec{r}_N), \quad (2.3)$$

and the total energy of the system as a sum of N single-electron energies

$$E = \epsilon_1 + \epsilon_2 + \cdots + \epsilon_N. \quad (2.4)$$

Substituting (2.3) and (2.4) into (2.2) and dividing by $\Psi = \psi(\vec{r}_1)\psi(\vec{r}_2)\cdots\psi(\vec{r}_N)$ we find that the many-electron Schrödinger equation is satisfied if N single-electron Schrödinger equations of the form

$$\left[-\frac{\hbar^2}{2m} \nabla_i^2 - eV_{eff}(\vec{r}_i) \right] \psi(\vec{r}_i) = \epsilon_i \psi(\vec{r}_i), \quad (2.5)$$

are satisfied. For this work, atomic units will be used and we will have $\hbar = m = e = 1$.

2.2 The Kohn-Sham Equations

We have now seen that we may transform one N -electron Schrödinger equation into N single-electron equations. This is one of the most useful formulations of density functional theory. Calculating the electronic structure of a many-body system amounts to solving the corresponding Kohn-Sham equations:[14]

$$-\frac{1}{2}\nabla^2\psi_i(\vec{r}) + U_{KS}(\vec{r})\psi_i(\vec{r}) = \epsilon_i\psi_i(\vec{r}), \quad (2.6)$$

where ψ_i and ϵ_i are the single-electron wavefunctions and eigen energies, respectively, and U_{KS} is the effective Kohn-Sham potential under which the single electrons move. The electron density of the system is calculated from the single-electron wavefunctions:

$$n(\vec{r}) = 2 \sum_i \frac{|\psi_i|^2}{1 + e^{\beta(\epsilon_i - \mu)}}. \quad (2.7)$$

The term $1/(1 + e^{\beta(\epsilon_i - \mu)})$ in eq. (2.7) is the occupation number of a Fermi gas at finite temperature T for energy ϵ_i . The temperature T is given by $\beta = 1/kT$. The effective Kohn-Sham potential U_{KS} under which the single electrons move is a functional of the electron density $n(\vec{r})$:

$$U_{KS}(\vec{r}) = V_0(\vec{r}) + V_H[n(\vec{r})] + V_{xc}[n(\vec{r})], \quad (2.8)$$

which includes a background pseudo-potential V_0 , the Hartree electrostatic potential V_H , and the exchange-correlation potential V_{xc} . The background pseudo-potential is an important quantity in calculating the electronic structure for metallic nanoparticles, where it is essential that the ionization potential of the metal match the known value of the metallic work function. The background pseudo-potential V_0 is chosen to be zero outside the particle and with a constant value $-v_0$ ($v_0 > 0$) inside the particle.

The value v_0 is adjusted to yield the correct value for the metallic work function.

The electronic structure of the system is calculated by self-consistently solving eqs. (2.6)-(2.8). In dealing with electrons moving under the influence of the positive ions in a metal, calculations are often done via the so-called jellium approximation, where the discrete positive ions are modeled by a continuous, uniform positive charge. Since the optical properties of a metallic nanoparticle are determined by the conduction electrons, we expect the jellium model to provide an accurate description. Previously, jellium models of shell structures have been successfully used for the investigation of the electronic structure of C_{60} and other fullerene systems. [15] Jellium models have also been widely used to model small metallic clusters. [16, 17] The numerical simplifications enabled by the jellium model are significant and allow the study of nanoparticles sufficiently large to have a fully developed plasmon mode. [12]

When calculating the electronic structure of a nanoparticle in the jellium model, the Hartree potential in eq. (2.8) takes the form:

$$V_H(\vec{r}) = \int \frac{n(\vec{r}') - n_0(\vec{r}')}{|\vec{r} - \vec{r}'|} d\vec{r}', \quad (2.9)$$

where $n(\vec{r})$ is the electron density given from eq. (2.7) and $n_0(\vec{r})$ is the positive pseudo-ionic charge taken to be zero outside the particle and with uniform density $n_0 = 3/(4\pi r_s^3)$ inside the particle. The appropriate charge density is chosen for the metal of interest by using the Wigner-Seitz radius r_s of the metal.

The exact form of the exchange-correlation potential V_{xc} in eq. (2.8) is given by the functional derivative of the exchange-correlation energy functional:

$$V_{xc}[n(\vec{r})] = \frac{\delta E_{xc}[n(\vec{r})]}{\delta n(\vec{r})}. \quad (2.10)$$

While an exact form of the energy functional $E_{xc}[n(\vec{r})]$ exists, it is not known. [13]

Approximating the form of E_{xc} is the ultimate source of error in the method. [18] This error, however, is especially small when considering the ground-state of the many-electron system. [19] For this work, we will work in the local density approximation (LDA), [14] where the exchange-correlation energy of a nonuniform electron gas of slowly varying density $n(\vec{r})$ is presumed to be

$$E_{xc}[n(\vec{r})] = \int \epsilon_{xc}[n(\vec{r}')]n(\vec{r}')d\vec{r}', \quad (2.11)$$

with ϵ_{xc} being the exchange-correlation energy per particle for a homogeneous system with density $n(\vec{r})$. V_{xc} can then be directly calculated through eq. (2.10). The final form obtained for V_{xc} is the Perdew-Zunger LDA exchange-correlation potential [20]:

$$V_{xc}(r_s) = \begin{cases} -\frac{0.611}{r_s} + 0.03109 \log r_s - 0.0584 \\ \quad + 0.0013r_s \log r_s - 0.007r_s & \text{if } r_s < 1. \\ -\frac{0.611}{r_s} - \frac{0.1423(1+1.23\sqrt{r_s}+0.445r_s)}{(1+1.1592\sqrt{r_s}+0.3334r_s)^2} & \text{if } r_s > 1. \end{cases}$$

2.3 Calculating Electronic Structure

We are interested in calculating the electronic structure of metallic nanoparticles. This problem has been reduced to self-consistently solving eqs. (2.6)-(2.8). The main computational challenge is to solve the single-electron Schrödinger equation (2.6) for the geometry of interest. A general solution for three dimensional geometries is extremely expensive computationally, but exploiting symmetry may lead to significant simplifications of the problem. In this section we look at special cases where symmetry reduces the number of computational dimensions.

2.3.1 Particles with spherical symmetry

For the special case of particles with spherical symmetry, the computational problem becomes one-dimensional. In a spherically symmetric system, U_{KS} in eq. (2.6) has no angular dependence, and the single-electron Schrödinger equation can be written

$$-\frac{1}{2}\nabla^2\psi + U_{KS}(r)\psi_i = \epsilon_i\psi_i. \quad (2.12)$$

Separating variables we let $\psi(r, \theta, \phi) = R(r)Y(\theta, \phi)$ and write eq. (2.12) as

$$\begin{aligned} -\frac{1}{2r^2}\frac{\partial}{\partial r}\left(r^2\frac{\partial}{\partial r}(RY)\right) - \frac{1}{2r^2\sin\theta}\frac{\partial}{\partial\theta}\left(\sin\theta\frac{\partial}{\partial\theta}(RY)\right) \\ - \frac{1}{2r^2\sin^2\theta}\frac{\partial^2}{\partial\phi^2}(RY) + U_{KS}(r)RY = \epsilon(RY). \end{aligned} \quad (2.13)$$

We may separate (2.13) into an angular equation and a radial equation. For convenience we use a separation constant equal to $l(l+1)$. The angular equation is independent of the effective potential $U_{KS}(r)$ and introduces another quantum number m as a separation constant for the variables θ and ϕ . Its solutions are the well known spherical harmonics:

$$Y_l^m(\theta, \phi) = Ae^{im\phi}P_l^m(\cos\theta). \quad (2.14)$$

The radial equation depends on the effective Kohn-Sham potential:

$$\frac{d}{dr}\left(r^2\frac{dR}{dr}\right) - 2r^2(U_{KS}(r) - \epsilon)R = l(l+1). \quad (2.15)$$

Using the change of variable $u(r) \equiv rR(r)$, the radial equation is often written as

$$\left[-\frac{1}{2}\frac{d^2}{dr^2} + U_{KS}(r) + \frac{l(l+1)}{2r^2}\right]u_n = \epsilon_n u_n. \quad (2.16)$$

For any quantum numbers l and m , and for any energy ϵ_n , we then have that the Schrödinger equation (2.12) is satisfied by a wave function of the form

$$\psi_{nlm}(r, \theta, \phi) = R_{nl}(r)Y_{lm}(\theta, \phi). \quad (2.17)$$

The computational Kohn-Sham problem is then reduced to solving the one-dimensional eq. (2.16) self-consistently with eqs. (2.7) and (2.8).

An interesting plasmonic nanoparticle with spherical symmetry is the so-called nanoshell, [21] consisting of a dielectric spherical core surrounded by a metallic shell. [22, 23, 24, 25] The interest in these particles lies in their exceptional tunability: by varying the ratio of the shell thickness with respect to the overall diameter of the particle, the plasmon frequencies of the nanoshells can be placed at arbitrary wavelengths between the mid infrared and the UV region of the optical spectrum. [6, 7, 8] The exceptional tunability of these particles has been experimentally verified [26] and makes them particularly attractive for applications that include Raman sensors, [27] environmental sensors, [28] drug delivery implants, [29] optical triggers for opto-mechanical materials, [30] and photo-oxidation inhibitors. [31]

With the computational procedure described above we are able to calculate the electronic structure of nanoshells of large enough size to exhibit fully developed plasmon modes. The optical response of nanoshells has been previously studied from first principles [32]. Such studies reveal good agreement with experimental results, supporting the assumption that the jellium approximation captures the physics at the optical and infrared frequencies studied. [33] The calculated electron density for a gold nanoshell of inner radius 10 Bohr, outer radius 20 Bohr, and a vacuum core is plotted in Fig. 2.1.

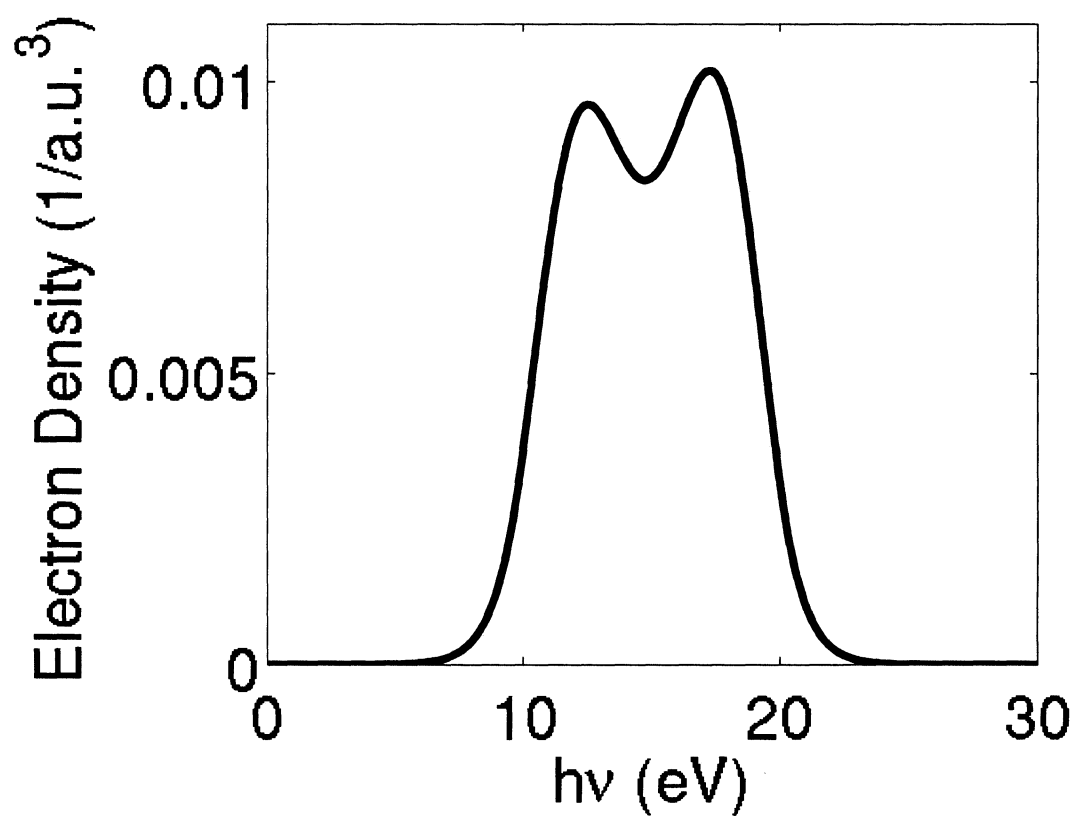


Figure 2.1: Electron density as a function of radius for a gold nanoshell of inner radius 10 Bohr, outer radius 20 Bohr, and a vacuum core.

2.3.2 Particles with cylindrical symmetry

Recent innovations in experimental techniques allow the fabrication of new nanoparticles with novel plasmonic properties. Some of these particles include nanorods, [34, 35, 36, 37, 38, 39, 40, 41] nanoeggs (nanoshells with an off-centered core), [42] nanocups, [43, 44, 45, 46] nanoparticle dimers, [47, 48, 49, 50, 51] nanowires, [52, 53, 54, 55, 56] and nanorice (metallic nanorods with dielectric cores), [57, 58, 59] all of which possess cylindrical azimuthal symmetry. While it is desirable to theoretically investigate the optical properties of such particles from first principles, the Kohn-Sham equations for particles of cylindrical symmetry become a two-dimensional problem of significantly more computational complexity than the one-dimensional problem appropriate for spherically symmetric particles. One of our goals was to extend this DFT approach to cases where the symmetry of the system is azimuthal. Here we present the mapping of the problem into cylindrical symmetry.

When doing electronic structure calculations for particles with cylindrical symmetry, U_{KS} in eq. (2.6) has no azimuthal dependence. In cylindrical coordinates we write $U_{KS} = U_{KS}(\rho, z)$, and the azimuthal dependence of the single-electron wave functions can be separated out: $\psi_{nm}(\rho, \phi, z) = \tilde{\psi}_{nm}(\rho, z)e^{im\phi}$. The single-electron Schrödinger equation (2.6) may then be written

$$\left[-\frac{1}{2}\nabla^2 + \frac{m^2}{2\rho^2} + U_{KS}(\rho, z) \right] \tilde{\psi}_{nm}(\rho, z) = \epsilon_{nm}\tilde{\psi}_{nm}(\rho, z). \quad (2.18)$$

By making the change of variable $\phi(\rho, z) = \sqrt{\rho}\tilde{\psi}(\rho, z)$, we may write this equation as

$$\left[-\frac{1}{2}\frac{\partial^2}{\partial\rho^2} - \frac{1}{2}\frac{\partial^2}{\partial z^2} + \frac{(m^2 - 1/4)}{2\rho^2} + U_{KS}(\rho, z) \right] \phi_{nm} = \epsilon_{nm}\phi_{nm}. \quad (2.19)$$

Now the Kohn-Sham problem consists of solving the two-dimensional single-electron Schrödinger equation (2.19) self-consistently with eq. (2.7) and (2.8).

As a first application and test, we use this generalized procedure for azimuthally symmetric systems to calculate the electron density of a spherically symmetric nanoshell. In Fig. 2.2 we plot the electron density as a function of radius for a gold spherical nanoshell of inner radius 10 Bohr and outer radius 20 Bohr. The electron density calculated with the one-dimensional approach for spherical systems is denoted with the solid black line. The red circles mark the density calculated with the generalized approach for azimuthally symmetric systems. The calculated electron densities from both approaches are in agreement.

We now exploit the generalized approach for azimuthally symmetric systems to calculate the electron density for other systems of interest that lack spherical symmetry. Fig. 2.3 shows the calculated electron density $n(\vec{r})$ for a gold nanoegg (non concentric shell) with core radius 12 Bohr, shell radius 24 Bohr, and core displacement of 9 Bohr. The figure reveals the expected oscillatory behavior of the electron density inside the particle due to Friedel oscillations. [32] It is also clear that, in the narrow metal strip produced by the proximity of the inner core to the outer shell, the electron density is reduced due to confinement effects. These important quantum effects are will prove to be crucial in understanding the optical properties of such systems.

As another example of an important cylindrically symmetric geometry that can be studied with the approach mentioned above, in Fig. 2.4 we plot the electron density for a gold sphere dimer. The radius of the particles is 24 Bohr and their separation distance is 5 Bohr, so there is no significant overlap in their electron densities, but the figure reveals the expected Friedel oscillations inside the particles. The effective Kohn-Sham potential for these particles is plotted in Fig. 2.5. As has been mentioned above, in the Kohn-Sham formulation of the problem, the electrons behave as non-interaction particles, all subject to this position-dependent effective potential.

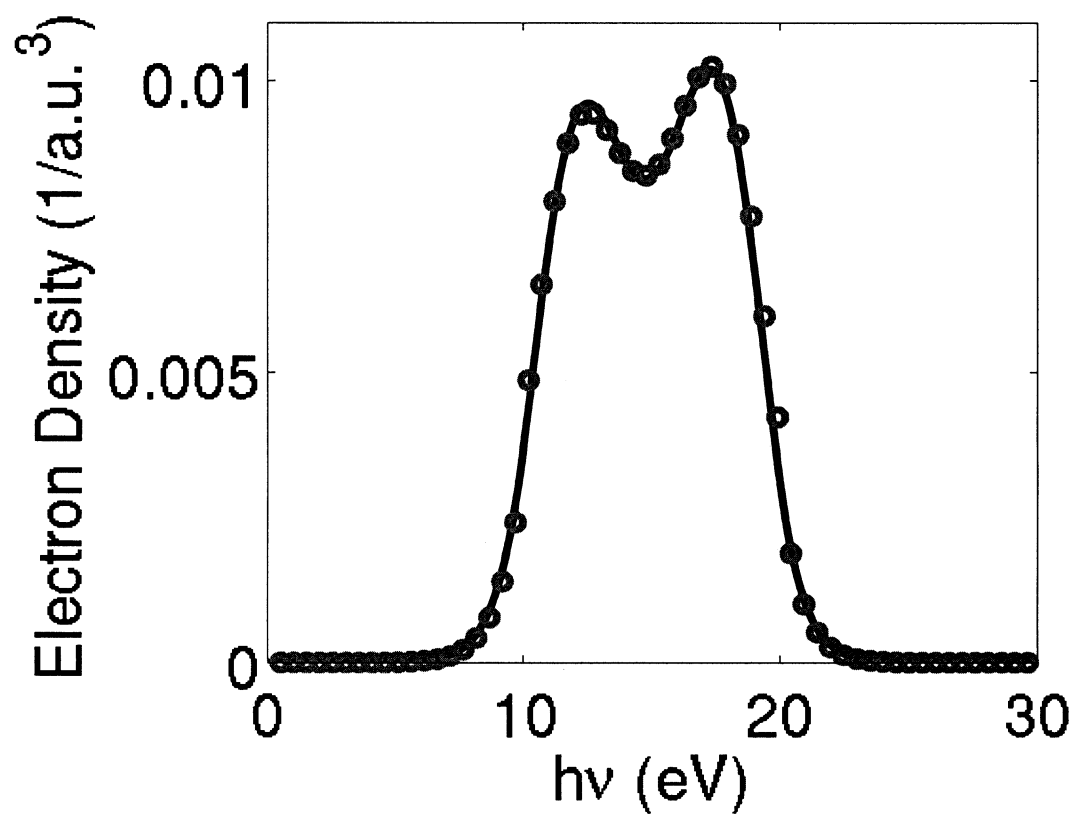


Figure 2.2: Electron density as a function of radius for a gold nanoshell of inner radius 10 Bohr, outer radius 20 Bohr, and a vacuum core. The solid black line shows the electron density calculated using the one dimensional procedure for systems with spherical symmetry. The red circles mark the electron density calculated using the two dimensional procedure for systems with azimuthal cylindrical symmetry.

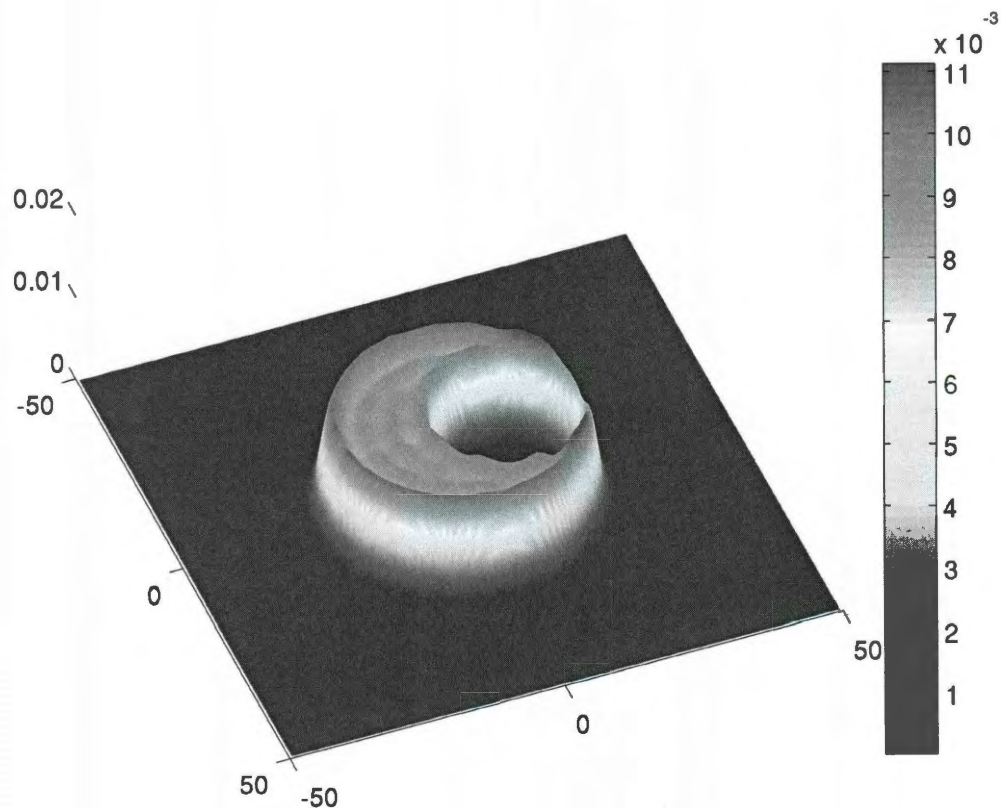


Figure 2.3: Electron density for a non concentric gold nanoshell with a vacuum core. The core radius is 12 Bohr, the shell radius is 24 Bohr, and the core is displaced 9 Bohr from the center.

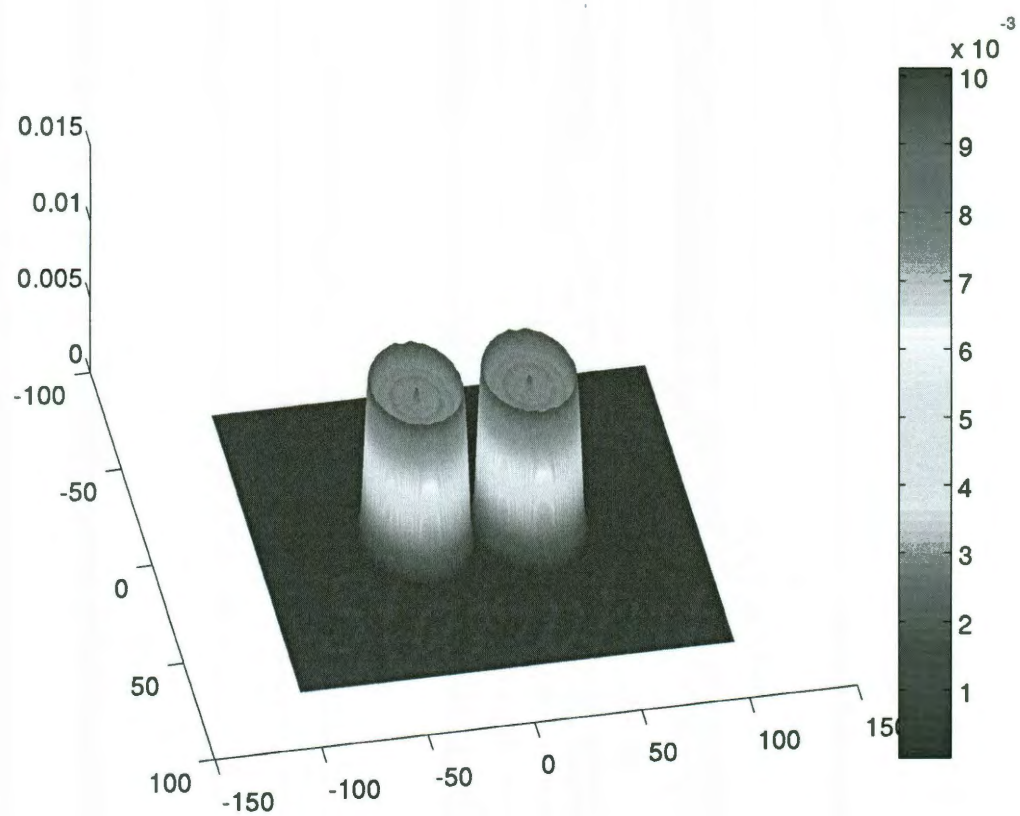


Figure 2.4: Electron density for an $R = 24$ Bohr sphere dimer. The separation distance is 5 Bohr.

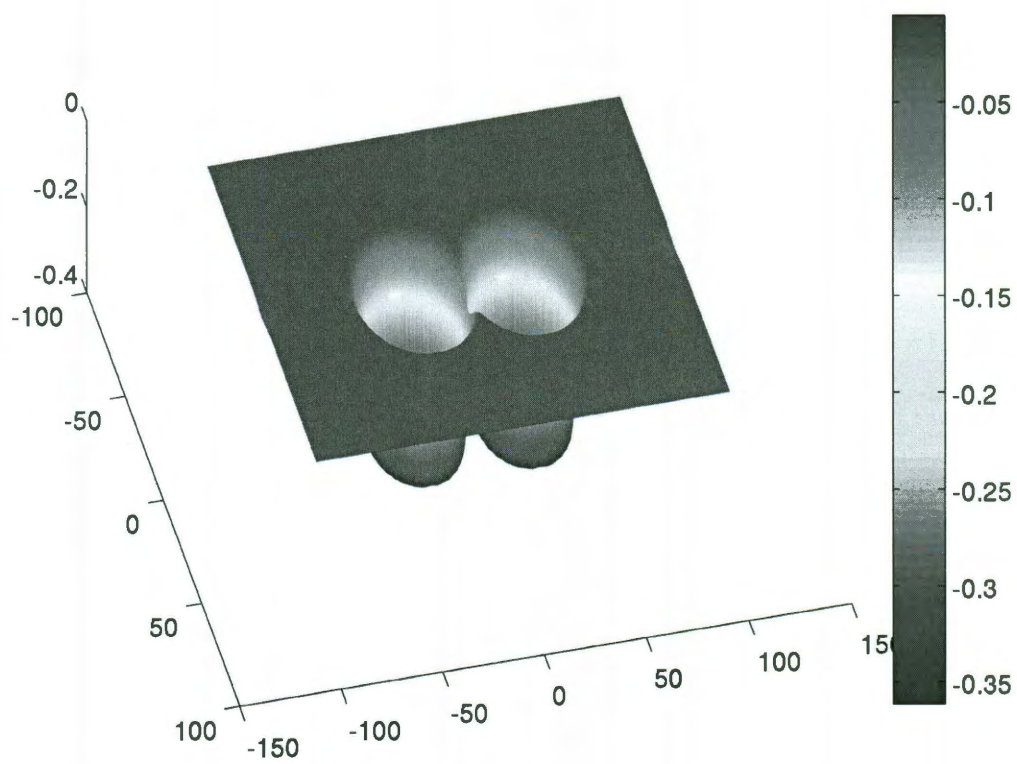


Figure 2.5: Effective Kohn-Sham potential $U_{KS}(\vec{r})$ for an $R = 24$ Bohr sphere dimer. The separation distance is 5 Bohr.

Optical Absorption

Having calculated the equilibrium electron density for a nanostructure, we now study the linear response of the electrons to external perturbations. In this chapter we elaborate on how the theory of linear response is used to calculate induced charge density in nanoparticles. This allows us to calculate the optical absorption.

3.1 Independent electron induced charge density

The frequency dependent optical absorption calculation was completed within time-dependent density functional theory (TDDFT). For the independent electrons, the linear response equation for the frequency dependent induced density perturbation is given by:

$$\delta n^0(\vec{r}, \omega) = \int d\vec{r}' \chi^0(\vec{r}, \vec{r}'; \omega) V_{ext}(\vec{r}', \omega), \quad (3.1)$$

where $\chi^0(\vec{r}, \vec{r}'; \omega)$ is the independent electron density-density correlation function and $V_{ext}(\vec{r}, \omega)$ is the external driving potential. The independent electron density-density correlation function has an exact expression in terms of the single-electron Kohn-Sham

orbitals obtained from the equilibrium electronic structure calculation (Eq. 2.5):

$$\chi^0(\vec{r}, \vec{r}'; \omega) = \sum_{i,j} (f_i - f_j) \frac{\psi_i(\vec{r}') \psi_i^*(\vec{r}) \psi_j^*(\vec{r}') \psi_j(\vec{r})}{\hbar\omega - (\epsilon_j - \epsilon_i) + i\delta}, \quad (3.2)$$

where f_i represents the finite temperature occupation number of the i^{th} state. We can rewrite (3.2) as

$$\begin{aligned} \chi^0(\vec{r}, \vec{r}'; \omega) &= \sum_{\substack{i \\ \text{occ}}} \psi_i(\vec{r}') \psi_i^*(\vec{r}) \sum_j \frac{\psi_j^*(\vec{r}') \psi_j(\vec{r})}{(\epsilon_i + \hbar\omega + i\delta) - \epsilon_j} \\ &+ \sum_{\substack{j \\ \text{occ}}} \psi_j^*(\vec{r}') \psi_j(\vec{r}) \sum_i \frac{\psi_i(\vec{r}') \psi_i^*(\vec{r})}{(\epsilon_j - \hbar\omega - i\delta) - \epsilon_i} \end{aligned} \quad (3.3)$$

or relabeling the dummy indices in the second term:

$$\begin{aligned} \chi^0(\vec{r}, \vec{r}'; \omega) &= \sum_{\substack{i \\ \text{occ}}} \psi_i(\vec{r}') \psi_i^*(\vec{r}) \sum_j \frac{\psi_j^*(\vec{r}') \psi_j(\vec{r})}{(\epsilon_i + \hbar\omega + i\delta) - \epsilon_j} \\ &+ \sum_{\substack{i \\ \text{occ}}} \psi_i^*(\vec{r}') \psi_i(\vec{r}) \sum_j \frac{\psi_j(\vec{r}') \psi_j^*(\vec{r})}{(\epsilon_i - \hbar\omega - i\delta) - \epsilon_j} \end{aligned} \quad (3.4)$$

For cylindrically symmetric systems where $U_{KS} = U_{KS}(\rho, z)$, the azimuthal dependence of the single-electron wave functions can be separated out as shown in Eq. (2.18): $\psi_{nm}(\rho, \phi, z) = \tilde{\psi}_{nm}(\rho, z) e^{im\phi}$. Here, each single electron state $\psi_i(\vec{r})$ is described by the two quantum numbers n and m : $\psi_{nm}(\rho, \phi, z)$. A sum over all values of i then corresponds to a sum over all values of n and m . If we take $\{\tilde{\psi}_{nm}\}$ to be normalized, we must include a normalization factor of $1/\sqrt{2\pi}$ to have normalized

single electron wavefunctions:

$$\psi_{nm}(\rho, \phi, z) = \frac{1}{\sqrt{2\pi}} \tilde{\psi}_{nm}(\rho, z) e^{im\phi}. \quad (3.5)$$

The independent electron density-density correlation function can then be expressed as

$$\begin{aligned} \chi^0(\vec{r}, \vec{r}'; \omega) &= \sum_{\substack{n=1 \\ \text{occ}}}^{\infty} \sum_{\substack{m=-\infty \\ \text{occ}}}^{\infty} \frac{1}{2\pi} \tilde{\psi}_{nm}(\rho', z') \tilde{\psi}_{nm}(\rho, z) e^{im(\phi-\phi')} \\ &\times \sum_{n'=1}^{\infty} \sum_{m'=-\infty}^{\infty} \frac{\tilde{\psi}_{n'm'}(\rho', z') \tilde{\psi}_{n'm'}(\rho, z) e^{im'(\phi-\phi')}}{2\pi [(\epsilon_{nm} + \hbar\omega + i\delta) - \epsilon_{n'm'}]} \\ &+ \sum_{\substack{n=1 \\ \text{occ}}}^{\infty} \sum_{\substack{m=-\infty \\ \text{occ}}}^{\infty} \frac{1}{2\pi} \tilde{\psi}_{nm}(\rho', z') \tilde{\psi}_{nm}(\rho, z) e^{im(\phi-\phi')} \\ &\times \sum_{n'=1}^{\infty} \sum_{m'=-\infty}^{\infty} \frac{\tilde{\psi}_{n'm'}(\rho', z') \tilde{\psi}_{n'm'}(\rho, z) e^{im'(\phi-\phi')}}{2\pi [(\epsilon_{nm} - \hbar\omega - i\delta) - \epsilon_{n'm'}]}. \end{aligned} \quad (3.6)$$

The Green's function is also given in terms of the single-electron Kohn-Sham orbitals:

$$G(\vec{r}, \vec{r}'; \lambda) = \sum_i \frac{\psi_i^*(\vec{r}') \psi_i(\vec{r})}{\lambda - \epsilon_i}, \quad (3.7)$$

which due to the cylindrical symmetry can factorize as

$$G(\vec{r}, \vec{r}'; \lambda) = \sum_{m=-\infty}^{\infty} \frac{1}{2\pi} G_m(\rho, \rho'; z, z'; \lambda) e^{-im\phi'} e^{im\phi}, \quad (3.8)$$

with

$$G_m(\rho, \rho'; z, z'; \lambda) = \sum_{n=1}^{\infty} \frac{\tilde{\psi}_{nm}(\rho', z') \tilde{\psi}_{nm}(\rho, z)}{\lambda - \epsilon_{nm}}. \quad (3.9)$$

Let $\lambda^+ = (\epsilon_{nm} + \hbar\omega + i\delta)$ and $\lambda^- = (\epsilon_{nm} - \hbar\omega - i\delta)$. Using eq. (3.8) and (3.9) we

can now rewrite eq. (3.3) in terms of the Green's functions:

$$\chi^0(\vec{r}, \vec{r}'; \omega) = \sum_{\substack{n=1 \\ \text{occ}}}^{\infty} \sum_{\substack{m=-\infty \\ \text{occ}}}^{\infty} \sum_{\substack{m'=-\infty \\ \text{occ}}}^{\infty} \left[\frac{\tilde{\psi}_{nm}(\rho', z') \tilde{\psi}_{nm}(\rho, z)}{(2\pi)^2} e^{im(\phi-\phi')} e^{im'(\phi-\phi')} \right. \\ \left. \times [G_{m'}(\rho, \rho'; z, z'; \lambda^+) + G_{m'}(\rho, \rho'; z, z'; \lambda^-)] \right], \quad (3.10)$$

or letting $M = m + m'$:

$$\chi^0(\vec{r}, \vec{r}'; \omega) = \sum_{\substack{n=1 \\ \text{occ}}}^{\infty} \sum_{\substack{m=-\infty \\ \text{occ}}}^{\infty} \sum_{\substack{M=-\infty \\ \text{occ}}}^{\infty} \frac{\tilde{\psi}_{nm}(\rho', z') \tilde{\psi}_{nm}(\rho, z)}{(2\pi)^2} e^{iM(\phi-\phi')} \\ \times [G_{M-m}(\rho, \rho'; z, z'; \lambda^+) + G_{M-m}(\rho, \rho'; z, z'; \lambda^-)]. \quad (3.11)$$

In the dipole approximation and assuming polarization along the z -axis, the external driving potential is given by $V_{ext} = -zE_0$. Using this expression together with eq. (3.11) in eq. (3.1), we write the independent electron induced density as:

$$\delta n^0(\vec{r}, \omega) = \int \int \int \sum_{\substack{n \\ \text{occ}}} \sum_{\substack{m \\ \text{occ}}} \sum_M \frac{\tilde{\psi}_{nm}(\rho', z') \tilde{\psi}_{nm}(\rho, z)}{(2\pi)^2} e^{iM(\phi-\phi')} \\ \times [G_{M-m}(\rho, \rho'; z, z'; \lambda^+) + G_{M-m}(\rho, \rho'; z, z'; \lambda^-)] \\ \times (-z' E_0) \rho' d\rho' dz' d\phi'. \quad (3.12)$$

The integration over ϕ kills every term in the sum over M except the term $M = 0$ that adds a factor of 2π :

$$\delta n^0(\vec{r}, \omega) = \sum_{\substack{n=1 \\ \text{occ}}}^{\infty} \sum_{\substack{m=-\infty \\ \text{occ}}}^{\infty} \frac{-E_0 \tilde{\psi}_{nm}(\rho, z)}{2\pi} \int \int \tilde{\psi}_{nm}(\rho', z') \\ \times [G_{0-m}(\rho, \rho'; z, z'; \lambda^+) + G_{0-m}(\rho, \rho'; z, z'; \lambda^-)] \\ \times z' \rho' d\rho' dz'. \quad (3.13)$$

Now, the key observation is that, using the properties of Green's functions, integrals of the form

$$u_\lambda(\rho, z) = - \int \int F(\rho', z') G_m(\rho, \rho'; z, z'; \lambda) \rho' d\rho' dz' \quad (3.14)$$

can be expressed as solutions to the differential equation

$$\left[-\frac{1}{2} \frac{\partial^2}{\partial \rho^2} - \frac{1}{2} \frac{\partial^2}{\partial z^2} - \frac{1}{2\rho} \frac{\partial}{\partial \rho} + \frac{m^2}{2\rho^2} + U_{KS}(\rho, z) - \lambda \right] u_\lambda(\rho, z) = F(\rho, z). \quad (3.15)$$

The independent electron induced density then takes the simplified form:

$$\delta n^0(\vec{r}, \omega) = \sum_{n=1}^{\infty} \sum_{m=0}^{\infty} f_{nm} \frac{E_0 \tilde{\psi}_{nm}(\rho, z)}{2\pi} [u_{\lambda^+, nm} + u_{\lambda^-, nm}], \quad (3.16)$$

with $u_{\lambda^\pm, nm}$ satisfying:

$$\left[-\frac{1}{2} \frac{\partial^2}{\partial \rho^2} - \frac{1}{2} \frac{\partial^2}{\partial z^2} - \frac{1}{2\rho} \frac{\partial}{\partial \rho} + \frac{(0-m)^2}{2\rho^2} + U_{KS}(\rho, z) - \lambda^\pm \right] u_{\lambda^\pm, nm}(\rho, z) = z \tilde{\psi}_{nm}(\rho, z). \quad (3.17)$$

and the occupation number of the single-electron states given by the Fermi-Dirac distribution

$$f_{nm} = \frac{2}{1 + e^{\beta(\epsilon_{nm} - \mu)}}. \quad (3.18)$$

Our problem then consists of solving eq. (3.17) for all occupied states and then calculating the independent electron induced charge density through eq. (3.16).

3.2 Total induced charge density

To calculate the total induced charge density, we must use the total (self-consistent) perturbing potential in the integrand of eq. (3.1):

$$\delta n(\vec{r}, \omega) = \int d\vec{r}' \chi^0(\vec{r}, \vec{r}'; \omega) V_{tot}(\vec{r}', \omega). \quad (3.19)$$

Here, the total perturbing potential V_{tot} is the sum of the external perturbing potential V_{ext} and a term that depends on the total induced density:

$$\delta n(\vec{r}, \omega) = \int d\vec{r}' \chi^0(\vec{r}, \vec{r}'; \omega) \left[V_{ext}(\vec{r}', \omega) + \frac{\delta U_{KS}}{\delta n} \delta n(\vec{r}', \omega) \right], \quad (3.20)$$

where U_{KS} is the effective potential appearing in the electronic structure calculation. This self consistent calculation can be cast in the form of linear problem:

$$\left[1 - \int d\vec{r}' \frac{\delta U_{KS}}{\delta n} \right] \delta n(\vec{r}, \omega) = \int d\vec{r}' \chi^0(\vec{r}, \vec{r}'; \omega) V_{ext}(\vec{r}', \omega). \quad (3.21)$$

Using eq. (3.1) we may write

$$\left[1 - \int d\vec{r}' \frac{\delta U_{KS}}{\delta n} \right] \delta n(\vec{r}, \omega) = \delta n^0(\vec{r}, \omega), \quad (3.22)$$

where the right hand side has been calculated through eq. (3.16). This can be written in operator form as

$$\left[I - \hat{\chi}_0 * \frac{\delta U_{KS}}{\delta n} \right] \delta n = \hat{\chi}^0 V_{ext} = \delta n^0. \quad (3.23)$$

Calculating the total induced charge density is now cast in the form of solving the linear problem (3.23).

We use the Biconjugate Gradient Algorithm[60] to solve this linear equation. Note

that we use the Biconjugate and not the simpler Conjugate Algorithm since the operator multiplying δn is not symmetric. In this algorithm, the only thing that we need to supply is an efficient subroutine that applies $\hat{\chi}^0$ on a general function $V(\rho, z)$. The action of $\delta U_{KS}/\delta n$ is trivial to compute.

Similarly to how we computed the action of $\hat{\chi}^0$ on V_{ext} to compute δn^0 , to compute the action of $\hat{\chi}^0$ on an arbitrary function $V(\rho, z)$, we solve the linear equation:

$$\left[-\frac{1}{2} \frac{\partial^2}{\partial \rho^2} - \frac{1}{2} \frac{\partial^2}{\partial z^2} - \frac{1}{2\rho} \frac{\partial}{\partial \rho} + \frac{(0-m)^2}{2\rho^2} + U_{KS}(\rho, z) - \lambda^\pm \right] u_{\lambda^\pm, nm}(\rho, z) = V(\rho, z) \tilde{\psi}_{nm}(\rho, z). \quad (3.24)$$

for all (n, m) indices of the occupied states and use the $u_{\lambda^\pm, nm}$ to compute the desired result:

$$\hat{\chi}^0 V(\rho, z) = - \sum_{n=1}^{\infty} \sum_{m=0}^{\infty} f_{nm} \frac{\tilde{\psi}_{nm}(\rho, z)}{2\pi} [u_{\lambda^+, nm} + u_{\lambda^-, nm}]. \quad (3.25)$$

Eq. (3.24) is solved using the same Biconjugate Gradient Algorithm as before, where the action of the reduced Kohn-Sham Hamiltonian on a function $u(\rho, z)$ is implemented on a grid, using a finite difference expression for the kinetic part.

The convergence of the Biconjugate Gradient Algorithm depends crucially on the initial guess. One important aspect of the present calculations is that we compute the optical spectrum for a sequence of frequencies and the computed δn for one frequency can be used as the starting point in the Biconjugate Gradient Algorithm for the next frequency. Thus, excepting the first frequency, the iteration in the Biconjugate Gradient Algorithm converges extremely fast, typically in less than 4 steps.

From the perturbed density we compute the induced dipole moment $\vec{P}(\omega) = \int \vec{r} \delta n(\vec{r}, \omega) d^3 \vec{r}$. In the linear response regime, $\vec{P}(\omega)$ is proportional to the driving field \vec{E}_0 : $\vec{P}(\omega) = \hat{\alpha}(\omega) \vec{E}_0$, where $\hat{\alpha}(\omega)$ is the frequency dependent polarizability tensor of the system. The total optical absorption cross section $\sigma(\omega)$ is directly related to the

imaginary part of the polarizability. For a driving field oriented along the z direction, $\sigma(\omega) = \frac{\omega}{c} \text{Im}[\alpha_{zz}(\omega)]$.

In the following chapters we will apply the formalism described above to investigate the optical properties of a variety of metallic nanostructure geometries of interest.

Single Particle Systems: Nanorods

One of the most pivotal discoveries in the field of plasmonics has been the realization that the plasmon resonances of a metallic nanoparticle can be tuned to occur at specific frequencies by modifying the particle geometry. This has been demonstrated experimentally for a variety of nanostructures whose plasmonic properties were nanoengineered using reproducible, controlled processes specific to each structure. Two of the most highly tunable plasmonic particles available are nanoshells and nanorods. For nanoshells, [22, 61, 62, 63, 64] the plasmon frequencies can be tuned by simply varying the ratio between the thickness of the shell and the overall diameter, which can be accomplished by controlled chemical synthesis. Nanorods, in contrast, are characterized by their aspect ratio ζ , defined as the ratio between its length and its width. The energies of their plasmon resonances depend quite sensitively on ζ , [65, 41, 39, 66, 67] so varying this ratio provides the tuning mechanism for nanorods. Nanorods can be fabricated by either template-based or seeded growth methods.[41] In contrast to the nanoshell, the nanorod is anisotropic and exhibits different resonances when illuminated with light of different polarizations. The ease with which these two types of nanoparticles can be synthesized with controlled geometry has made both nanoshells and nanorods highly popular substrates for applications in

sensing, medicine, and spectroscopy.[68, 69, 70]

The electromagnetic properties of both nanoshells and nanorods have been investigated quite extensively using classical electromagnetic theory.[71, 72] There have only few *ab initio* studies on this subject. The spherical symmetry of nanoshells simplifies their theoretical investigation by allowing the computational problem to be reduced to one dimension. [73, 74, 33] Nanorods, on the other hand, exhibit cylindrical symmetry, and their theoretical investigation from first principles requires solving a two dimensional problem. [11] This chapter is devoted to exploiting our generalized TDDFT formalism for cylindrically symmetric systems to study nanorods. We will see how quantum effects play a significant role in accurately describing the plasmonic properties of nanorods and are of crucial importance to establish the limits of validity of classical descriptions.

In classical electromagnetic modeling, the nanoparticles are defined by their dielectric permittivity, which changes abruptly at the nanoparticle-air interface. Such classical approximations neglect the spill-out of electrons outside a realistic nanoparticle surface, and also do not take into account the associated gradual change of the dielectric properties at the surfaces. Electron spill-out at the particle surfaces introduces a source of screening that is absent in a classical description.

In this chapter we will focus on the optical properties of silver nanorods. We will see how the calculations reveal distinct longitudinal and transverse plasmon resonances with frequencies that can be tuned by varying the aspect ratio ζ of the nanorod. The ζ dependence of the energies of both the longitudinal and transverse plasmon modes has been found to be in excellent agreement with the predictions of classical electromagnetic modeling, where the surfaces of the nanoparticles are assumed to be infinitely sharp. However, the plasmon-induced electric field enhancements obtained from the quantum mechanical approach are found to be much smaller than those

obtained using classical theory. The major differences occur within 0.5 nm of the surface of the nanoparticle, and are due to nonlocal screening introduced by the finite electron spill-out.

4.1 Optical Absorption

For the size regime that is the focus of this chapter, particles are in the quasistatic limit and the optical response is dominated by the dipolar plasmon mode [58]. The optical spectra of small nanorods are characterized by a longitudinal and two degenerate transverse dipolar plasmon resonances. From experiment as well as classical simulations,[65] the longitudinal mode is known to strongly redshift as the aspect ratio ζ of the rod increases, while the transverse mode has the opposite behavior, i.e. it blueshifts with increasing ζ . The longitudinal mode is also known to be more sensitive to changes in the aspect ratio than the transverse mode.

For our simulations, we model the nanorods as prolate spheroids. In this case, their geometry is uniquely defined by their aspect ratio ζ and length b of their major axis. To do the quantum calculations, the strength of the pseudopotential $V_0(\vec{r})$ (see Eq. (2.8)) has been adjusted such that the computed work function matches the value of 4.5 eV appropriate for Ag. This assures that our simulations give the correct electron spill-out profile. In addition, our simulation includes a background dielectric that takes into account the polarizability of the ion cores.

As described in chapter 2, our simulations are based on a jellium description appropriate for Ag, which assumes a uniformly distributed positive ionic charge of appropriate density throughout the volume of the nanorod. In each direction, the size of the jellium model is half a lattice plane spacing larger than the physical size of the particle. For Ag, the separation between close-packed lattice planes is approximately 4 Bohr, which places the jellium surfaces approximately 2 Bohr outside what would

be the real surface of the silver nanoparticles. For the frequency range considered in this paper, such jellium models are known to provide good quantitative descriptions of the optical properties of small metallic nanoparticles.[32] As discussed in chapter 2, this approximation will enable us to simulate sufficiently large structures (up to more than 2×10^3 conduction electrons), a necessary condition in order to obtain a well-developed plasmonic response.

We employ the linear response version of TDDFT discussed in chapter 3. The equilibrium self-consistent Kohn-Sham equations are solved for the conduction electrons of the nanorods. The equilibrium Kohn-Sham orbitals are then used to compute the independent electron response function and the induced screening charge is obtained from a Random Phase Approximation-type integral equation, as discussed previously.

We start by investigating nanorod spectra. In Fig. 4.1 we plot the normalized TDDFT optical absorption cross sections as a function of photon energy for nanorods of different aspect ratios ζ , ranging from $\zeta = 1$ (spherical) to $\zeta = 3$ (highly elongated). We have adjusted the overall lengths b of the nanorods so that each nanorod contains exactly 510 conduction electrons. Fig. 4.1 shows results for longitudinal (upper panel) and transverse (lower panel) polarization of the incident light. As one can see, all absorption curves display a prominent peak which is identified as a dipolar plasmon resonance. For longitudinal polarization, we observe a strong redshift of the plasmon resonance with increasing ζ . In contrast, for transverse polarization, the plasmon modes blueshift with increasing ζ , and the shifts are relatively small. The redshift of the longitudinal mode and the blueshift of the transverse mode with increasing aspect ratio is in agreement with previous classical electromagnetic calculations and experimental data.[65]

The calculated spectra are all consistent with the f-sum rule, which states that the

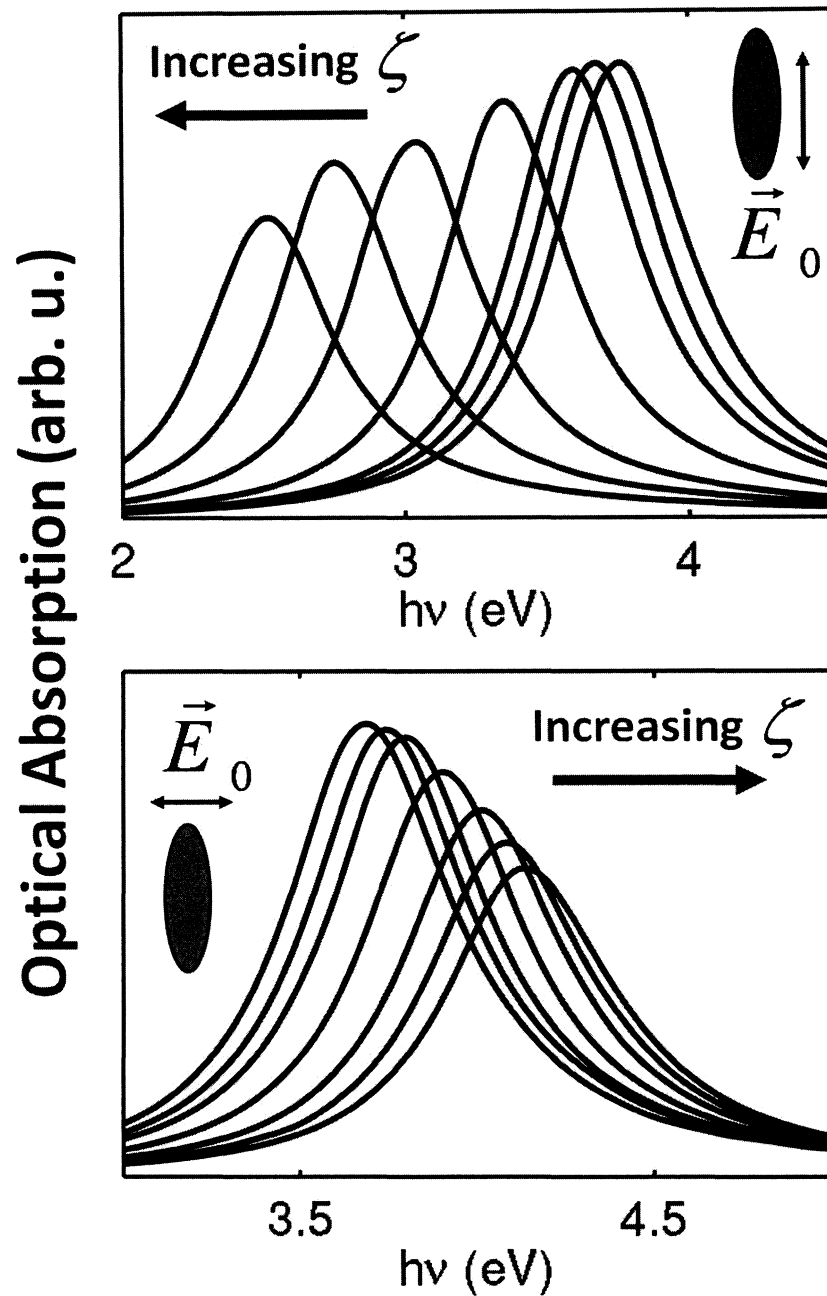


Figure 4.1: Optical absorption spectra calculated using TDDFT for nanorods of different aspect ratios ζ . The top panel shows the longitudinal mode for nanorods with $\zeta = 3, 2.5, 2, 1.5, 1.2, 1.1$, and 1 with the labeling going from left to right. The bottom panel shows the transverse mode for the same ζ , but with a labeling from right to left. The length b of the nanorod is scaled so that each nanorod contains the same number of electrons (510). The spectra have been normalized to the cross sectional area of the nanorod.

total area under the curves remains constant. The intensity changes of the plasmon peak with aspect ratio are caused by our present normalization of the spectra in the figure. The spectra have been normalized to the cross sectional area of the nanorod.

In Fig. 4.2 we plot the plasmon resonant frequencies as functions of ζ as extracted from Fig. 4.1. The two branches correspond to the longitudinal and transverse plasmon modes. For comparison, we include the results of classical electromagnetic calculations using the appropriate dielectric function for Ag. As can be seen, there is good quantitative agreement between classical and quantum descriptions for both the longitudinal and transverse modes. The TDDFT results slightly overestimate the energies for the transverse modes. This is a quantum size effect, which is expected to be stronger for the transverse polarization due to a more pronounced electron confinement in the transverse direction. It is clear that good quantitative agreement is obtained between the quantum and classical results when comparing the plasmon peak positions of nanorods. A similar quantitative agreement was seen between these two approaches for the calculated plasmon peak positions of nanoshells. [33, 32]

4.2 Field Enhancements

We will now investigate the electromagnetic field enhancements in nanorods using the same approach. Our focus will center mainly around the longitudinal dipolar plasmon mode, which is of primary interest in applications due to its facile tunability. In Fig. 4.3 we plot the field enhancements for rods of different aspect ratios. The bottom panels of the figure show the intensity maps of E/E_0 , where E is the electric field in the presence of the nanorod and E_0 is the applied electric field. The electric field intensities are plotted for rods of four different aspect ratios at the corresponding resonant frequencies for each case. The bottom row of the figure displays the quantum mechanically calculated field enhancements, and the classically calculated

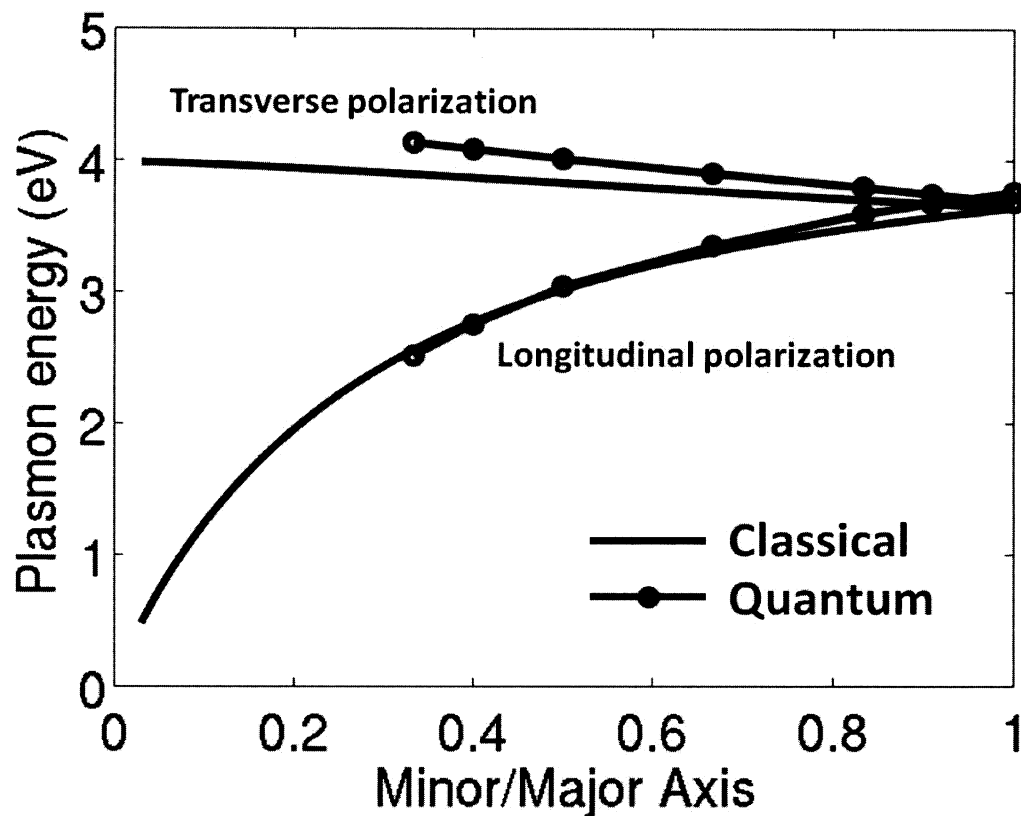


Figure 4.2: Longitudinal and transverse dipolar plasmon energies of a silver nanorod as a function of inverse aspect ratio $1/\zeta$ for the nanorods discussed in Fig. 4.1. The TDDFT results are shown in blue and the classical electromagnetic results obtained using an equivalent dielectric permittivity for Ag are shown in black.

enhancements are plotted in the middle row. The rods are kept at a constant volume (containing 510 electrons) as we change the aspect ratio. The electric field intensity panels in the figure reveal that the spatial distribution of the field enhancements are similar for both the TDDFT and classical calculations. There are clear differences, however, if we look at the maximum value of the field enhancements.

In the top panel of Fig. 4.3 we show the maximum value of the field enhancements extracted from the intensity maps as a function of ζ . For both methods of calculation, the maximum enhancements grow monotonically with ζ , but it is clear that the classical calculations overestimate the growth rate. For the case of perfect spheres ($\zeta = 1$) we have the lowest discrepancy between the maximum field enhancements calculated from both methods: the classical enhancements yield a value of 6 while the TDDFT result gives a value of 4. The difference between the two approaches becomes more pronounced with increases in the particle aspect ratio. For the most elongated particles ($\zeta = 3$), the maximum classical field enhancement is 24, almost twice as large as the TDDFT value of 13.

To look more closely at the differences between the field enhancements calculated with the classical and quantum mechanical approaches, we now plot the enhancements as a function of distance from the particle surface. Fig. 4.4 is a plot of the local field enhancements calculated at the peak resonant frequency using TDDFT (black curves) and classical electrodynamics (red curves). The top panel shows the enhancements for a sphere ($\zeta = 1$) and the bottom panel shows the enhancements for a rod ($\zeta = 3$) as a function of separation d from the particle surface. For both particles, the classical and TDDFT field enhancements are very similar for d larger than 10 Bohr, but start to deviate in value when d becomes smaller than 5 Bohr, with the difference reaching its largest value at the particle surface ($d = 0$ Bohr). The figure reveals that the TDDFT field enhancements peak at approximately $d = 3$ Bohr from the surface,

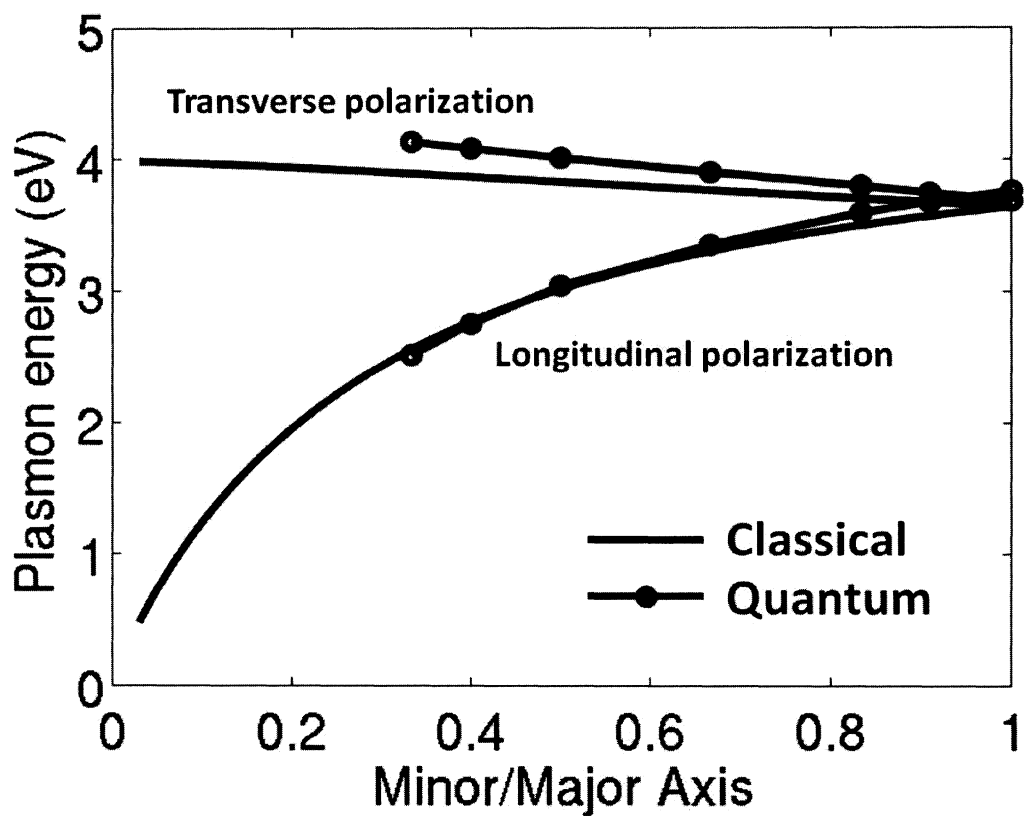


Figure 4.2: Longitudinal and transverse dipolar plasmon energies of a silver nanorod as a function of inverse aspect ratio $1/\zeta$ for the nanorods discussed in Fig. 4.1. The TDDFT results are shown in blue and the classical electromagnetic results obtained using an equivalent dielectric permittivity for Ag are shown in black.

enhancements are plotted in the middle row. The rods are kept at a constant volume (containing 510 electrons) as we change the aspect ratio. The electric field intensity panels in the figure reveal that the spatial distribution of the field enhancements are similar for both the TDDFT and classical calculations. There are clear differences, however, if we look at the maximum value of the field enhancements.

In the top panel of Fig. 4.3 we show the maximum value of the field enhancements extracted from the intensity maps as a function of ζ . For both methods of calculation, the maximum enhancements grow monotonically with ζ , but it is clear that the classical calculations overestimate the growth rate. For the case of perfect spheres ($\zeta = 1$) we have the lowest discrepancy between the maximum field enhancements calculated from both methods: the classical enhancements yield a value of 6 while the TDDFT result gives a value of 4. The difference between the two approaches becomes more pronounced with increases in the particle aspect ratio. For the most elongated particles ($\zeta = 3$), the maximum classical field enhancement is 24, almost twice as large as the TDDFT value of 13.

To look more closely at the differences between the field enhancements calculated with the classical and quantum mechanical approaches, we now plot the enhancements as a function of distance from the particle surface. Fig. 4.4 is a plot of the local field enhancements calculated at the peak resonant frequency using TDDFT (black curves) and classical electrodynamics (red curves). The top panel shows the enhancements for a sphere ($\zeta = 1$) and the bottom panel shows the enhancements for a rod ($\zeta = 3$) as a function of separation d from the particle surface. For both particles, the classical and TDDFT field enhancements are very similar for d larger than 10 Bohr, but start to deviate in value when d becomes smaller than 5 Bohr, with the difference reaching its largest value at the particle surface ($d = 0$ Bohr). The figure reveals that the TDDFT field enhancements peak at approximately $d = 3$ Bohr from the surface,

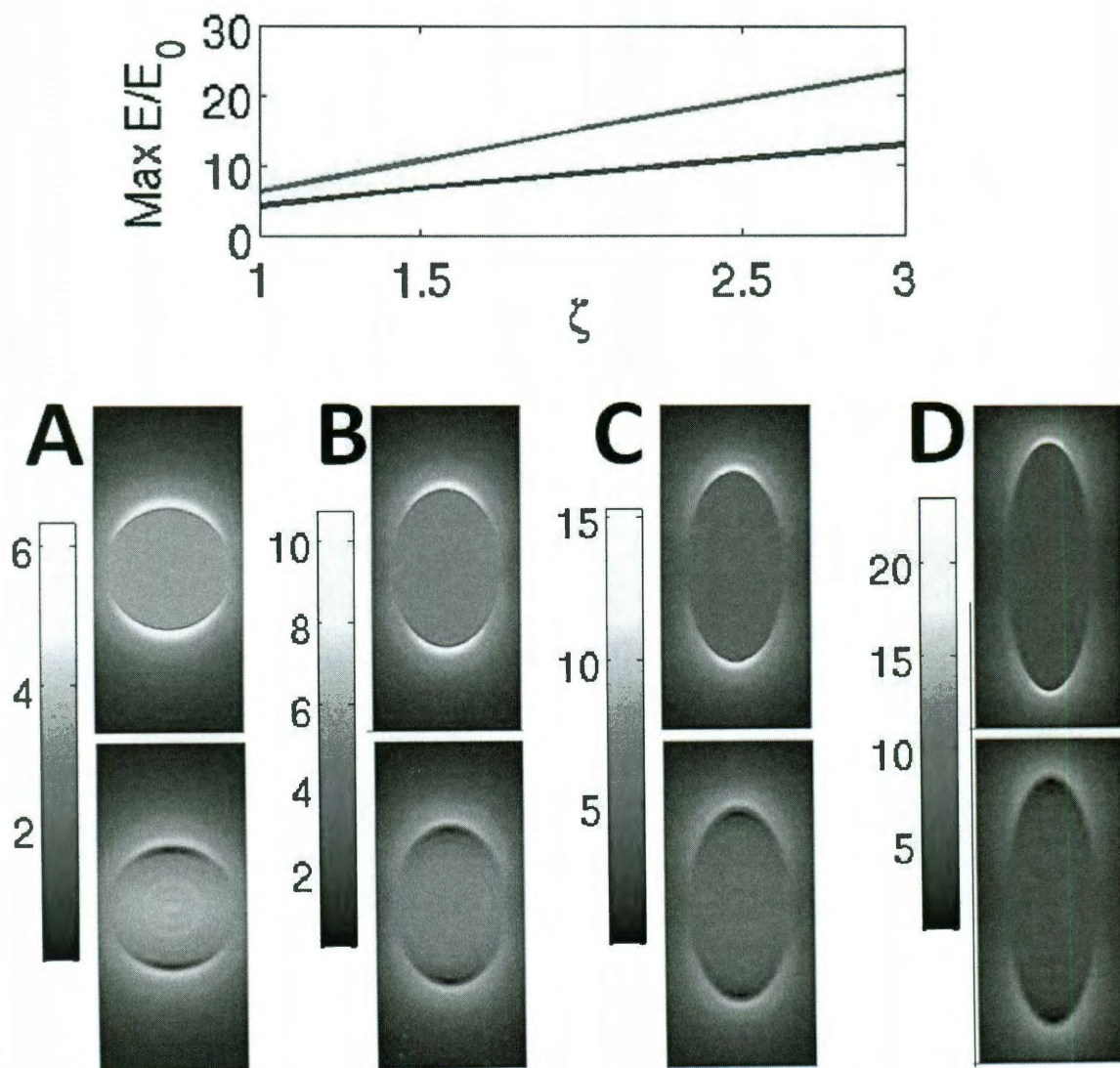


Figure 4.3: The upper graph shows a comparison of the maximum electromagnetic field enhancements calculated using classical electromagnetic theory (red) and TDDFT (blue) for a nanorod as a function of ζ . The lower panels compare the field distributions calculated using classical electromagnetic theory (top panels) and TDDFT (bottom panels) for $\zeta = 1$ (A), $\zeta = 1.5$ (B), $\zeta = 2$ (C), and $\zeta = 3$ (D). The field enhancements were calculated for the resonant frequency of the longitudinal dipolar plasmon using a broadening of $\delta = 0.27$ eV. The overall size b of each nanorod has been adjusted so it contains 510 electrons.

while the classical enhancements peak at the surface ($d = 0$ Bohr). This is true for rods of all aspect ratios. We will see shortly that the reason for the large discrepancy between the TDDFT and classical field enhancements in the near surface region ($d < 5$ Bohr) is that the plasmon induced electron density calculated with the quantum mechanical approach is smeared over a significant region of space, while the induced density in the classical picture is an infinitely thin two-dimensional surface charge. Since the classical framework yields an induced surface charge that is a delta function in d , the maximal field enhancements occur at $d = 0$.

In order to understand why the classical approach overestimates the field enhancements at short separations from the particle surface, it is helpful to analyze the electronic structure of the nanorods. In Fig. 4.5A we plot the equilibrium electron density as a function of distance d from the surface of the nanorod. The electron density is shown along the long (red) and short (black) axis for a nanorod with $\zeta = 3$. For comparison, we also show the density profile for a spherical particle of $\zeta = 1$ (blue). The oscillatory behavior of the electron density inside the nanoparticles is due to Friedel oscillations. [32] We can see from the figure that the spill-out density is the same for all three cases, as we would expect, since the asymptotic electron density profile is determined by the Fermi level ϵ_F of the particle and vanishes as

$$n(d) = n_0 e^{-\sqrt{-2\epsilon_F}d}, \quad (4.1)$$

where ϵ_F is measured from the vacuum level. The electron spill-out extends to approximately 3 Bohr beyond the particle surface. An important feature to notice in Fig. 4.5 is the pronounced anisotropy of the electron density for the elongated $\zeta = 3$ nanorod, which can be easily seen by comparing the red and black curves. This is a purely geometrical effect due to the enhancement of Friedel oscillations by the increased electron confinement in the transverse direction.

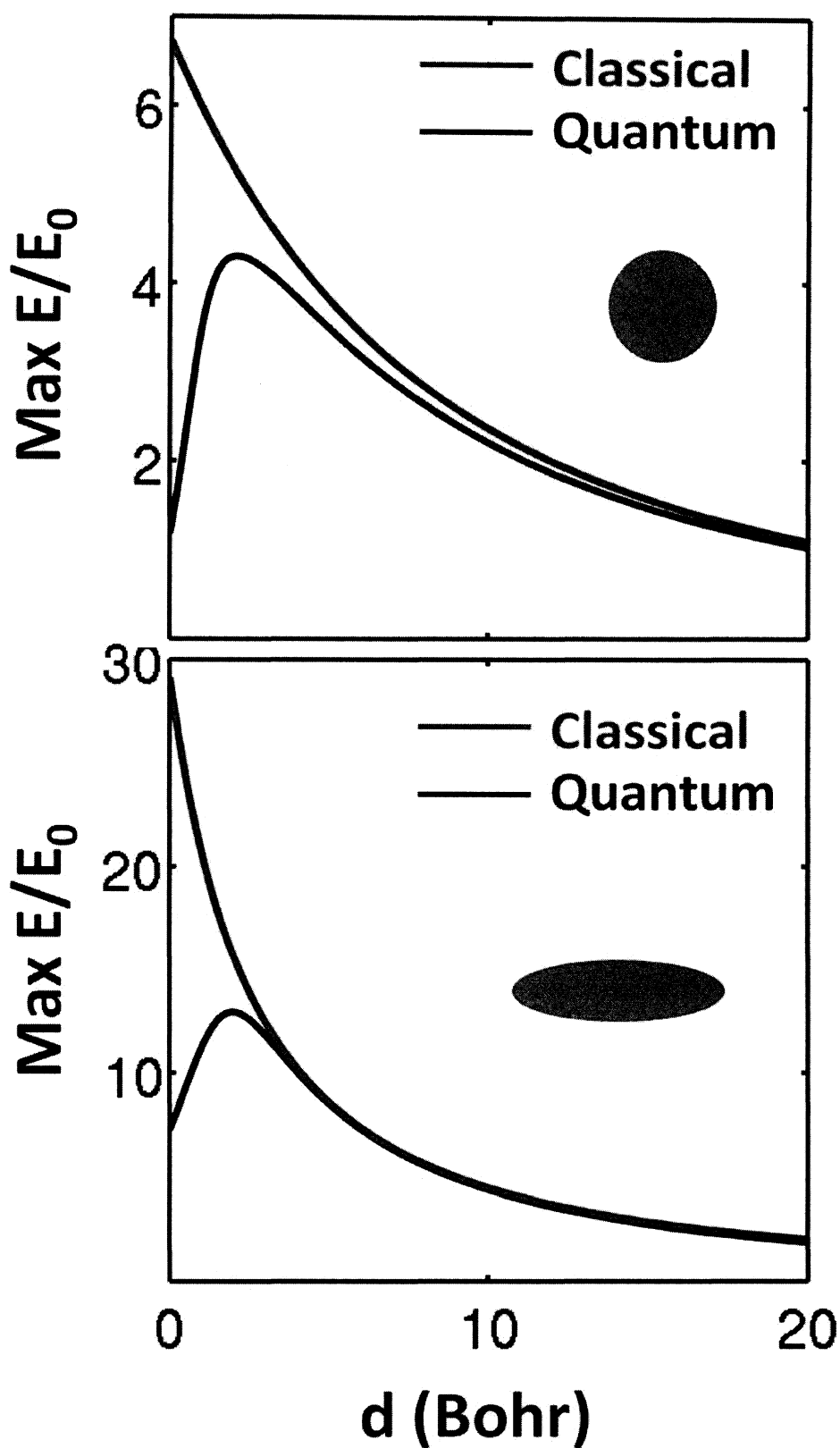


Figure 4.4: Electric field enhancements as a function of distance d from the particle tip for an aspect ratio of $\zeta=1$ (top) and $\zeta=3$ (bottom). The classical calculations are shown with red lines and the TDDFT results are shown with black lines.

For the same nanorods as in Fig. 4.5A, we also calculate the induced screening charge density δn using the TDDFT approach. Fig. 4.5B shows the induced charge density δn at the longitudinal plasmon frequency, as a function of distance d from the nanorod surface. The more elongated rods ($\zeta = 3$) show a pronounced increase in the screening charge near the tip area, as compared with the spheres ($\zeta = 1$). This larger accumulation of charge near the tip is responsible for the increase in field enhancements for more elongated particles. In a classical picture, the same phenomenon appears, and more elongated particles have a larger accumulation of charge in the tip vicinity, leading to larger field enhancements. The crucial difference is that, in the classical picture, the induced screening charge is an infinitely thin surface charge, while the quantum calculations reveal a charge density that is distributed over a thick region (~ 10 Bohr) around the nanoparticle surface and extends out as far as the spill-out in the ground state electron density shown in Fig. 4.5A. For d well outside this smeared density, the Coulomb potential of the 3-dimensional volume charge density is not much different from that of the 2-dimensional surface charge, since the magnitude of the total induced charge is the same in both cases. This results in good agreement between the classical and TDDFT field enhancements at separations larger than about 10 Bohr, as we saw in Fig. 4.4. For $d < 10$ Bohr, the three dimensional induced charge distribution giving rise to the quantum mechanically calculated field enhancements reduces their value in comparison to the classically calculated enhancements. For d inside the smeared density region, the quantum mechanical field enhancements are generated by only a fraction of the total induced charge density, resulting in the decrease of the TDDFT enhancements for $d < 3$, as we saw in Fig. 4.4.

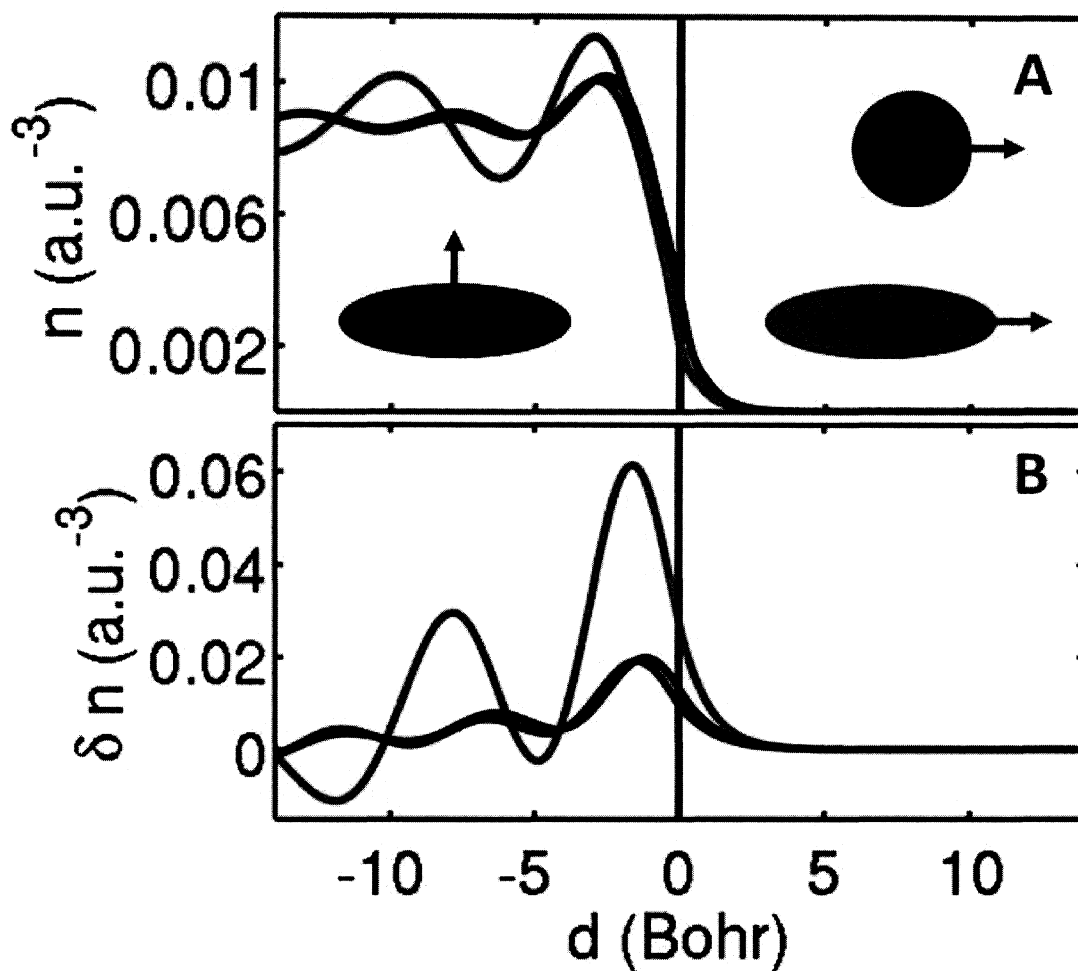


Figure 4.5: (A) Equilibrium electron density calculated using TDDFT as a function of distance from the particle surface along the long axis for nanorods of aspect ratios $\zeta = 1$ (blue curve) and $\zeta = 3$ (red curve), and perpendicular to the long axis for nanorods of $\zeta = 3$ (black curve). (B) Induced screening charge calculated using TDDFT as a function of distance from the particle surface along the long axis for nanorods of aspect ratios $\zeta = 1$ (blue curve) and $\zeta = 3$ (red curve), and perpendicular to the long axis for nanorods of $\zeta = 3$ (black curve). The insets show the definitions of the coordinate d .

4.3 Quantum Size Effects

As the size of nanorods becomes smaller, the onset of quantum size effects might affect plasmonic properties. Our goal here is to investigate at what scales such effects start to take place. An important size-dependent factor that may influence the plasmon energies and induced electric field distributions is the electronic density of states. In momentum space, a plasmon oscillation may be envisioned as a harmonic variation of the momentum of each conduction electron. If the energy spacings between the electronic states in the particle are too large, a plasmon oscillation is not possible. This is the reason why neither a small nanoparticle nor an individual atom exhibits a plasmonic response. We now look at how the absorption spectra of nanoparticles is modified as the size gets small enough for quantum size effects to play a significant role.

In Fig. 4.6, we compare the absorption spectra for longitudinal polarization of five nanorods with the same aspect ratio ($\zeta = 3$) but a wide array of values for the major axes b . In a classical description, their absorption spectra would be identical, except for a trivial scaling by a factor proportional to the number of electrons in the nanoparticle. Fig. 4.6 clearly shows blueshifted plasmon resonances for the two smallest nanorods. For particles containing less than 100 electrons, the plasmon resonance is not fully developed and quantum size effects influence the spectra, i.e., the plasmon peak positions shifts with particle size. The figure shows that the plasmon resonances tend to redshift with increasing particle size. Such a redshift is similar to that observed in TDDFT calculations for nanoshells of the same aspect ratios but varying overall size and is caused by slight changes in the surface electron density distribution.[33] The spectra for the largest two particles are very similar, showing size convergence for particles containing more than 500 electrons.

The sizes of the nanorods we investigate are small ($b < 162$ Bohr), so an interesting

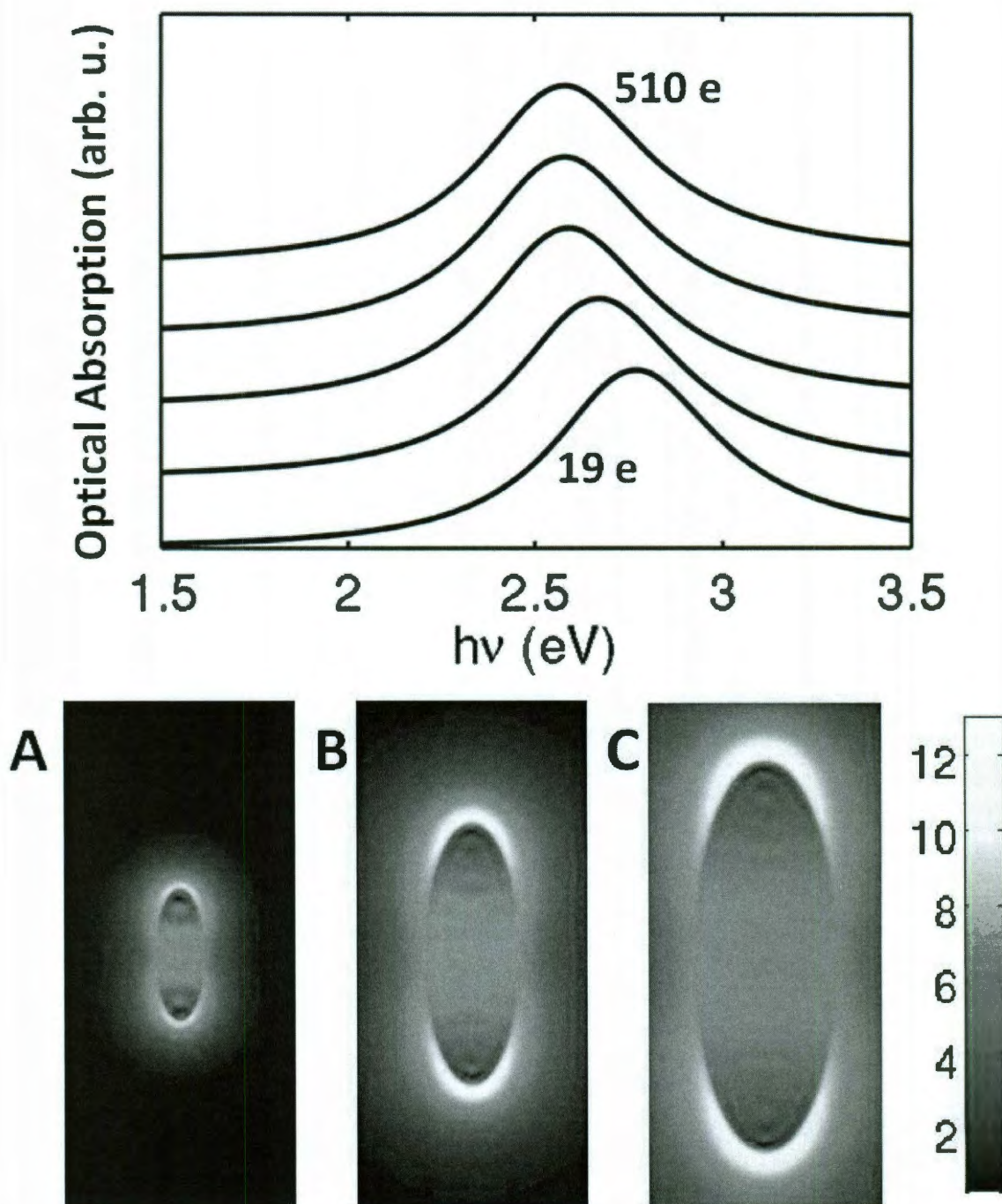


Figure 4.6: Top panel: Absorption spectra calculated using TDDFT for five nanorods of the same aspect ratio ($\zeta = 3$) but different major axis b : 17 Bohr (19 electrons), 20 Bohr (63 electrons), 33 Bohr (151 electrons), 42 Bohr (294 electrons), and 50 Bohr (510 electrons) from bottom to top. The absorption spectra have been scaled so the absorption maxima are the same for each nanorod. Bottom panel: Plasmon-induced electric field enhancements for the $b=17$ Bohr (A), 33 Bohr (B), and 50 Bohr (C) nanorods.

question is whether our present findings apply to larger nanorods. The asymptotic form of the electron spill out (Eq. 4.1) holds for particles of all sizes, but for larger nanorods, the electronic state distribution becomes more dense and more electrons are available at the Fermi energy. This naturally leads to an increase in the electron spill-out density near the surface. An increased spill-out density will make the nanorod appear larger and thus may change its effective aspect ratio and therefore its plasmon energies. Also, as discussed in Fig. 4.5, the spill-out determines the width of the smeared plasmon-induced electron density. An increased spill-out density will introduce a further smearing of the induced electron density and may thus reduce the field enhancements even further, relative to classical results.

4.4 Extrapolation to larger particles

Classical electromagnetic calculations in the quasistatic regime, where retardation effects can be ignored, are scale invariant. For nanorods in this regime, the magnitudes of the electromagnetic field enhancements are determined solely by the aspect ratio ζ , and not by the particle size. The behavior seen in the quantum calculations is slightly different. In Fig. 4.7 we show the field enhancements as a function of the scaled distance from the surface of the tip, $\hat{d} = d/b$, where d is the distance from the rod surface (as defined in the red inset of Fig. 4.5), for different size nanorods with the same $\zeta = 3$. The dashed line shows the scale-invariant classical enhancements, which increase monotonically with decreasing \hat{d} . The solid lines are the field enhancements calculated using TDDFT. The quantum mechanical effects are not scale invariant, since they are determined by the electronic structure and the electron spill-out (Eq. (4.1)). The quantum calculations differ from the classical results only at physical distances smaller than $d = d_{QM} = 0.5$ nm from the particle surface. As the particles get larger, then, the quantum calculations differ from the classical results

at smaller values of \hat{d} . When the particle size is increased, the maximum quantum field enhancement near the surface increases monotonically, asymptotically approaching the scale-invariant electrostatic result. In real systems this limit would never be reached since retardation effects, which reduce the field enhancements, begin to play an important role when the physical dimensions of the nanorod becomes larger than a quarter of the plasmon wavelength.

Although the present calculations are performed for small model systems, the results are robust and show only small changes as the overall sizes of the structures are increased. It is clear that our prediction that the classical electromagnetic field enhancements break down near the nanoparticle surface is a real effect. The predicted distances where this breakdown happens (around 0.5 nm) are most likely underestimated. For more realistic size particles, the electron spill-out is likely to extend to larger distances, due to the closer spacings of the electronic states of the nanoparticle. In addition, our quantum approach is based on the local density approximation, which neglects the electron image potential. The image potential will lower the potential barrier in the vacuum direction and will therefore increase the equilibrium electron spill-out n near the surface. Since the induced charge density δn involves excitations of electrons out of their ground state, it is likely that the image potential will have an even more significant effect on the profile of the induced charge δn and thus on the induced electric field enhancements.

Another important point is that our study focuses on rods with smooth edges. Even the most elongated rods considered do not have sharp tips. We expect particles with sharp edges to have more pronounced quantum size effects due to the increased electron density near the sharp tips.

Our TDDFT calculations confirm the tunability of the longitudinal and transverse dipolar plasmon modes predicted using classical electromagnetic modeling. The most

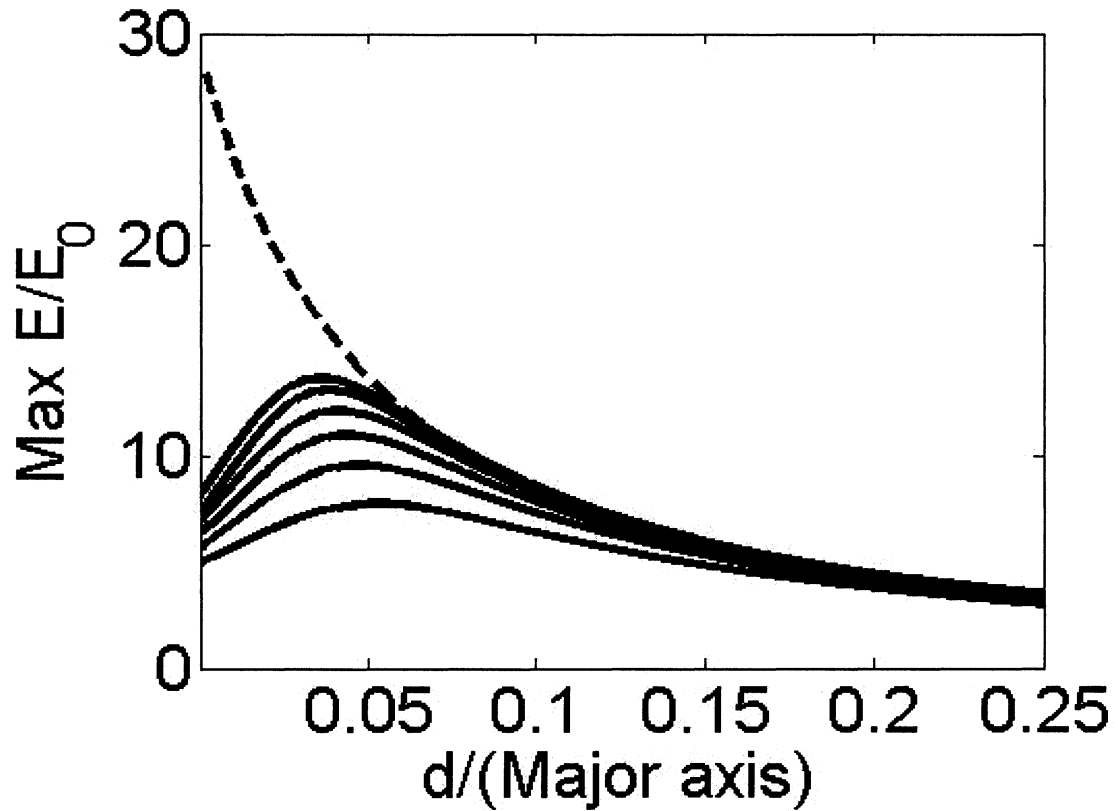


Figure 4.7: Electromagnetic field enhancements as a function of $\hat{d} = d/b$ along the rod axis for rods of $\zeta = 3$. The dashed line represents the scale-invariant classical result. The solid lines show the quantum mechanical results for rods of different sizes: 19, 63, 151, 294, 882, and 2171 electrons (from bottom curve and up).

important insight we have gained from the first-principles calculations is that the field enhancements show significant differences from classical predictions at positions closer than 0.5 nm from the nanoparticle surface. These differences arise from the electronic structure of the particles and from the spatial distribution of the plasmon-induced electron surface charges.

Recently, there has been an increasing interest in understanding the plasmonic behavior of two nanoparticles in close proximity to each other.[75, 76, 47, 77, 78, 79, 80, 81, 82] Such nanoparticle pairs, known as “dimers” are important for understanding the dynamics of hybridized plasmons in complex nanostructures. The intense current interest surrounding this geometry is due, in part, to the extremely large field enhancements predicted to appear in narrow dimer junctions, which have direct applications in single molecule surface enhanced spectroscopies.[83, 84, 85, 86, 87, 88]

Although nanoparticle dimers have been extensively studied both experimentally and theoretically,[89, 90] so far, theoretical investigations have mostly employed classical approaches. In such classical descriptions, the nanoparticle surfaces are modeled as abrupt and sharp terminations of the particles. These approaches reveal distinct behaviors in two different regimes: when the particles are close to each other but not touching, and when the particles are touching with conductive overlap. In the non-touching regime, the dipolar dimer plasmon redshifts monotonically with decreasing interparticle separation. When conductive overlap is established between the nanoparticles, a new plasmon mode is enabled. This is the Charge Transfer Plasmon (CTP)[47] and involves conduction electrons flowing back and forth between the

two nanoparticles. The resonant frequency of the CTP blueshifts when the overlap between the two nanoparticles is increased. Classical descriptions predict an abrupt, discontinuous transition from non-touching to touching particles as the distance between nanoparticles is continuously reduced.[77, 47]

In the investigation of dimers, a purely classical description breaks down in the limit of nearly touching nanoparticles. In this regime, electrons can tunnel between the nanoparticles and thus, in principle, enable a CTP. Moreover, the finite electron density distribution in the junction between the particles can screen the plasmonic interactions responsible for the strong redshift of dimer plasmons observed in the classical regime. It is evident that a quantum mechanical approach involving realistic electron density profiles and including effects such as tunneling and screening is essential to accurately describe the optical properties of closely spaced nanoparticles.[91, 92, 93]

In this chapter we present fully quantum mechanical calculations of the plasmonic properties of metallic nanosphere dimers. We present calculations for different nanosphere sizes and various nanosphere separations. We identify three distinct regimes of interactions between the two nanoparticles. In the classical regime, where the nanosphere separation is larger than 1 nm, the electron potential between the two particles is characterized by a large potential barrier that prevents electrons from transferring between the nanoparticles. In this regime, each nanosphere remains neutral during a plasmon excitation. The plasmonic coupling between the nanospheres can be well described using classical approaches such as Plasmon Hybridization (PH)[94] and results in optically active, “bonding” hybridized plasmons that redshift strongly with decreasing interparticle separation.[47, 90] As the interparticle distance is reduced, one approaches the crossover regime, which occurs for interparticle separations smaller than 1 nm but larger than 0.5 nm. Here the classical description breaks down and quantum mechanical effects begin to play an important

role in the optical response of the system. In the crossover regime the electron potential between the two nanoparticles is characterized by a narrow barrier through which electrons may tunnel. The charge transfer across the junction reduces the electromagnetic interactions between the two particles, resulting in a much smaller hybridization and a less pronounced redshift of the bonding dipolar dimer plasmons. Interparticle separations smaller than 0.5 nm define the conductive regime. Here, the Fermi level of the system lies above the electron potential barrier separating the two particles, and the conductance of the junction is large. A CTP appears with an intensity that increases and an energy that blueshifts as the interparticle separation is further decreased. The energy and width of the CTP resonance depend sensitively on the touching profile and on the electronic structure of the individual nanoparticles.

As before, we do our calculations using the jellium model, where the ionic background charge of the particles is replaced by a uniform charge density n_0 that terminates at the nanoparticle surfaces. The value of n_0 was fixed to a Wigner-Seitz radius of $r_s=3$ Bohr, which is a typical value for many noble and simple metals. We have used a pseudopotential (see eq. 2.8) $V_0 = -2.72$ eV to set the Fermi energy of the dimers at 4.0 eV below the vacuum level. Fig. 5.1 shows the equilibrium electron density and self-consistent effective Kohn-Sham potential for a nanosphere dimer of sphere radii $R = 12$ Bohr and interparticle separation $d = 1$ Bohr. The figure reveals a finite electron density and low potential barrier in the narrow junction, as is expected for short interparticle separations.

A polarizable background may be included in our TDDFT calculations, as we have done for the nanorods in chapter 4. In the investigation of dimers, however, we neglect the background polarizability of the metal and focus on the effects mediated by the coupling of electrons to emphasize the plasmon energy shifts caused by changing interparticle separations.

The radii R of the nanoparticles refer to the radii of the jellium spheres which are half a lattice plane spacing larger than the physical sizes of the nanoparticles. For noble and simple metal crystals, the spacing between close-packed planes is typically around 5 Bohr. The dimer separation distances d refer to the separation of the jellium edges of the respective nanoparticles. Thus the physical separation D of the nanoparticles is related to d as $D=d+5$ Bohr. The polarization of the incident light is assumed to be oriented along the dimer axis and only the longitudinal dimer plasmons will be discussed.

5.1 Optical Absorption

We first focus on the absorption spectra of nanoparticle dimers. In Fig. 5.2 we show the dipolar optical absorption $\sigma(\omega)$ as a function of photon energy $\hbar\omega$ for dimers consisting of nanospheres of radius $R=16$ and 24 Bohr, placed at various separations d from each other. The nanosystems contain 302 and 1018 conduction electrons, respectively. For large separations (of the order of the individual sphere radii) the dimers behave as two individual nanospheres with dipolar sphere plasmon resonances at nominally 5 eV. As the separation distance becomes smaller, the dipolar ($l=1$) dimer plasmon resonance redshifts monotonically until a separation distance of about $d=10$ Bohr. For this separation, the $R=16$ dimer resonance occurs at 4.8 eV and the $R=24$ dimer resonance at 4.2 eV. This redshift is a classical effect caused by the electromagnetic interactions of the plasmons of the individual nanospheres leading to the formation of hybridized dimer modes.[94] The reason the $R=24$ resonance is more strongly redshifted is that, for small systems, the electromagnetic interactions are scale invariant, i.e. in the classical regime the dimer plasmon resonances depend on the dimer geometry as the ratio d/R . Thus, the sphere plasmon modes in the larger dimer are more strongly coupled and redshifted for the same fixed separation.

For the $R=24$ dimer, a second dimer resonance appears at approximately 5.5 eV for $d=10$ Bohr. This is the predicted[94] bonding hybridized quadrupolar ($l=2$) dimer resonance, which appears in the dipolar optical spectra because of the hybridization with dipolar individual nanosphere plasmons.[94, 47] The quadrupolar dimer resonance only appears for small nanosphere separations and redshifts only weakly with separation because of the lower magnitude of quadrupolar interactions.[94]

For separations in the interval $10 > d > 3$ Bohr, the dimer plasmon resonances do not shift significantly in energy. This is the crossover regime where electrons begin to tunnel between the two nanoparticles. The conductance of the junction between the nanospheres is too small for a CTP to clearly appear. The transfer of electrons across the junction reduces the electric field across the junction and thus decreases the electromagnetic couplings responsible for the redshift and hybridization of the dimer plasmons. The reduced interactions caused by electron tunneling in the cross-over regime are the primary reason why the hybridized quadrupolar dimer resonance does not appear for the $R=16$ dimer.

For separations below $d=3$ Bohr, the CTP regime, the conductance of the junction is large. A clear blueshifting CTP appears at an energy around 5 eV. For this mode, the plasmon oscillations involve both a polarization of the electron distribution of the individual nanospheres and a flow of electrons between the nanospheres.[77] The CTP is significantly broader than the classical dimer plasmons due to the dissipation caused by the finite junction conductivity.

In Fig. 5.3 we report the energies of the dimer plasmon resonances as a function of separation distance, as extracted from Fig. 5.2. The TDDFT calculations are compared with the exact result from the classical PH approach.[94] It is clear that for large separation distances the plasmonic behavior approaches the classical result. For the smaller dimer, the quantum mechanical calculations begin to differ from the

classical ones at around $d/R=0.5$. For the larger dimer, this starts to happen at around $d/R=0.4$. This is consistent with the finding of the onset of charge transfer at separations d around 10 Bohr. In this crossover regime, the redshift of the dipolar dimer plasmon with decreasing dimer separation is smaller than the classical result. For the $R=16$ dimer, the plasmon energy displays a nonmonotonic behavior. This is caused by small changes of the electronic structure of the dimer and will be discussed in more detail below. In the CTP regime ($d/R < 0.15$), the particles are sufficiently close such that a significant charge current can flow between them. As a result, the plasmon modes blueshift rapidly with decreasing separation, as demonstrated also in classical calculations.[77, 47]

In Fig. 5.4 we show the self-consistent Kohn-Sham potential U_{KS} (see eq. 2.8) and electron charge density for the $R=24$ dimer in the three different regimes of interaction. The figure shows that in the classical regime ($d > 10$ Bohr), a significant potential barrier is present between the two nanospheres. The electrons can therefore not tunnel between the two nanoparticles. The charge density plots show that no electrons are present in the junction. Hence, the plasmonic response can be understood in terms of the hybridization of the neutral nanosphere plasmon modes. In the crossover regime ($10 < d < 4$ Bohr), the potential barrier is narrow and a small but finite electron density is present in the junction. As the external electric field is imposed on the dimer, the Fermi energies of the two nanospheres are shifted harmonically with respect to each other. Thus, electrons in occupied states of one nanosphere can tunnel into unoccupied states of the other nanosphere. The conductance of the junction forming between the two nanospheres is determined by the number of conducting channels and their tunneling coefficients. Both quantities depend sensitively on the shape of the tunneling barrier and on the relative spacings between the energy levels near the Fermi energy. The non-monotonic redshift of the $R=16$ dimer

plasmon in the crossover regime seen in Fig. 5.3 is caused by small changes in the level spacings near the Fermi energy, as the separation distance d is varied. In the CTP regime ($d < 4$ Bohr), the potential barrier lies below the Fermi energy and the electron density in the junction is large. Thus, electrons can flow freely between the two particles, leading to a junction conductance equal to the number of conducting channels times the unit of quantum conductance (e^2/h).

5.2 Field Enhancements

Further insight into the role of quantum mechanical effects for dimer plasmons can be gained by analyzing the electromagnetic field enhancements in the different regimes of interaction. In Fig. 5.5 we show the field enhancements for dimers at various separations. At the top of the figure, the maximum field enhancement in the junction for each separation distance studied, in both the classical and quantum pictures, is shown. Here it is clear that the classical and quantum descriptions diverge as the interparticle separation is reduced. The corresponding near field plots for the classical (top row) and quantum (bottom row) descriptions for these for interparticle separations are shown. With the classical approach, the field enhancements grow monotonically as the separation distance becomes smaller, becoming extremely large at small interparticle distances. The quantum mechanical model reveals a distinctly different behavior than the classical picture in the crossover and CTP regimes. In the classical regime ($d > 10$ Bohr), however, the field enhancement distributions are quantitatively similar. The maximum field enhancement in the center of the junction calculated using TDDFT is 13, which compares very well with the PH result of 16. In the outer part of the crossover regime, at $d=8$ Bohr, the maximum field enhancement calculated using TDDFT is 30, while PH gives 36. For $d=4$ Bohr, which is deep into the crossover regime, the quantum calculation gives a maximum

field enhancement of 35, which is significantly smaller than the classical enhancement of 65. For $d=2$ Bohr, which is in the CTP regime, the TDDFT enhancement is only 22 while the PH prediction is 110, a factor of 5 divergence between the two descriptions. Our investigation of the electromagnetic field enhancements clearly shows that quantum mechanical effects can play a major role in reducing the field enhancements in nearly touching nanoparticle dimers.

Although the present model calculations were performed for two small systems they yield consistent results, allowing us to deduce a qualitative and semi-quantitative picture of the plasmonic response. For larger nanoparticle systems, the spacing between the discrete electron energy levels is smaller, thus allowing for more conducting channels between the two nanospheres. In this case, it is very likely that the separation distance defining the outer boundary of the crossover regime will shift slightly to separation distances as large as $d=15$ Bohr. Such a jellium edge separation would correspond to a physical nanoparticle separation of 1 nm. Another factor that is likely to further extend the crossover boundary is the electron image potential. The present calculation was based on the local density approximation, which cannot describe the electron image potential outside the surface. The electron potential barrier between the two nanoparticles is therefore too sharp, leading to unphysically small electron tunneling rates between the two systems.[95]

Our calculations confirm that for large nanoparticle separation distances, the quantum calculations agree with the predictions of the classical approach for both plasmon energy and field enhancement. However, for nanoparticle separations smaller than 1 nm, quantum mechanical effects begin to significantly influence the plasmonic response of the dimer. The major effect is the onset of electron tunneling between the two nanoparticles, resulting in significantly smaller hybridization and a strong reduction of the electromagnetic field enhancements across the junction. For separa-

tions smaller than 0.5 nm, a charge transfer plasmon appears which blueshifts with decreasing interparticle separation.

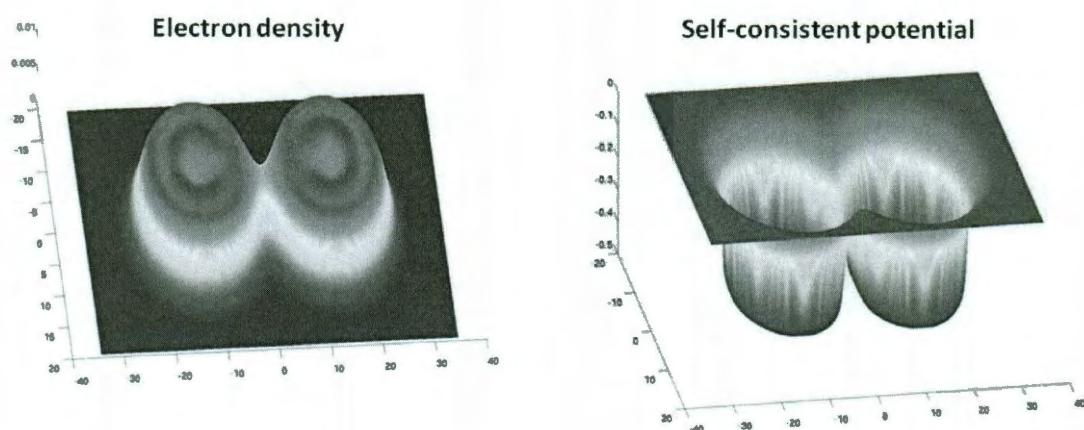


Figure 5.1: Equilibrium electron density (left) and self-consistent effective Kohn-Sham potential (right) for a nanosphere dimer of sphere radii $R = 12$ Bohr and interparticle separation $d = 1$ Bohr.

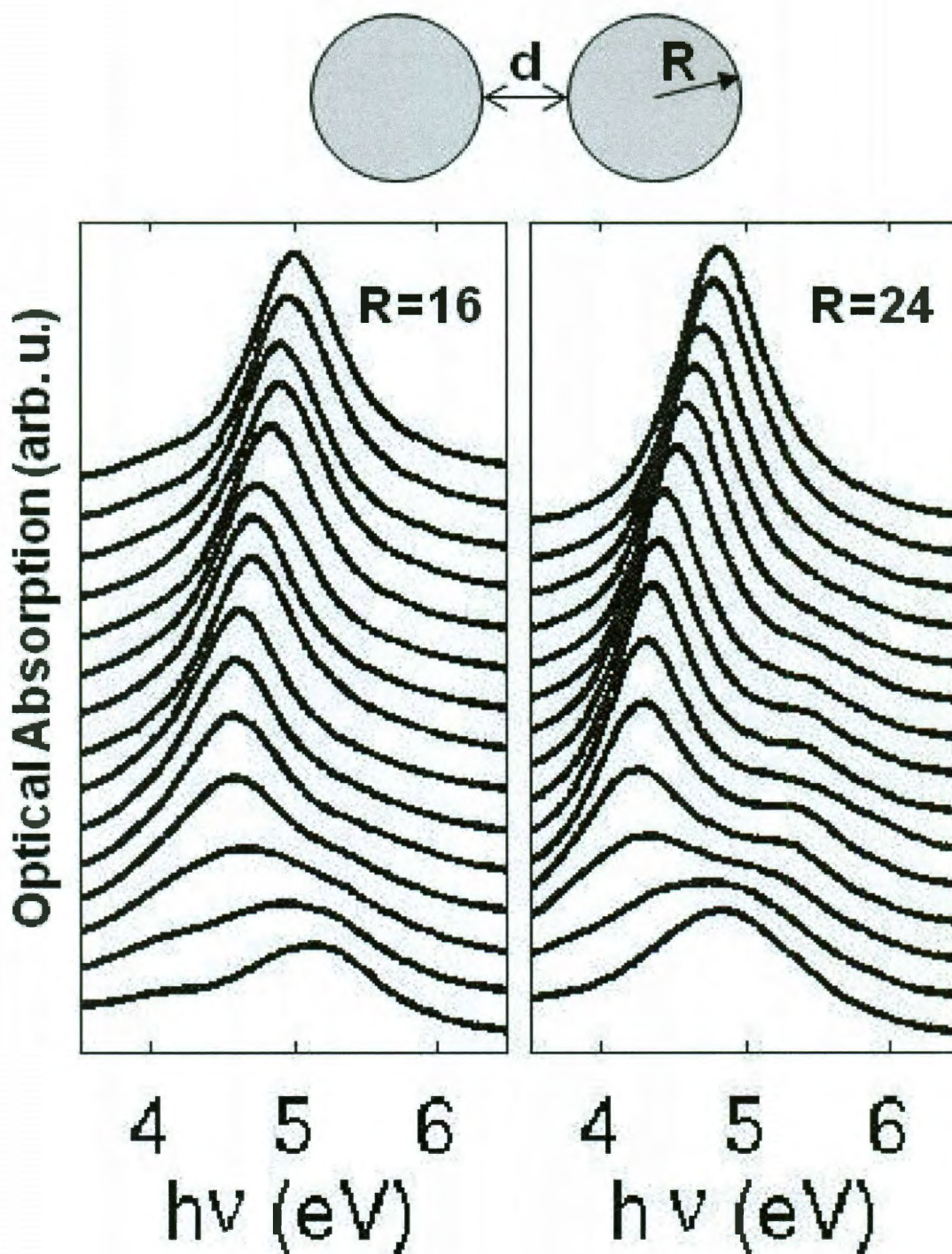


Figure 5.2: TDDFT absorption spectra for the $R=16$ Bohr (upper panel) and $R=24$ Bohr (lower panel) for different separations $d=0, 1, 2, 3, 4, 5, 6, 7, 8, 10, 16$ and 24 Bohr (from bottom curve and up). The spectra were calculated using an energy broadening of $\delta=0.27$ eV.

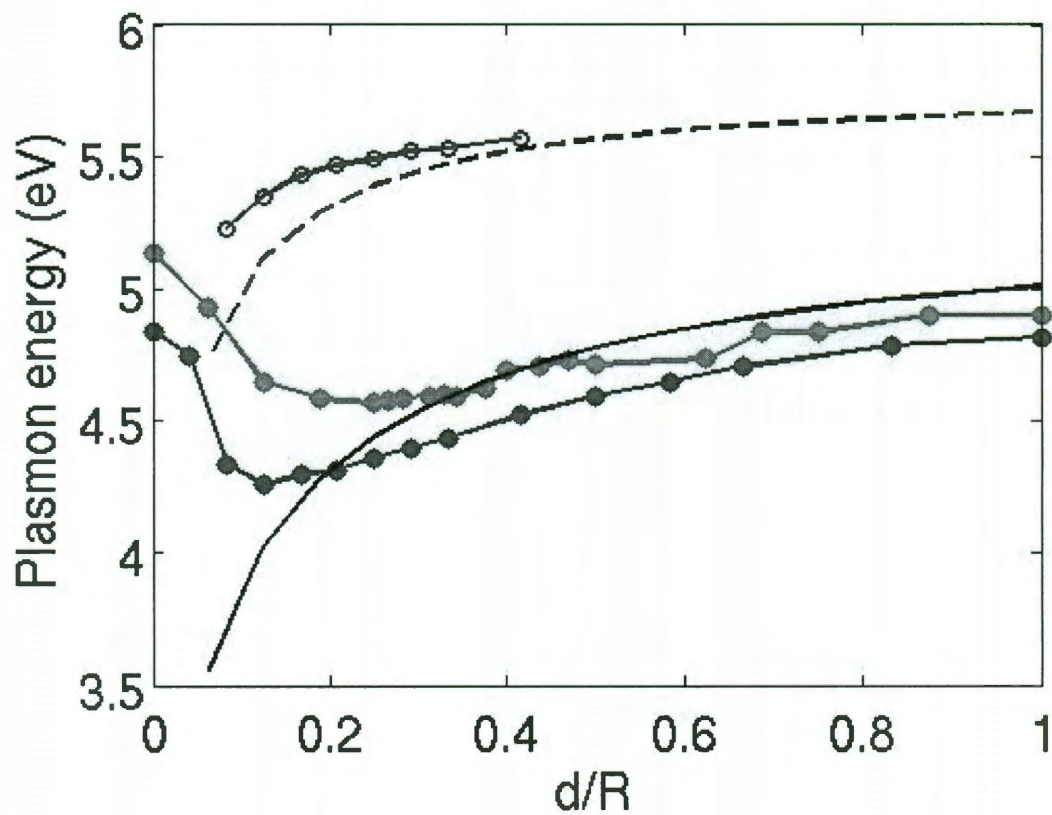


Figure 5.3: The dipolar (full circles) and quadrupolar (open circles) dimer plasmon energy as a function of d/R for of $R=16$ Bohr (red) and 24 Bohr (blue) sphere dimers calculated using TDDFT. The PH result is shown with solid (dipolar) and dashed (quadrupolar) lines.

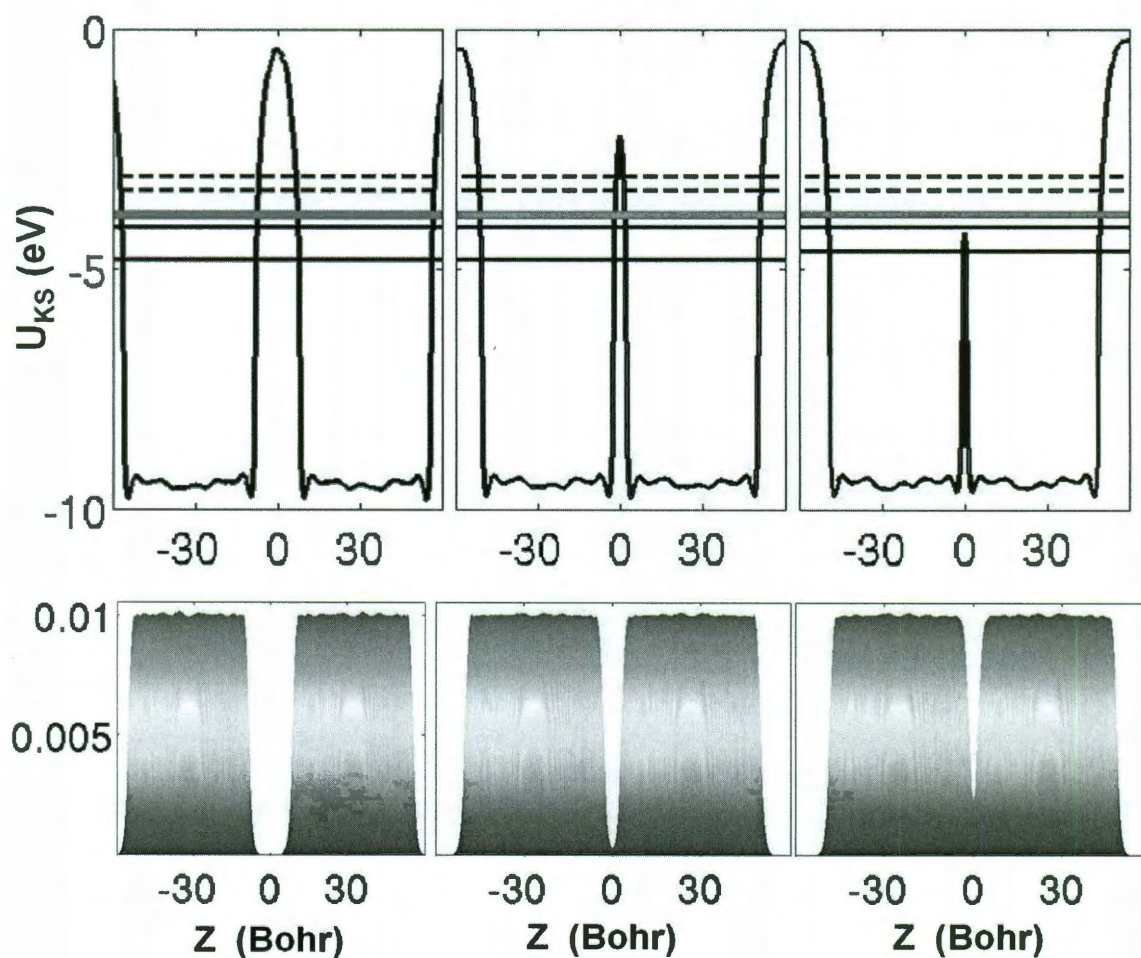


Figure 5.4: The self-consistent effective Kohn-Sham potential U_{KS} (upper row) and electron charge density $n(z)$ (lower row) along the symmetry axis, for $R=24$ Bohr and $d=16$ (left), 5 (middle) and 2 Bohr (right). The red horizontal lines mark the Fermi level. The solid horizontal lines are the energies of the the 60th and 30th occupied state below the Fermi energy. The dashed horizontal lines are the energies of the 30th and 60th unoccupied states above the Fermi level.

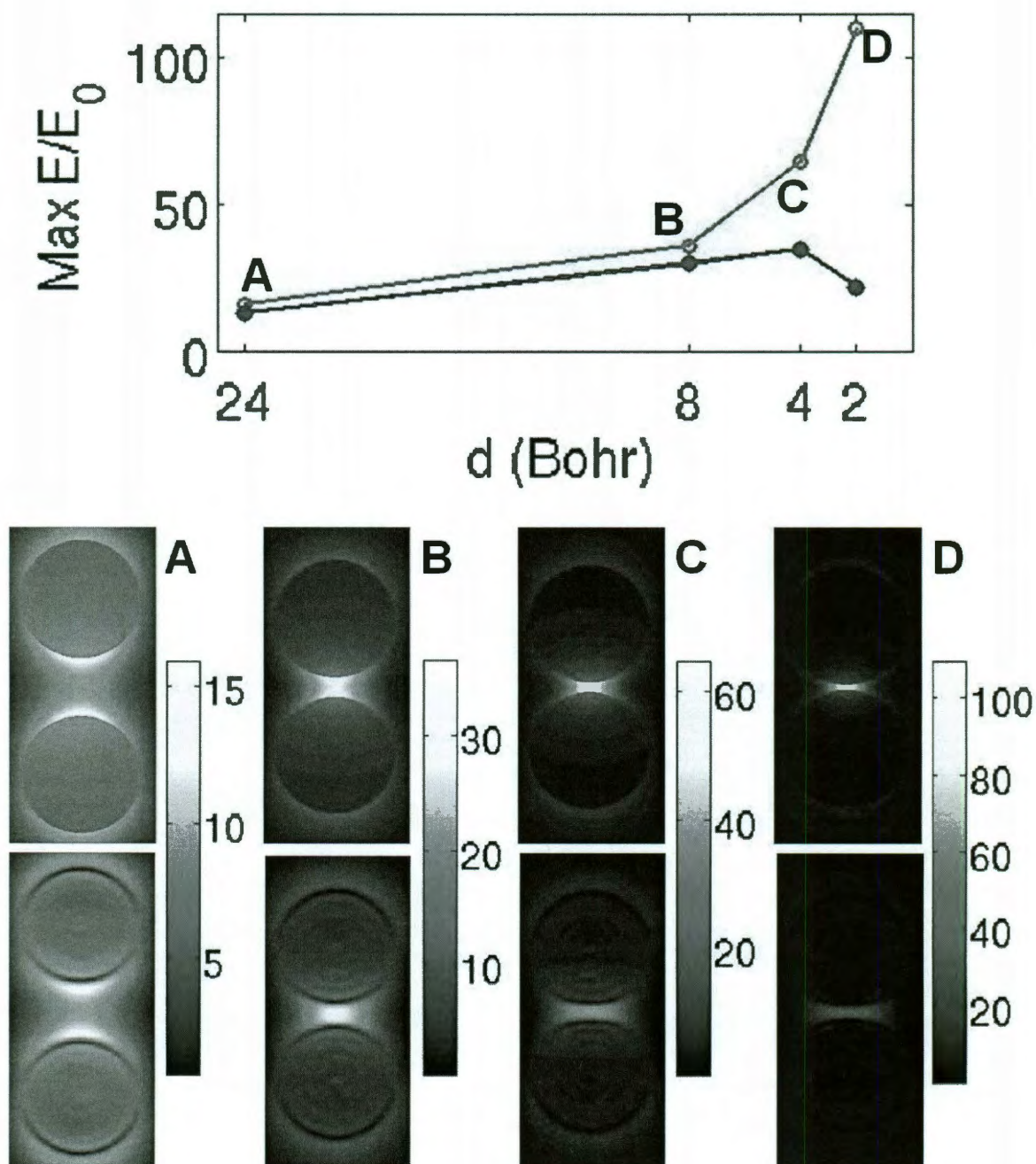


Figure 5.5: The upper panel show a comparison of the maximum electromagnetic field enhancements calculated using PH (red) and TDDFT (blue) for $R=24$ Bohr dimers of separations $d=24$ (A), 8(B), 4(C) and 2 Bohr (D). The lower panels compares the field distributions calculated using PH (top panels) and TDDFT (bottom panels). The field enhancements were calculated for resonant excitation of the dipolar dimer plasmon using a broadening of $\delta=0.27$ eV.

Other Geometries

We have looked at the plasmonic properties of both single particle systems and nanoparticle dimers. In chapter 4 we learned that classical calculations accurately predict the plasmon peak positions for single nanorods. The field enhancements at separations larger than about 1 nm from the nanorod surface are also described accurately by classical electromagnetic models. It is in the close vicinity of the surface that the predictions of classical electromagnetism overestimate field enhancement values. For nanoparticle dimers (chapter 5) we have learned that neither the absorption spectra nor the field enhancements can be accurately modeled within a classical framework for small interparticle separations. These insights lead us to conclude that special care must be taken in modeling plasmonic properties near metallic surfaces or in situations where two or more surfaces are in close proximity. In this chapter we will study two more relevant geometries where such situations occur and special care must be taken in their investigation.

6.1 Nanoeggs to Nanocups

We have seen how one of the most popular varieties of easily tunable nanoparticles is the nanoshell (a uniform metallic shell surrounding a spherical dielectric core), which has been widely used in applications. [29, 30, 31] The plasmon frequency of a nanoshell can be tuned by controlling the ratio of the shell thickness with respect to the overall particle diameter. A nanoshell's plasmon frequency can also be tuned by displacing the inner core within the shell, yielding symmetry broken non-concentric shells, or 'nanoeggs'. When displacements of the core are larger than the shell thickness we get altogether new particles with different properties: 'nanocups'. The properties of nanoshells, nanoeggs, and nanocups have been extensively investigated. [61, 42, 43] The transition between the three kinds of particle (accomplished by a gradual displacement of the core with respect to the metallic shell) drastically changes the optical behavior and is the subject of a recent study.[96] So far, theoretical investigations of all three varieties of this core-shell geometry, as well as of the transition between them, have been mostly limited to modeling based on classical electromagnetic simulations. The transition from nanoeggs to nanocups involves metallic surfaces (inner core and outer shell) positioned at very short separations from each other. In Fig. 6.1 we illustrate the transition from a perfectly concentric nanoshell, to a nanoegg, to a nanocup, by plotting the calculated electron density of such a system for different core displacements. Theoretically modeling the such a situation within a purely classical picture is bound to provide results that leave out important quantum effects. Here we will investigate the nanoegg to nanocup transition within a purely quantum mechanical framework and compare the results with traditional classical approaches.

To start our analysis, we look at the tunability of core-shell particles by calculating the plasmon energy as a function of core displacement. It is well known that for larger core displacements, nanoeggs have more red-shifted plasmon resonances. The oppo-

site is true once we get to the nanocup regime, where larger core displacements correspond to blue-shifts in the resonances.[97, 96] We begin with a perfectly concentric gold nanoshell of inner radius $R_{in} = 12$ Bohr, outer radius $R_{out} = 24$ Bohr, and a vacuum core. We define the dimensionless displacement parameter $D = d/(R_{out} - R_{in})$, where d is the physical distance that the core is displaced from the center. Since nanoeggs are known to display a remarkably small orientation dependence,[97] we will focus on the case where light is polarized along the azimuthal axis of symmetry of the particles. In Fig. 6.2 the lowest energy plasmon mode is plotted as a function of the displacement parameter D . The energies obtained from classical electromagnetic calculations are shown in red; quantum results are shown in blue. While the classical and quantum descriptions predict almost the same energies for concentric shells, in cases where the core is closer to the outer shell surface, classical calculations grossly overestimate the redshift in the plasmon energies.

For nanoeggs, the lowest energy plasmon mode is a bonding dipole excitation, where symmetric charges arise on the inner and outer shell surfaces. Displacing the core increases coupling between the surface and cavity modes, resulting in a redshift of the bonding plasmon energy. Classical calculations sustain shell and cavity modes even for arbitrarily small shell-cavity separations, where the strong coupling results in artificially large redshifts of the resonant frequency. This is seen in Fig. 6.2, where the classical plasmon energies drop drastically as $D \rightarrow 1$. For $D > 1$ we move into the nanocup regime, where increasing core displacements yield farther separated, duller edges, decreasing the coupling and blueshifting the plasmon energy. As we learned in chapter 4, discrepancies between classical and quantum descriptions of plasmons are more marked around sharper tips. This trend is confirmed in Fig. 6.2: classical nanocups within the $1 < D < 2$ regime have strongly interacting, sharp edges leading to much lower energies than what a quantum description predicts, with its screened,

smoothed out surface charges.

We now look at the field enhancements for the particles studied in Fig. 6.2. In Fig. 6.3 we plot the field enhancements 0.5 Bohr outside the surface in the direction of the core displacement. For nanoeegs, displacements of the core bring the cavity surface charges closer to the shell, increasing field enhancements in that region. Classical calculations have shown that positioning the core at small separations from the outer surface gives rise to very large field enhancements[96], an effect that is confirmed in Fig. 6.3. As $D \rightarrow 1$, the classical enhancements become unphysically large. For such cases, large hybridization between shell and cavity plasmons strengthens multipolar excitations, for which the largest field enhancements are obtained. In the quantum description, as $D \rightarrow 1$ and the metal layer between the core and the shell becomes increasingly narrow, electrons are forced out of this region, leaving a lack of surface charges that results in decreased field enhancements. In this picture, with no strongly coupled surface and cavity modes, there are no enhanced higher order modes that give rise to the large field enhancements predicted in classical calculations.

To more closely examine the coupling between the core and shell modes, we investigate the evolution of the optical absorption and field enhancements as a function of frequency as we increase core displacement. In Fig. 6.4 we compare the optical absorption spectra (left panels) and field enhancements (right panels) obtained by quantum (black curves) and classical (red curves) calculations. The figure reveals that for perfectly concentric shells (top panels), the both the absorption spectra and the field enhancements are dominated by the lowest order mode. For a larger core displacement of $d = 6$ (middle panels) we see the emergence of multipolar peaks in the spectra, but the dominant mode is still the lowest energy bonding dipole mode. As the core approaches the outer shell with a displacement of $d = 10$ (bottom panels) the core-shell coupling is increased, leading to the strengthening higher order modes.

For this case, we see how in the classical calculations the largest absorption and field enhancements do not occur for the lowest energy dipole mode, but for a higher order mode. This is because the large hybridization that results from the narrow core-shell separation intensifies higher order modes. A quantum description allows for electrons to be forced out of the narrow core-shell junction, reducing surface charges in that region and decreasing the coupling between the shell and cavity modes. It is the natural electron distribution in this geometry that reduces coupling; not accounting for this in a calculation intensifies higher order modes which give rise to unphysical field enhancements. The reduced shell-cavity coupling in this quantum picture is manifested by the dominance of the lowest energy dipole mode over higher order modes, both in the optical absorption and in the field enhancements.

It is also of interest to analyze the spatial distribution of the field enhancements. In Fig. 6.5 we plot the enhancements for both a perfectly concentric nanoshell (left panels) and for a $D = 10/12$ nanoegg (right panels). In the classical picture (top panels), the enhancements arise as a result of two dimensional surface charges in the metal. Quantum mechanically (bottom panels) we account for a three dimensional spatial distribution of screening charges, spilling to the outside of the shell and to the inside of the core cavity. The more localized surface charges give rise to larger enhancement values at short separations from the surface, an effect that has been previously demonstrated in other geometries (chapter 4). Although the enhancement hot spots are larger in the classical description, the area over which they are spread is larger in the quantum picture, where the screening charges are distributed in three dimensions.

We have seen how the transition from nanoshells, to nanoeggs, to nanocups is one in which quantum effects can significantly modify plasmonic properties. Our results show that a classical description significantly overestimates the shifts in plasmon

peaks with core displacements. In the classical description, both shell and cavity modes are supported even for arbitrarily narrow shell-cavity separations, giving rise to large coupling which enhances multipolar modes with large absorption and field enhancements. A quantum mechanical description is needed to account for a realistic electron density in narrow shell-cavity junctions, giving rise to modified, screened field enhancements.

6.2 Nanomategyoshkas

We will now discuss a nanoparticle geometry with new found popularity due to its ideal use for surface-enhanced Raman scattering (SERS). This kind of particle, the “nanomategyoshka”, consists of a spherical metallic sphere surrounded by a dielectric layer, which in turn is surrounded by a spherical metallic shell. An schematic illustration of this geometry is depicted in Fig. 6.6. A recent study has shown that DNA on gold nanoparticles facilitates the formation of well-defined gold nanogaps that generate a highly stable and reproducible SERS signal. [98] The study described how to apply this technique to fabricate nanomategyoshka-type particles that generate enhancement factors sufficient for single-molecule detection. These particles can be synthesized with uniform and reproducible nanogaps of the order of 1 nm between the inner metallic sphere and the outer shell. It is natural that quantum effects may modify plasmonic properties of nanomategyoshka-type particles if the core-shell nanogap is sufficiently narrow to allow electron tunneling. Our aim here will be to show that for metallic nanomategyoshka-type particles, the evolution of the spectra and plasmon modes may be significantly modified by quantum effects. We show that such effects will lead to behavior that deviates from classical electrodynamic predictions.

As explained earlier in this work, we will do our TDDFT calculations within the jellium model. We will neglect the background polarizability of the metal and focus

on the effects mediated by the coupling of the electrons on the core and the shell. The dimensions specified for our particles refer to the dimensions defined by the jellium background, which are half a lattice space larger than the physical sizes of the nanoparticles. For noble and simple metal crystals, the spacing between close-packed planes is typically around 5 Bohr. Our specified gap thickness d refers to the separation of the core and shell jellium edges. Thus, the physical gap thickness D is related to d as $D + 5$ Bohr.

We will start our analysis with a nanomatryoshka of center sphere radius $r_c = 14$ Bohr, and outer shell inner and outer radii of $R_{s1} = 18$ and $R_{s2} = 24$, respectively. We scale down the particle dimensions dividing by a constant λ , so that the scaled dimensions are given by $(r_c, R_{s1}, R_{s2})/\lambda$. In the left panels of Fig. 6.7 we show the electron density calculated for particles of dimensions $(r_c, R_{s1}, R_{s2})/\lambda = (14, 18, 24)/\lambda$ Bohr, for $\lambda = 1, 2, 3$. The right panels show the corresponding optical absorption for each particle size. For the case of scaling constant $\lambda = 1$, the core-shell nanogap is 4 Bohr thick, still within the crossover regime, so no significant charge current can flow through the gap. The electron density plot for the $\lambda = 1$ case shows no significant electron density overlap, and the absorption spectra shows the three distinct peaks predicted by classical electrodynamics. For scaling constant $\lambda = 2$, the nanogap thickness is reduced to 2 Bohr and brought within the CTP regime. The electron density for this case shows significant overlap between the core and the shell and we see the onset of a merging between the three distinct modes in the absorption spectra. The particle starts resembling a single solid sphere as a result of the large conduction between the core and the shell. Using a scaling constant of $\lambda = 3$ completely blurs the core-shell boundary. The particle behaves like a single sphere of varying density, and the absorption spectra starts resembling that of a single sphere.

For small nanoparticles within the quasistatic regime, electromagnetic interac-

tions are scale invariant within a classical formulation; i.e., in the classical regime the nanomatryoshka plasmon resonances only depend on the relative dimensions between the inner sphere and outer shell, so particles of dimensions $(r_c, R_{s1}, R_{s2})/\lambda$ have the same absorption spectra for all λ . We have seen that in a quantum mechanical formulation this is not the case and, as the particles are scaled down, charge conductance is established in the gap and the optical properties are significantly modified.

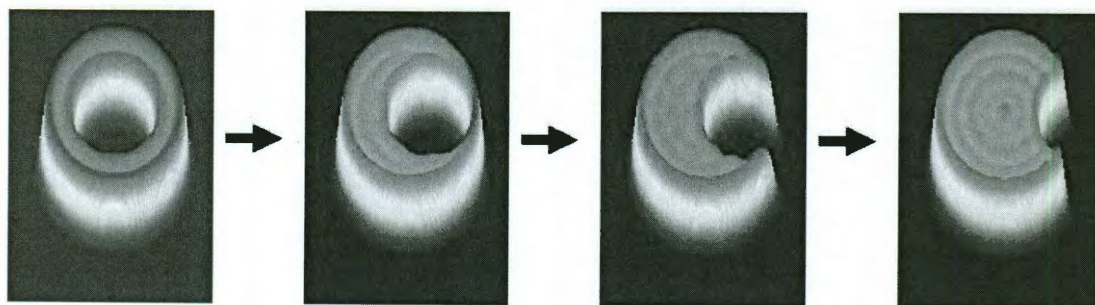


Figure 6.1: Calculated electron density for a nanoshell to nanoegg to nanocup transition. We start with a perfectly concentric nanoshell of inner radius 12 Bohr and outer radius 24 Bohr and gradually increase the core displacement: $d = 0, 9, 14, 27$ (from left to right).

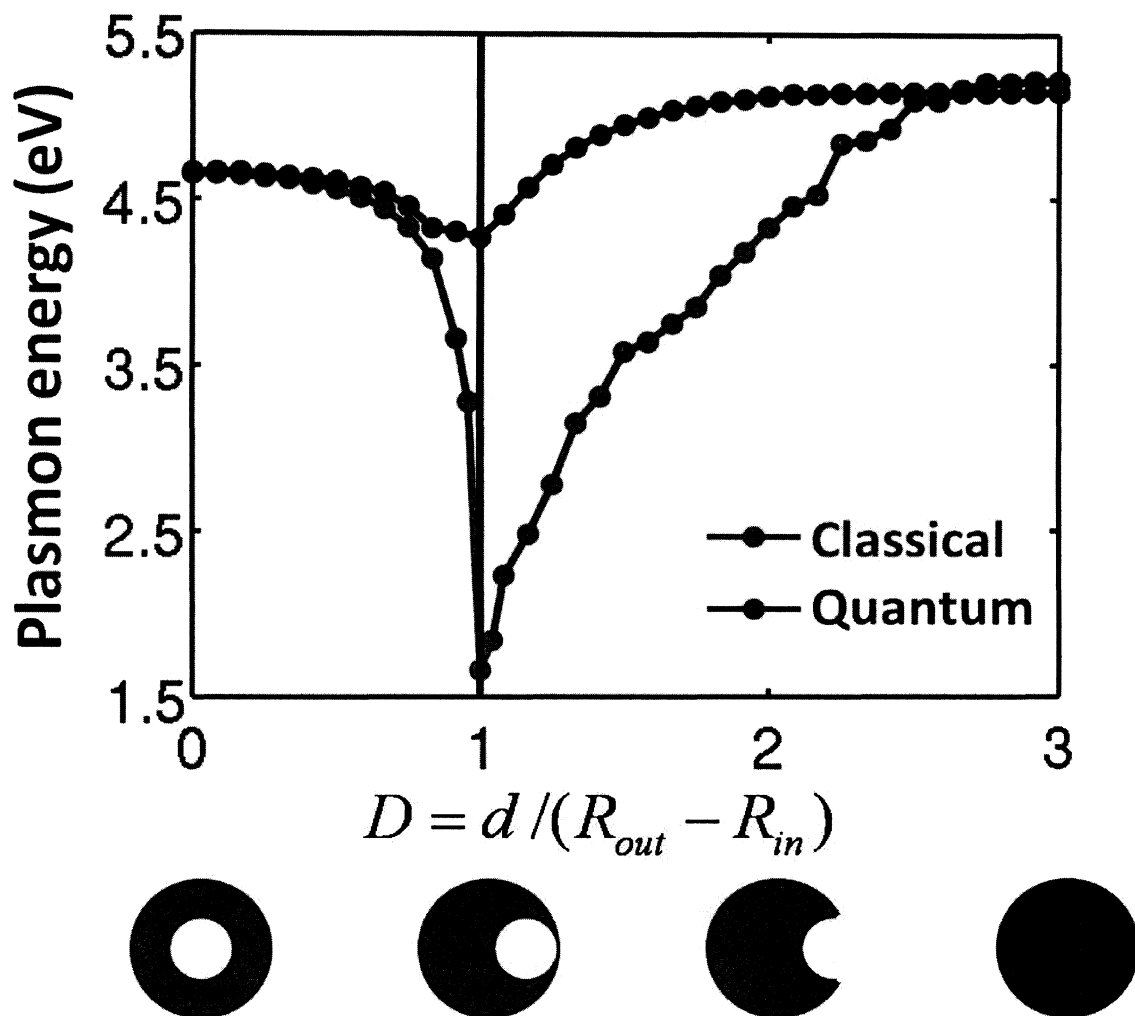


Figure 6.2: Lowest plasmon energy as a function of core displacement parameter $d/(R_{out} - R_{in})$ for a core-shell particle with outer radius $R_{out} = 24$ Bohr, inner radius $R_{in} = 12$ Bohr, and a vacuum core. The excitation polarization is aligned with the azimuthal axis of symmetry of the particles. The number of electrons in the particle ranges from 444 for the $d = 0$ concentric nanoshell to 507 for $d = 36$ solid sphere. The red curve shows the classical calculations and the blue curve shows the quantum results.

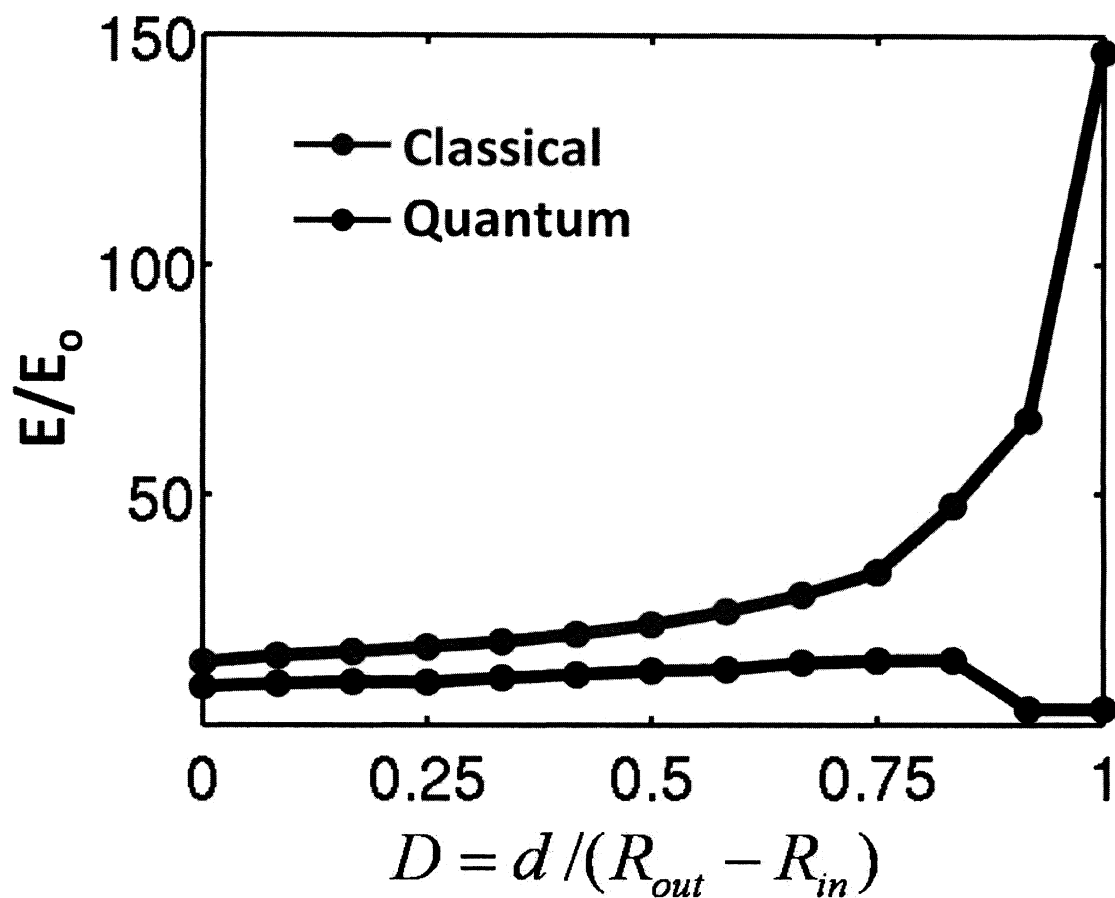


Figure 6.3: Electromagnetic field enhancements as a function of core displacement parameter D for a core-shell particle with outer radius 24 Bohr and core radius 12 Bohr. The red curve shows the classical calculations and the blue curve shows the quantum results. The enhancements are plotted for a point 0.5 Bohr outside the particle surface in the direction of core displacement.

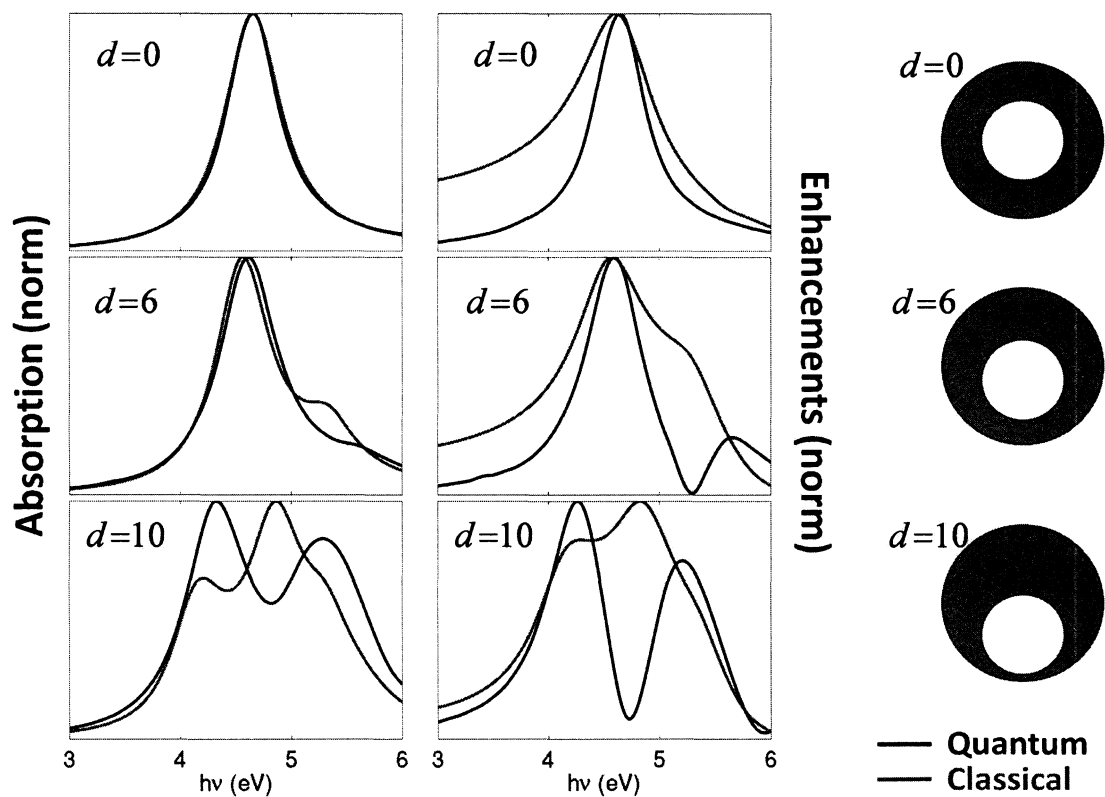


Figure 6.4: Optical Absorption (left panels) and field enhancements (right panels) as a function of frequency for core-shell particles with core displacement $d = 0$ (top), $d = 6$ (middle), and $d = 10$ (bottom). The quantum results are shown in black and the classical results are shown in red.

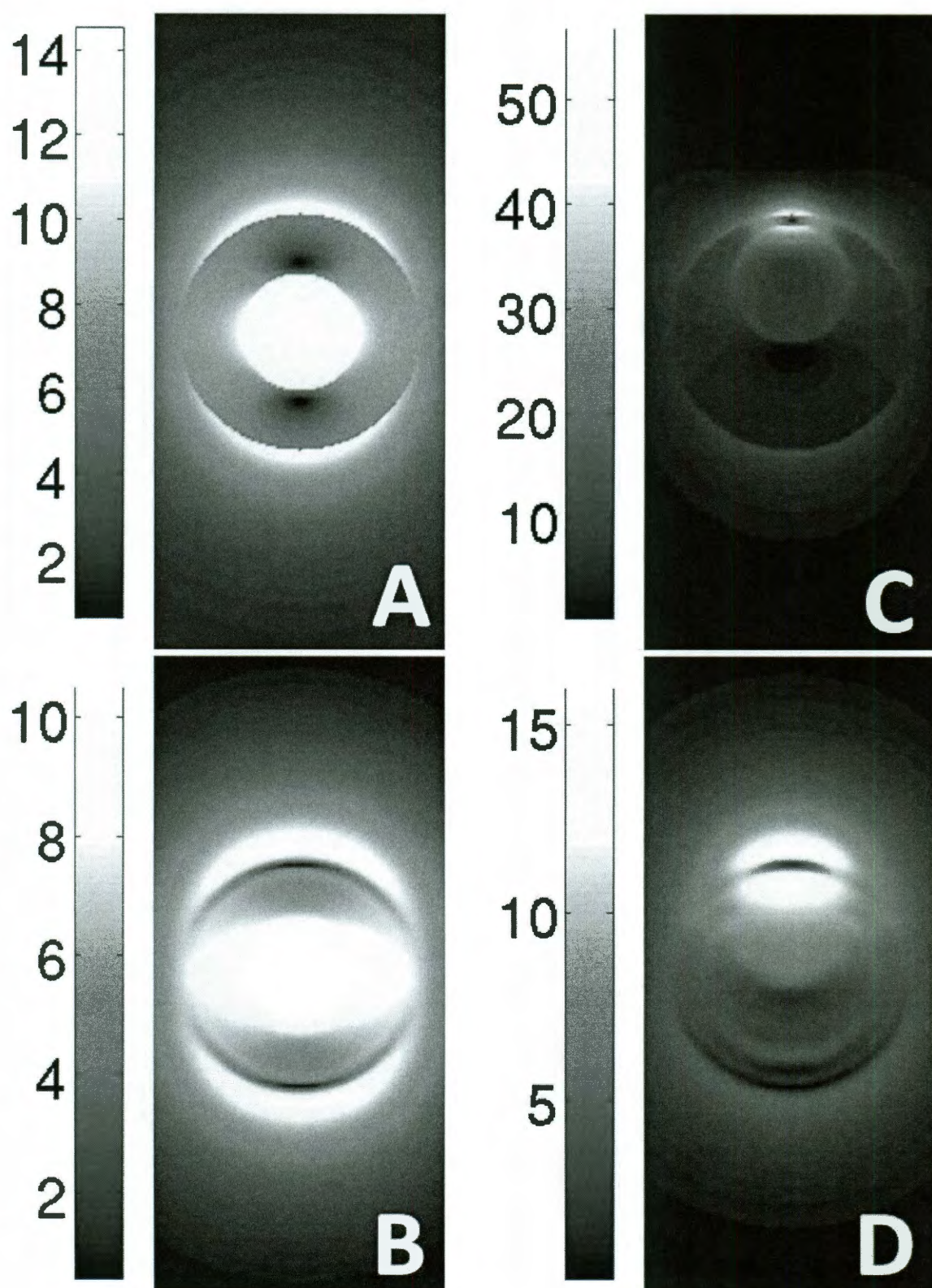


Figure 6.5: Field enhancements for a core-shell particle with outer radius 24 Bohr, core radius 12 Bohr, and core displacement of $d = 0$ Bohr (left panels) and $d = 10$ Bohr (right panels). The top panels show the classical results and the bottom panels show the quantum results.

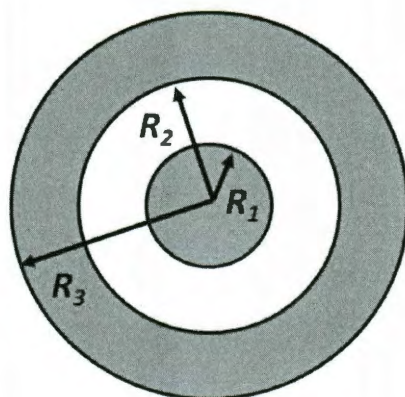


Figure 6.6: Schematic illustration of a nanomatyoshka. This particle consists of a metallic sphere surrounded by a dielectric layer, which in turn is surrounded by a spherical metallic shell.

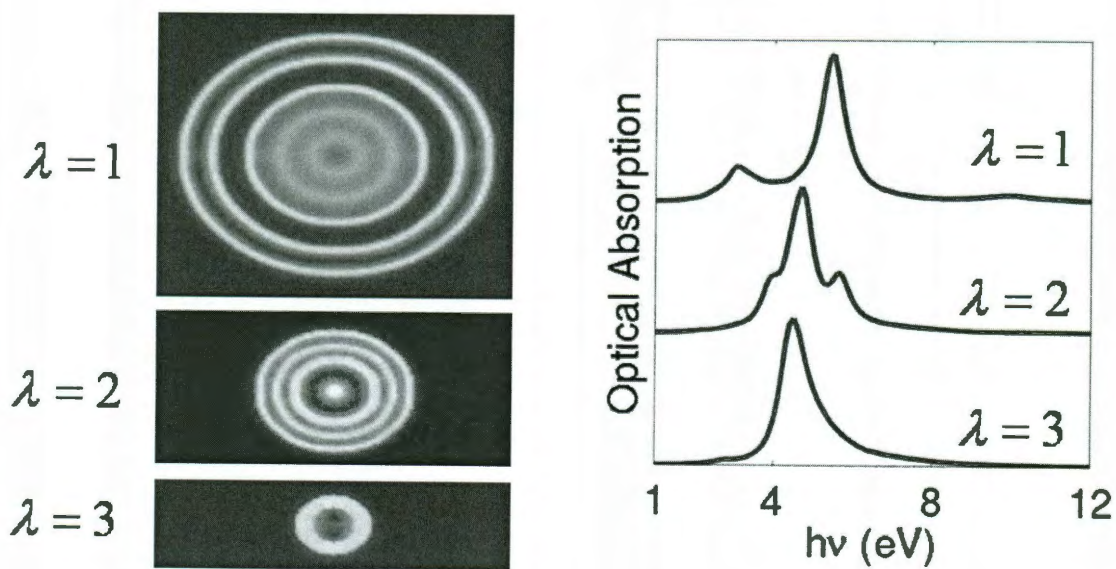


Figure 6.7: Calculated electron density (left panels) and optical absorption spectra (right panels) for nanomatyoshkas of size $(r_c, R_{s1}, R_{s2})/\lambda = (14, 18, 24)/\lambda$ Bohr, for $\lambda = 1, 2, 3$.

Conclusions

The present study provides a thorough microscopic understanding of the electronic structure and optical properties of novel nanostructures. Our formulation of the time-dependent density functional theory formalism in a way that allows the treatment of azimuthally symmetric systems has opened the doors for the investigation of important new structures. An efficient computational implementation of the theory has made it possible to do *ab initio* studies of electronic structure and optical absorption calculations for nanoparticles that are large enough to display collective electron oscillations and surface plasmon modes.

For simple single nanoparticle systems, such as nanorods or nanoshells, classical electrodynamic descriptions accurately predict plasmon peak positions and optical absorption spectra. The field enhancements for such systems are also accurately modeled by classical descriptions for distances of more than about 1 nm from the particle surface. In the close proximity of the particle surface (< 1 nm), a classical description overestimates the value of the field enhancements and realistic electron density distributions must be taken into account to accurately model electromagnetic field enhancements.

When studying more complex nanostructures that display metallic surfaces in

close proximity to each other, quantum effects, such as electron tunneling and screening, may drastically reduce electromagnetic field enhancements and significantly modify plasmon resonant frequencies. Outside of such closely-touching regimes, classical descriptions make accurate predictions that match experimental results. We have compared fully quantum mechanical and classical electrodynamical descriptions for a wide variety of nanostructures of interest, including nanoshells, nanorods, nanoparticle dimers, nanomatryoshkas, nanoeggs, and nanocups, and we have clearly identified the limits of validity of traditional classical models.

The bulk of this thesis is devoted to a thorough first-principles investigation of electronic structure and optical properties of metallic nanoparticles. Here we indulge in a brief excursion into classical territory.

8.1 Enhancements are red, absorption is blue, their shift is deciphered and quantified too

The field of plasmonics has been largely concerned with studying and designing nanostructures with both tunable plasmon resonances and large field enhancements, to enable drastic increases in the cross section for surface enhanced spectroscopies such as SERS. One measure of the plasmonic response of a metallic nanoparticle or nanostructure commonly used involves its far-field quantities, such as absorption, scattering, and extinction. Another measure involves its near-field properties, such as the intensity and spatial distribution of its electromagnetic field enhancements.

A well-known phenomenon that has frequently been pointed out in the literature is that near-field properties peak at lower energies than the far-field quantities.[99,

100, 101] This redshift of the near-field peak energies with respect to the far-field peak energies is known to depend upon the size of the particle,[102, 103] with larger particles displaying a more marked shift. For large enough particles, this shift has been observed to be comparable to the resonance half-width.[103] A recent systematic study has provided a phenomenological comparison of the relationship between the near- and far-field spectra of plasmonic particles,[104] but a simple physical explanation of this apparently universal characteristic of these systems is still lacking.

Our goal here is to identify the physical origin of this shift. We will show that this universally observed phenomenon is a general and central consequence of the universal behavior of damped harmonic oscillators (HOs). Plasmons are damped HOs driven by the electric (and sometimes the magnetic) component of the incident light.[105, 106, 107, 108, 109, 110, 111, 112, 113, 114] The absorption maximum occurs at the resonance frequency of the oscillator. The plasmon-induced electric field enhancements are proportional to the plasmon-induced surface charges, which in turn are proportional to the plasmon amplitudes.[105] When damping is present for a HO, the maximum displacement amplitudes occur at a lower energy than the resonance frequency, with a redshift that depends on the damping. We will derive an analytical expression for this shift and compare it with exact electromagnetic calculations for the near- and far-field properties of plasmonic nanoparticles. We will explicitly show that intrinsic and radiative damping play a similar role in determining this shift and that the redshift is determined by the total damping as inferred from the width of the plasmon resonance in the far-field spectrum.

8.2 The Harmonic Oscillator Model

We start by analyzing a simple HO consisting of a particle of mass m on a spring with spring constant k and damping β , driven by an external force $F(t) = F_0 \cos(\omega t)$.

The displacement $x(t)$ of the particle from its equilibrium is thus governed by

$$m\ddot{x} = -kx - m\beta\dot{x} + F_0 \cos(\omega t). \quad (8.1)$$

For a plasmonic nanoparticle, the mass m would correspond to the total mass of the conduction electrons, the displacement parameter x corresponds to the plasmon amplitude, and k is the electromagnetic restoring force originating from the displacement of the conduction electrons.[105] In steady state, the motion is of the form:

$$x(t) = D(\omega) \cos(\omega t - \delta), \quad (8.2)$$

where the particle position will oscillate at the driving frequency ω , with an amplitude

$$D(\omega) = \frac{F_0/m}{\sqrt{(\omega_0^2 - \omega^2)^2 + (\beta\omega)^2}} \quad (8.3)$$

and a phase,

$$\tan(\delta) = \frac{\beta\omega}{\omega_0^2 - \omega^2}, \quad (8.4)$$

where $\omega_0 = \sqrt{k/m}$ is the resonance frequency of the oscillator (plasmon frequency). Equation (8.3) shows that the largest amplitude is obtained for a driving frequency of

$$\omega_{NF} = \sqrt{\omega_0^2 - \beta^2/2}, \quad (8.5)$$

i.e., redshifted from the natural frequency of the oscillator by an amount determined by the damping β . Indeed, this shift is consistent with our everyday experience. For example, for a mechanical oscillator placed in a viscous medium, the motion is slowed and one would have to drive it at a slower frequency to maintain large amplitude motion.

The energy absorbed by the oscillator is equal to the power delivered to the system:

$$P(t) = F(t) \cdot \dot{x}(t) = -F_0 D(\omega) \omega \cos(\omega t) \sin(\omega t - \delta). \quad (8.6)$$

Taking the time average of the power we find the average absorption per oscillation period:

$$\langle P(t) \rangle = \frac{F_0^2 \beta}{2m} \frac{\omega^2}{[(\omega_0^2 - \omega^2)^2 + (\beta\omega)^2]}. \quad (8.7)$$

Setting $d\langle P(t) \rangle/d\omega = 0$ we find that the average absorption is maximum at frequency $\omega = \omega_0$; that is, the absorption experiences a resonance at the natural frequency ω_0 of the oscillator.

A more detailed analysis shows that the time average of the kinetic energy in the oscillator takes the form

$$\langle T(t) \rangle = \frac{F_0^2}{4m} \frac{\omega^2}{[(\omega_0 - \omega)^2 + (\beta\omega)^2]}, \quad (8.8)$$

which is a Lorentzian centered at ω_0 and is directly proportional to $\langle P(t) \rangle$ from Eq. (8.7). In contrast, the time average of the potential energy is given by

$$\langle U(t) \rangle = \frac{\omega_0^2 F_0^2}{4m} \frac{1}{[(\omega_0 - \omega)^2 + (\beta\omega)^2]}, \quad (8.9)$$

which peaks at the same redshifted frequency $\omega_{NF} = \sqrt{\omega_0^2 - \beta^2/2}$, as the oscillation amplitude Eq. (8.3).

Since plasmons are examples of HOs, we expect that the above results derived for a simple HO model should apply also for the optical properties of plasmonic nanoparticles and nanostructures. Specifically, we expect that the intensity of the plasmon-induced near-field, which is proportional to the plasmon amplitude, should peak at a lower energy ω_{NF} than the maximum absorption, which occurs at the plasmon energy ω_0 . Since the scattering of a plasmonic nanoparticle is a consequence

of the acceleration of its conduction electrons, the far-field scattering and extinction cross sections should also peak at a similar frequency as the maximum kinetic energy, i.e at the plasmon energy. This coincidence has been observed in many previous studies.[99, 115]

To investigate how our simple model applies in realistic situations, we use Mie theory to calculate the near- and far-field properties of different metallic particles. For simplicity we employ a Drude model (DM) for the metallic permittivities

$$\epsilon(\omega) = \epsilon_{\infty} - \frac{\omega_B^2}{\omega(\omega + i\gamma)}, \quad (8.10)$$

where ϵ_{∞} corresponds to the background dielectric constant, ω_B is the bulk plasma frequency, and γ is the intrinsic damping parameter. To model Au we use $\omega_B = 8.9488$ eV, $\epsilon_{\infty}=9.5$, and $\gamma = 0.06909$ eV. To investigate the effect of intrinsic damping, we will also use larger γ in some calculations described below. The results presented here do not depend on this choice of the DM for the permittivity of the metal but also apply for realistic dielectric data.

In Fig. 8.1 we plot the far-field extinction cross section (blue curve) and the plasmon-induced near-field electromagnetic field enhancements (NFE) (black curve) calculated using Mie theory for a gold sphere of radius 12 nm. In this figure and in the following figures all spectra is normalized to unity to more clearly show the magnitude of spectral shifts. The peaks in the spectra correspond to the excitation of the dipolar Mie resonance. Such a small particle has minimal radiative damping and very little intrinsic damping, resulting in a negligible redshift of the near-field spectrum. In a situation where the damping would be larger, we would expect a larger redshift of the near-field spectrum. We now investigate the effect of radiative damping by considering a larger particle where retardation effects and consequently the radiative damping would be larger.

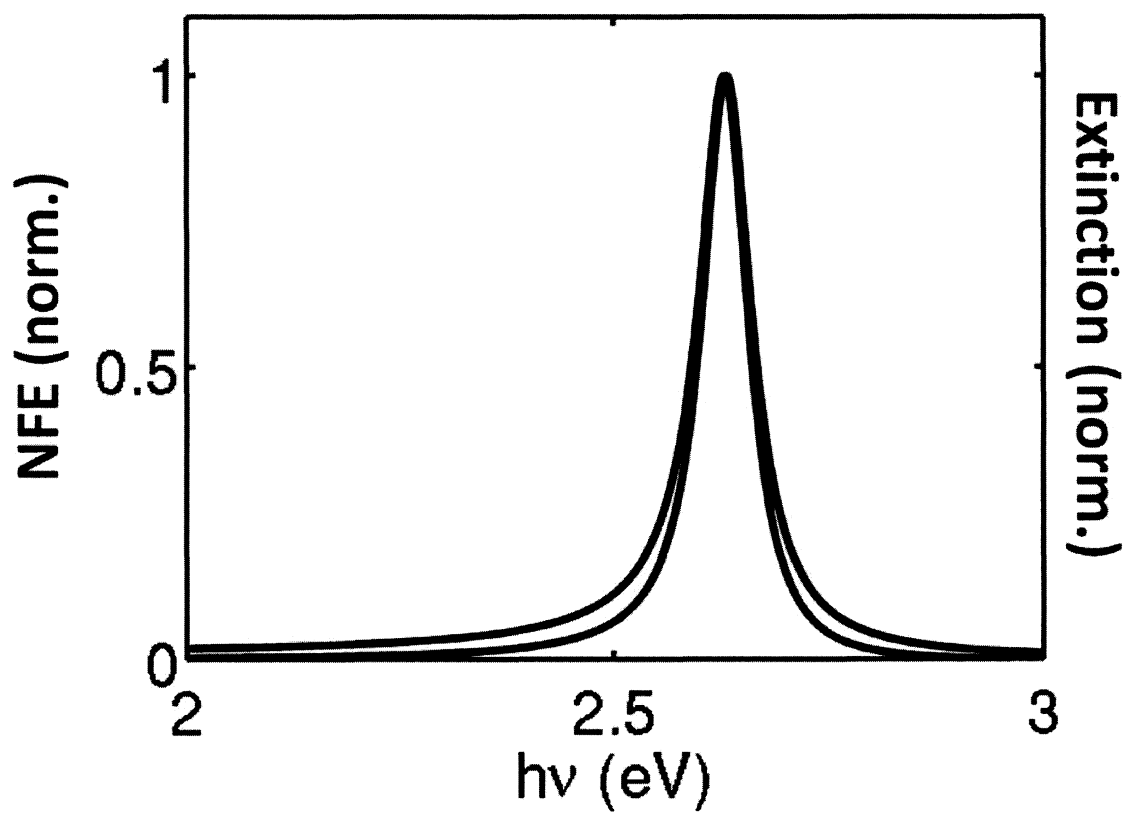


Figure 8.1: Mie extinction cross section (blue curve) and NFE (black curve) as a function of energy for a 12 nm radius gold (DM) sphere. Both spectra have been normalized to unity.

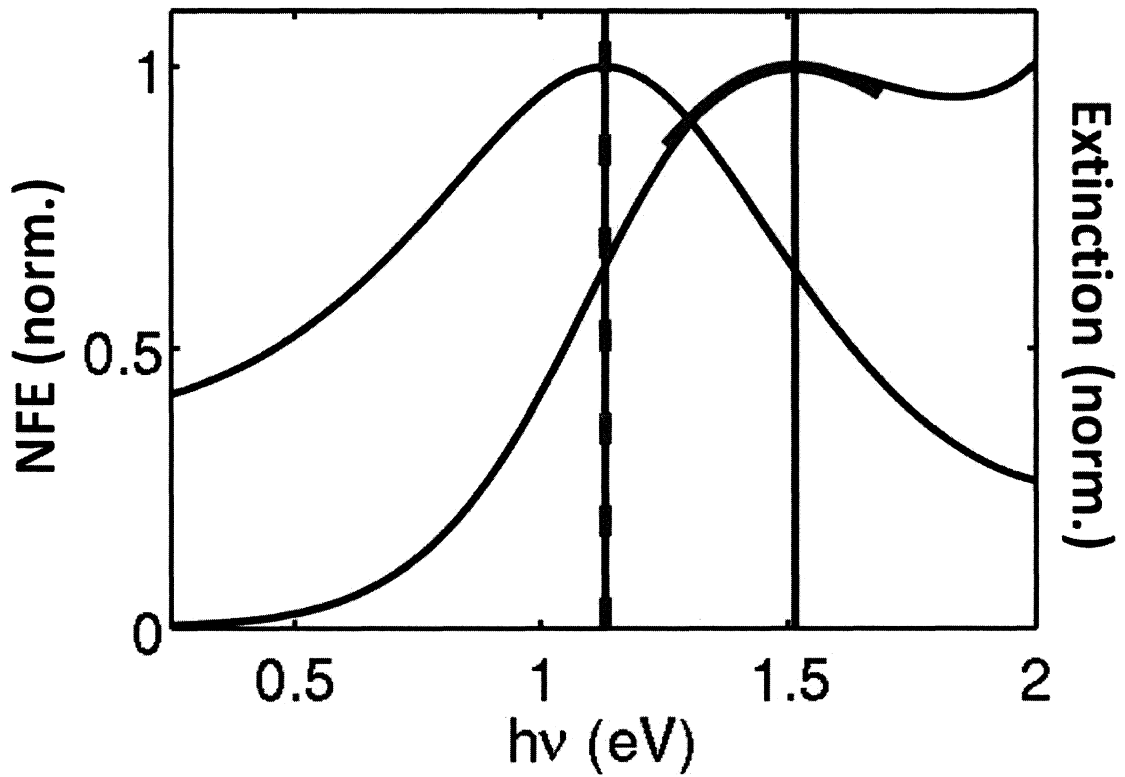


Figure 8.2: Mie extinction spectra (blue) and NFE (black) as a function of energy for a 150 nm radius gold (DM) sphere. The fit of the far-field peak to Eq. (8.7) is shown in red. The vertical black and blue lines denote the peak positions in the near-field and far-field spectra, respectively. The red dashed line denotes the energy ω_{NF} obtained using Eq. (8.5). The spectra have been normalized to unity.

In Fig. 8.2 we show the far-field extinction cross section (blue curve) and the NFE (black curve) for a gold sphere of radius 150 nm. For a particle of this size, retardation effects are prominent, resulting in both a redshift of the dipolar plasmon resonance and a significant broadening of the extinction peak due to radiative damping. The NFE spectrum is clearly redshifted from the far-field spectrum. The far-field spectra, obtained from rigorous electromagnetic calculations, can be fit by the Lorentzian absorption of a HO, Eq. (8.7) (red curve). The oscillator damping parameter β obtained from this fit is then used to calculate the peak position ω_{NF} of the plasmon-induced near-field through Eq. (8.5). This calculated ω_{NF} is shown with the dashed red line. The figure clearly shows that the redshift of the near-field spectra as predicted by the simple HO model is in almost perfect agreement with the result from Mie theory.

We now investigate how the intrinsic damping influences the redshift of the near-field spectrum. This can be accomplished by increasing the damping γ in the DM Eq. (8.10). In Fig. 8.3, the extinction spectra are shown for different polarizations for nanorods of aspect ratio 3 for two hypothetical metals with different intrinsic broadening. The figure clearly shows that the redshift of the near-field spectra increases with increasing intrinsic damping γ . As in Fig. 8.2, the plasmon damping β can be obtained by fitting the extinction spectra to the result for the HO model, Eq. (8.7) (red curves). Using these parameters, the results for ω_{NF} in Eq. (8.5) are shown with the dashed red lines. As in Fig. 8.2, the predicted redshifts of the near-field peaks are in almost perfect agreement with the results from electromagnetic calculations.

Finally, we consider a more complex plasmonic system. In Fig. 8.4 we show the extinction spectrum and NFE spectrum for a gold nanoshell calculated using Mie theory. The size of the nanoparticle is sufficiently large that both the broad dipolar plasmon around 1.5 eV and the much narrower quadrupolar plasmon around 2.3 eV are visible in the far-field spectrum. The calculated near-field spectrum also displays

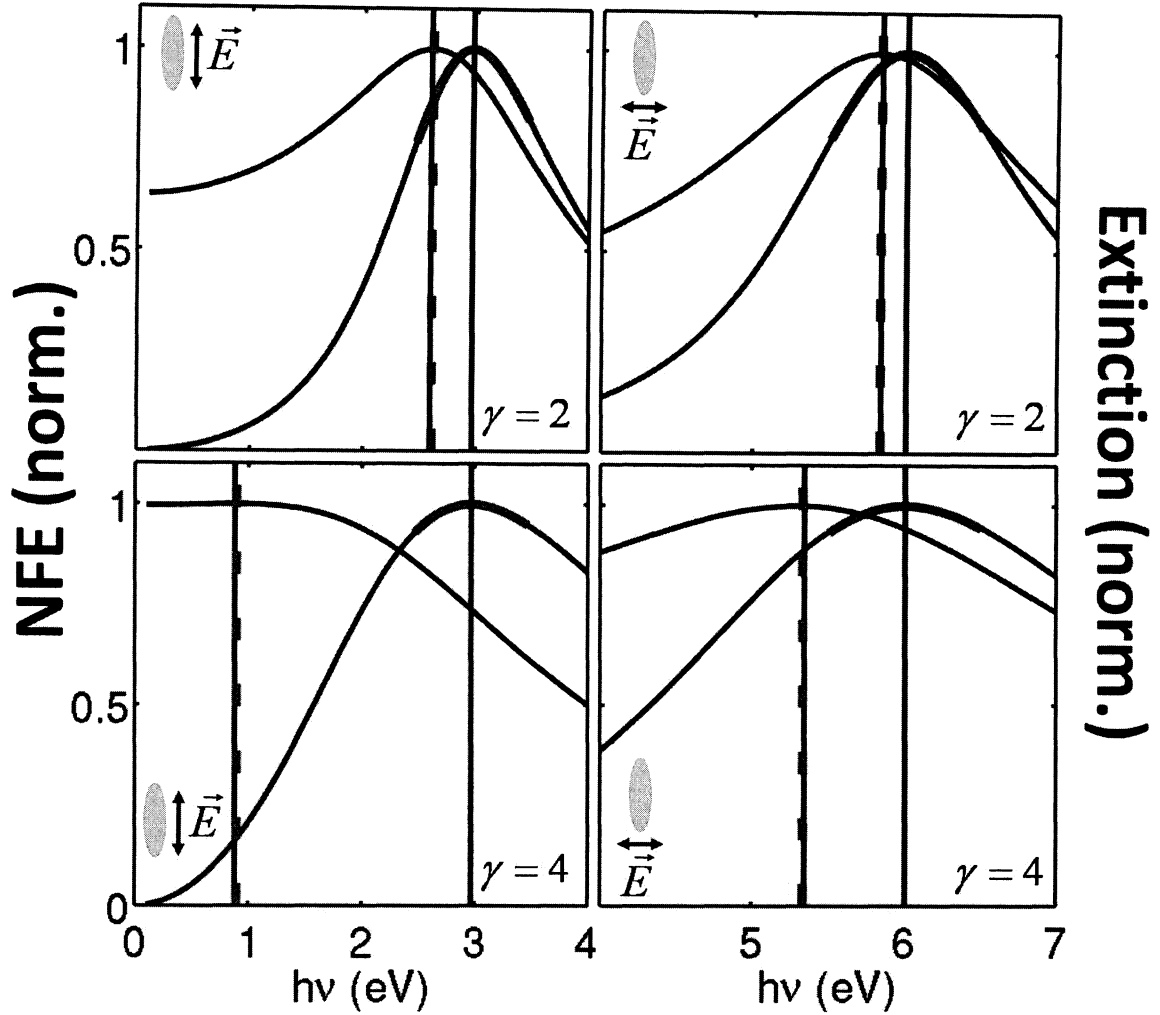


Figure 8.3: Extinction cross section (blue) and NFE (black) as a function of energy for a metallic nanorod of aspect ratio 3 for longitudinal polarization (left panels) and transverse polarization (right panels). DMs with artificially large damping are used: $\gamma = 2$ (top panels), $\gamma = 4$ (bottom panels). The fits of the far-field peaks to Eq. (8.7) are shown in red. The vertical black and blue lines denote the peak positions for the calculated near-field and far-field, respectively. The red dashed lines denote the energy ω_{NF} obtained using Eq. (8.5). The spectra have been normalized to unity.

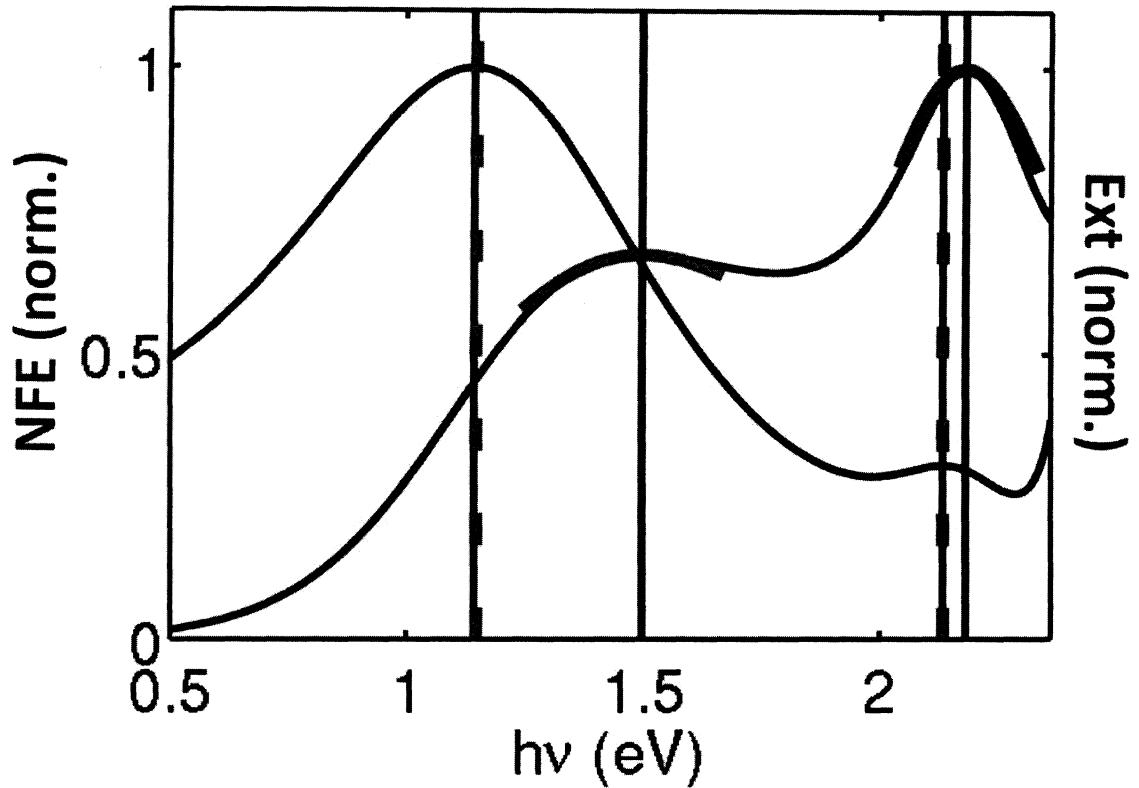


Figure 8.4: Mie extinction spectra (blue) and NFE (black) as a function of energy for a gold (DM) nanoshell of inner radius 75 nm and outer radius 150 nm. The fits of the far-field peak to Eq. (8.7) are shown in red. The vertical black and blue lines denote the near-field and extinction peak energies, respectively. The red dashed line denote the energy ω_{NF} obtained using Eq. (8.5) The spectra have been normalized to unity.

two peaks that are redshifted compared to the far-field spectrum. As in Figures 8.2 and 8.3, the line shape of the extinction resonances in Fig.8.4 is fitted with the HO result, eq. 8.7 (red curves). The dashed red lines show that the predicted NFE peaks obtained using Eq. (8.5) are in excellent agreement with the NFE peaks obtained from full electromagnetic simulations.

In conclusion, using a simple analytical harmonic oscillator model, we have explained why the the near-field spectra of plasmonic nanoparticles are redshifted compared to their far-field spectra. We have shown how this phenomenon is a direct consequence of the fundamental properties of damped, driven harmonic oscillators, and how, using such a model, one can quantitatively predict the magnitude of this shift. This physical insight into the behavior of plasmonic systems should be useful for the practical design of plasmonic nanoparticles and nanostructures for applications of both fundamental and technological interest.

References

- [1] I. Freestone, N. Meeks, M. Sax, and C. Higgitt, “The lycurgus cup – a roman nanotechnology,” *Gold Bulletin*, vol. 40, pp. 270–277, 2007. 1
- [2] A. P. Alivisatos, “Semiconductor clusters, nanocrystals, and quantum dots,” *Science*, vol. 271, pp. 933–937, 1996. 1
- [3] U. Kreibig and M. Vollmer, *Optical properties of metal clusters*. New York: Springer, 1995. 1
- [4] C. Bohren and D. Huffman, *Absorption and scattering of light by small particles*. New York: John Wiley & Sons, Ltd., 1983. 1
- [5] G. Mie, “Beitrge zur optik trber medien, speziell kolloidaler metallungen,” *Ann. Phys.*, vol. 25, p. 377, 1908. 1
- [6] A. L. Aden and M. Kerker, “Scattering of electromagnetic waves from two concentric spheres,” *J. Appl. Phys.*, vol. 22, pp. 1242–1246, 1951. 1, 2.3.1
- [7] A. E. Neeves and M. H. Birnboim, “Composite structures for the enhancement of nonlinear optical susceptibility,” *J. Opt. Soc. Am. B*, vol. 6, pp. 787–796, 1989. 1, 2.3.1
- [8] D. Sarkar and N. J. Halas, “General vector basis function solution of maxwell’s equations,” *Phys. Rev. E*, vol. 56, pp. 1102–1112, 1997. 1, 2.3.1
- [9] E. Prodan and P. Nordlander, “Exchange and correlation effects in small metallic nanoshells,” *Chem. Phys. Lett.*, vol. 349, pp. 153–160, 2001. 1
- [10] E. Prodan and P. Nordlander, “Electronic structure and polarizability of metallic nanoshells,” *Chem. Phys. Lett.*, vol. 352, pp. 140–146, 2002. 1
- [11] J. Zuloaga, E. Prodan, and P. Nordlander, “Quantum plasmonics: Optical properties and tunability of metallic nanorods,” *ACS Nano*, vol. 4, pp. 5269–5276, 2010. 1, 4

-
- [12] J. Zuloaga, E. Prodan, and P. Nordlander, “Quantum description of the plasmon resonances of a nanoparticle dimer,” *Nano Lett.*, vol. 9, pp. 887–891, 2009. 1, 2.2
- [13] H. Hohenberg and W. Kohn *Phys. Rev. B*, vol. 136, p. 864, 1964. 2.1, 2.2
- [14] W. Kohn and L. J. Sham *Phys. Rev. A*, vol. 140, p. 1133, 1965. 2.2, 2.2
- [15] M. J. Puska and R. M. Nieminen, “Photoadsorption of atoms inside c_{60} ,” *Phys. Rev. A*, vol. 47, pp. 1181–1186, 1993. 2.2
- [16] M. J. Puska, R. M. Nieminen, and M. Manninen, “Electronic polarizability of small metal spheres,” *Phys. Rev. B*, vol. 31, pp. 3486–3495, 1985. 2.2
- [17] W. Ekardt, “Work function of small metal particles: Self-consistent spherical jellium-background model,” *Phys. Rev. B*, vol. 29, pp. 1588–1564, 1984. 2.2
- [18] M. J. Stott and E. Zaremba, “Linear-response theory within the density-functional formalism: Application to atomic polarizabilities,” *Phys. Rev. A*, vol. 21, pp. 12–23, 1980. 2.2
- [19] O. Gunnarsson and B. Lundqvist, “Exchange and correlation in atoms, molecules, and solids by the spin-density-functional formalism,” *Phys. Rev. B*, vol. 13, p. 4274, 1976. 2.2
- [20] J. P. Perdew and A. Zunger, “Self-interaction correction to density-functional approximations for many-electron systems,” *Phys. Rev. B*, vol. 23, pp. 5048–5079, 1981. 2.2
- [21] R. D. Averitt, D. Sarkar, and N. J. Halas, “Plasmon resonance shifts of au coated au_2s nanoshells: Insight into multicomponent nanoparticle growth,” *Phys. Rev. Lett.*, vol. 78, pp. 4217–4220, 1997. 2.3.1
- [22] S. Oldenburg, R. D. Averitt, S. Westcott, and N. J. Halas, “Nanoengineering of optical resonances,” *Chem. Phys. Lett.*, vol. 288, pp. 243–247, 1998. 2.3.1, 4
- [23] J. B. Jackson and N. J. Halas, “Silver nanoshells: Variations in morphologies and optical properties,” *J. Phys. Chem. B*, vol. 105, pp. 2743–2746, 2001. 2.3.1
- [24] C. Graf and A. van Blaaderen, “Metallo-dielectric core-shell particles for photonic applications,” *Langmuir*, vol. 18, pp. 524–534, 2002. 2.3.1
- [25] Y. Sun, B. T. Mayers, and Y. Xia, “Template-engaged replacement reaction: A one step approach to the large scale synthesis of metal nanostructures with hollow interiors,” *Nano Lett.*, vol. 2, pp. 481–485, 2002. 2.3.1
- [26] S. J. Oldenburg, J. B. Jackson, S. L. Westcott, and N. J. Halas, “Infrared extinction properties of gold nanoshells,” *Appl. Phys. Lett.*, vol. 75, pp. 2897–2899, 1999. 2.3.1

-
- [27] J. B. Jackson, S. L. Westcott, L. R. Hirsch, J. L. West, and N. J. Halas, "Controlling the surface enhanced raman effect via the nanoshell geometry," *Appl. Phys. Lett.*, vol. 82, pp. 257–259, 2003. 2.3.1
- [28] Y. Sun and Y. Xia, "Increased sensitivity of surface plasmon resonance of gold nanoshells compared to that of gold solid colloids in response to environmental changes," *Anal. Chem.*, vol. 74, pp. 5297–5305, 2002. 2.3.1
- [29] S. Sershen, S. L. Westcott, N. J. Halas, and J. L. West, "Temperature-sensitive polymer-nanoshell composites for photothermally modulated drug delivery," *J. Biomed. Mat. Res.*, vol. 51, pp. 293–298, 2000. 2.3.1, 6.1
- [30] S. Sershen, S. L. Westcott, J. L. West, and N. J. Halas, "An opto-mechanical nanoshell-polymer composite," *Appl. Phys. B*, vol. 73, pp. 379–381, 2001. 2.3.1, 6.1
- [31] G. D. Hale, J. B. Jackson, O. E. Shmakova, T. R. Lee, and N. J. Halas, "Enhancing the active lifetime of luminescent semiconducting polymers via doping with metal nanoshells," *Appl. Phys. Lett.*, vol. 78, pp. 1502–1504, 2001. 2.3.1, 6.1
- [32] E. Prodan, P. Nordlander, and N. J. Halas, "Electronic structure and optical properties of gold nanoshells," *Nano Lett.*, vol. 3, pp. 1411–1415, 2003. 2.3.1, 2.3.2, 4.1, 4.1, 4.2
- [33] E. Prodan and P. Nordlander, "Structural tunability of the plasmon resonances in metallic nanoshells," *Nano Lett.*, vol. 3, pp. 543–547, 2003. 2.3.1, 4, 4.1, 4.3
- [34] H. W. Liao and J. H. Hafner, "Monitoring gold nanorod synthesis on surfaces," *J. Phys. Chem. B*, vol. 108, pp. 19276–19280, 2004. 2.3.2
- [35] A. Gulati and J. H. Hafner, "Monitoring gold nanorod synthesis by localized surface plasmon resonance," *J. Phys. Chem. B*, vol. 110, pp. 22323–22327, 2006. 2.3.2
- [36] A. Lee, G. F. S. Andrade, A. Ahmed, M. L. Souza, N. Coombs, E. Tumarkin, K. Liu, R. Gordon, A. G. Brolo, and E. Kumacheva, "Probing dynamic generation of hot-spots in self-assembled chains of gold nanorods by surface-enhanced raman scattering," *J. Am. Chem. Soc.*, vol. 133, pp. 7563–7570, 2011. 2.3.2
- [37] V. Schweikhard, A. Grubisic, T. A. Baker, I. Thomann, and D. J. Nesbitt, "Polarization-dependent scanning photoionization microscopy: Ultrafast plasmon-mediated electron ejection dynamics in single au nanorods," *ACS Nano*, vol. 5, pp. 3724–3735, 2011. 2.3.2
- [38] F. Neubrech, A. Garcia-Extarri, D. Weber, J. Bochterle, H. Shen, M. L. de la Chapelle, G. W. Bryant, J. Aizpurua, and A. Pucci, "Defect-induced activation

- of symmetry forbidden infrared resonances in individual metallic nanorods,” *Appl. Phys. Lett.*, vol. 96, p. 213111, 2010. 2.3.2
- [39] A. Mohammadi, V. Sandoghdar, and M. Agio, “Gold nanorods and nanospheroids for enhancing spontaneous emission,” *New. J. Phys.*, vol. 10, p. 105015, 2008. 2.3.2, 4
- [40] X. Huang, P. K. Jain, I. H. El-Sayed, and M. A. El-Sayed, “Gold nanoparticles and nanorods in medicine: From cancer diagnostics to photothermal therapy,” *Nanomedicine*, vol. 2, pp. 681–693, 2007. 2.3.2
- [41] J. Perez-Juste, I. Pastoriza-Santos, L. M. Liz-Marzan, and P. Mulvaney, “Gold nanorods: Synthesis, characterization and applications,” *Coord. Chem. Rev.*, vol. 249, pp. 1870–1901, 2005. 2.3.2, 4
- [42] H. Wang, Y. Wu, B. Lassiter, C. L. Nehl, J. H. Hafner, P. Nordlander, and N. J. Halas, “Symmetry-breaking in individual plasmonic nanoparticles,” *Proc. Natl. Acad. Sci. USA*, vol. 103, pp. 10856–10860, 2006. 2.3.2, 6.1
- [43] C. Charnay, A. Lee, S.-Q. Man, C. E. Moran, C. Radloff, R. K. Bradley, and N. J. Halas, “Reduced symmetry metallodielectric nanoparticles: Chemical synthesis and plasmonic properties,” *J. Phys. Chem. B.*, vol. 107, pp. 7327–7333, 2003. 2.3.2, 6.1
- [44] J. Liu, B. Cankurtaran, L. Wieczorek, M. J. Ford, and M. Cortie, “Anisotropic optical properties of semitransparent coatings of gold nanocaps,” *Adv. Funct. Mater.*, vol. 16, pp. 1457–1461, 2006. 2.3.2
- [45] J. Liu, A. I. Maarroof, L. Wieczorek, and M. Cortie, “Fabrication of hollow metal nanocaps and their red-shifted optical absorption spectra,” *Adv. Mater.*, vol. 17, pp. 1276–1281, 2005. 2.3.2
- [46] J. Liu, B. Cankurtaran, G. McCreddie, M. Ford, L. Wieczorek, and M. Cortie, “Investigation of the optical properties of hollow aluminium nano-caps,” *Nanotechnology*, vol. 16, pp. 3023–3028, 2005. 2.3.2
- [47] J. B. Lassiter, J. Aizpurua, L. I. Hernandez, D. W. Brandl, I. Romero, S. Lal, J. H. Hafner, P. Nordlander, and N. Halas, “Close encounters between two nanoshells,” *Nano Lett.*, vol. 8, pp. 1212–1218, 2008. 2.3.2, 5, 5.1, 5.1
- [48] L. S. Slaughter, Y. P. Wu, B. A. Willingham, P. Nordlander, and S. Link, “Effects of symmetry breaking and conductive contact on the plasmon coupling in gold nanorod dimers,” *ACS Nano*, vol. 4, p. 4657–4666, 2010. 2.3.2
- [49] J. I. L. Chen, Y. Chen, and D. S. Ginger, “Plasmonic nanoparticle dimers for optical sensing of dna in complex media,” *J. Am. Chem. Soc.*, vol. 132, pp. 9600–9601, 2010. 2.3.2

-
- [50] L. Shao, K. C. Woo, H. Chen, Z. Jin, J. Wang, and H. Q. Lin, "Angle- and energy-resolved plasmon coupling in gold nanorod dimers," *ACS Nano*, vol. 4, pp. 3053–3062, 2010. 2.3.2
- [51] M. Rycenga, P. H. C. Camargo, W. Li, C. H. Moran, and Y. Xia, "Understanding the sers effects of single silver nanoparticles and their dimers, one at a time," *J. Phys. Chem. Lett.*, vol. 1, pp. 696–703, 2010. 2.3.2
- [52] M. S. Stewart, C. Qiu, R. Kattumenu, S. Singamaneni, and C. Jiang, "Diameter-dependent coloration of silver nanowires," *Nanotechnology*, vol. 22, p. 275712, 2011. 2.3.2
- [53] T. Shegai, V. D. Miljkovic, K. Bao, H. X. Xu, P. Nordlander, P. Johansson, and M. Kall, "Unidirectional broadband light emission from supported plasmonic nanowires," *Nano Lett.*, vol. 11, pp. 706–711, 2011. 2.3.2
- [54] D. Solis, W. S. Chang, B. P. Khanal, K. Bao, P. Nordlander, E. R. Zubarev, and S. Link, "Bleach-imaged plasmon propagation (blipp) in single gold nanowires," *Nano Lett.*, vol. 10, pp. 3482–3485, 2010. 2.3.2
- [55] D. A. Clayton, D. M. Benoist, Y. Zhu, and S. Pan, "Photoluminescence and spectroelectrochemistry of single ag nanowires," *ACS Nano*, vol. 4, pp. 2363–2373, 2010. 2.3.2
- [56] K. Wang and D. M. Mittleman, "Dispersion of surface plasmon polaritons on metal wires in the terahertz frequency range," *Phys. Rev. Lett.*, vol. 96, p. 157401, 2006. 2.3.2
- [57] H. Y. Chung, P. T. Leung, and D. P. Tsai, "Enhanced intermolecular energy transfer in the vicinity of a plasmonic nanorice," *Plasmonics*, vol. 5, pp. 363–368, 2010. 2.3.2
- [58] H. Wei, A. Reyes-Coronado, P. Nordlander, J. Aizpurua, and H. X. Xu, "Multipolar plasmon resonances in individual ag nanorice," *ACS Nano*, vol. 4, pp. 2649–2654, 2010. 2.3.2, 4.1
- [59] H. Wang, D. W. Brandl, F. Le, P. Nordlander, and N. J. Halas, "Nanorice: A hybrid plasmonic nanostructure," *Nano Lett.*, vol. 6, pp. 827–832, 2006. 2.3.2
- [60] Y. Saad, *Iterative Methods for Sparse Linear Systems*. Philadelphia, USA: SIAM, 2003. 3.2
- [61] B. E. Brinson, J. B. Lassiter, C. S. Levin, R. Bardhan, N. Mirin, and N. J. Halas, "Nanoshells made easy: Improving au layer growth on nanoparticle surfaces," *Langmuir*, vol. 24, pp. 14166–14171, 2008. 4, 6.1

-
- [62] T. C. Preston and R. Signorell, "Growth and optical properties of gold nanoshells prior to the formation of a continuous metallic layer," *ACS Nano*, vol. 3, pp. 3696–3706, 2009. 4
- [63] B. Storti, F. Elisei, S. Abbruzzetti, C. Viappiani, and L. Latterini, "One-pot synthesis of gold nanoshells with high photon-to-heat conversion efficiency," *J. Phys. Chem. C*, vol. 113, pp. 7516–7521, 2009. 4
- [64] M. A. Ochsenkuhn, P. R. T. Jess, H. Stoquert, K. Dholakia, and C. J. Campbell, "Nanoshells for surface-enhanced raman spectroscopy in eukaryotic cells: Cellular response and sensor development," *ACS Nano*, vol. 3, pp. 3613–3621, 2009. 4
- [65] S. Link, M. B. Mohamed, and M. A. El-Sayed, "Simulation of the optical absorption spectra of gold nanorods as a function of their aspect ratio and the effect of the medium dielectric constant," *J. Phys. Chem. B*, vol. 103, pp. 3073–3077, 1999. 4, 4.1, 4.1
- [66] C. Tserkezis, N. Papanikolaou, E. Almpanis, and N. Stefanou, "Tailoring plasmons with metallic nanorod arrays," *Phys. Rev. B*, vol. 80, p. 125124, 2009. 4
- [67] Y. F. Chau, M. W. Chen, and D. P. Tsai, "Three-dimensional analysis of surface plasmon resonance modes on a gold nanorod," *Appl. Optics*, vol. 48, pp. 617–622, 2009. 4
- [68] H. W. Liao, C. L. Nehl, and J. H. Hafner, "Biomedical applications of plasmon resonant metal nanoparticles," *Nanomedicine*, vol. 1, pp. 201–208, 2006. 4
- [69] S. Lal, S. Link, and N. J. Halas, "Nano-optics from sensing to waveguiding," *Nature Phot.*, vol. 1, pp. 641–648, 2007. 4
- [70] S. Lal, S. E. Clare, and N. J. Halas, "Nanoshell-enabled photothermal cancer-therapy: Impending clinical impact," *Acct. Chem. Res.*, vol. 41, pp. 1842–1851, 2008. 4
- [71] V. Myroshnychenko, J. Rodrigues-Fernandez, I. Pastoriza-Santos, A. M. Funston, C. Novo, P. Mulvaney, L. M. Liz-Marzan, and F. J. G. de Abajo, "Modelling the optical response of gold nanoparticles," *Chem. Soc. Rev.*, vol. 37, pp. 1792–1805, 2008. 4
- [72] E. M. Perassi, J. C. Hernandez-Garrido, M. S. Moreno, E. R. Encina, E. A. Coronado, and P. A. Midgley, "Using highly accurate 3d nanometrology to model the optical properties of highly irregular nanoparticles: A powerful tool for rational design of plasmonic devices," *Nano Lett.*, vol. 10, pp. 2097–2104, 2010. 4

-
- [73] E. Prodan, A. Lee, and P. Nordlander, "The effect of a dielectric core and embedding medium on the polarizability of metallic nanoshells," *Chem. Phys. Lett.*, vol. 360, pp. 325–332, 2002. 4
- [74] E. Prodan, P. Nordlander, and N. J. Halas, "Effects of dielectric screening on the optical properties of metallic nanoshells," *Chem. Phys. Lett.*, vol. 368, pp. 94–101, 2003. 4
- [75] T. Atay, J. H. Song, and A. V. Nurmikko, "Strongly interacting plasmon nanoparticle pairs: From dipole-dipole interaction to conductively coupled regime," *Nano Lett.*, vol. 4, pp. 1627–1631, 2004. 5
- [76] M. Danckwerts and L. Novotny, "Optical frequency mixing at coupled gold nanoparticles," *Phys. Rev. Lett.*, vol. 98, p. 026104, 2007. 5
- [77] I. Romero, J. Aizpurua, G. W. Bryant, and F. J. G. de Abajo, "Plasmons in nearly touching metallic nanoparticles: Singular response in the limit of touching dimers," *Opt. Express*, vol. 14, pp. 9988–9999, 2006. 5, 5.1
- [78] L. L. Yang, B. Yan, and B. M. Reinhard, "Correlated optical spectroscopy band transmission electron microscopy of individual hollow nanoparticles and their dimers," *J. Phys. Chem. C*, vol. 112, pp. 15989–15996, 2008. 5
- [79] A. O. Pinchuk and G. C. Schatz, "Collective surface plasmon resonance coupling in silver nanoshell arrays," *Appl. Phys. B*, vol. 93, pp. 31–38, 2008. 5
- [80] T. Hartling, Y. Alaverdyan, A. Hille, M. T. Wenzel, M. Kall, and L. M. Eng, "Optically controlled interparticle distance tuning and welding of single gold nanoparticle pairs by photochemical deposition," *Optics Expr.*, vol. 16, pp. 12362–12371, 2008. 5
- [81] G. H. Gu and J. S. Suh, "Enhancement at the junction of silver nanorods," *Langmuir*, vol. 24, pp. 8934–8938, 2008. 5
- [82] M. Mugisawa and H. Sawada, "Architecture of linear arrays of fluorinated co-oligomeric nanocomposite-encapsulated gold nanoparticles: A new approach to the development of gold nanoparticles possessing an extremely red-shifted absorption characteristic," *Langmuir*, vol. 24, pp. 9215–9218, 2008. 5
- [83] K. Imura, H. Okamoto, M. K. Hossain, and M. Kitajima, "Visualization of localized intense optical fields in single gold-nanoparticle assemblies and ultra-sensitive raman active sites," *Nano Lett.*, vol. 6, pp. 2173–2176, 2006. 5
- [84] P. K. Jain and M. A. El-Sayed, "Noble metal nanoparticle pairs: Effect of medium for enhanced nanosensing," *Nano Lett.*, vol. 8, pp. 4347–4352, 2008. 5
- [85] M. Pelton, J. Aizpurua, and G. W. Bryant, "Metal-nanoparticle plasmonics," *Laser and Photon. Rev.*, vol. 2, pp. 136–159, 2008. 5

-
- [86] A. Alu and N. Engheta, "Hertzian plasmonic nanodimer as an efficient optical nanoantenna," *Phys. Rev. B*, vol. 78, p. 195111, 2008. 5
- [87] H. Ko, S. Singamaneni, and V. V. Tsukruk, "Nanostructured surfaces and assemblies as sers media," *Small*, vol. 4, pp. 1576–1599, 2008. 5
- [88] N. G. Khlebtsov, "Optics and biophotonics of nanoparticles with a plasmon resonance," *Quantum Electronics*, vol. 38, pp. 504–529, 2008. 5
- [89] J. K. Ghosh and T. Pal, "Interparticle coupling effect: on the surface plasmon resonance of gold nanoparticles: From theory to applications," *Chem. Rev.*, vol. 107, pp. 4797–4862, 2007. 5
- [90] P. Olk, J. Renger, M. T. Wenzel, and L. M. Eng, "Distance dependent spectral tuning of two coupled metal nanoparticles," *Nano Lett.*, vol. 8, pp. 1174–1178, 2008. 5
- [91] I. A. Larkin and M. I. Stockman, "Imperfect perfect lens," *Nano Lett.*, vol. 5, pp. 339–343, 2005. 5
- [92] E. Prodan and R. Car, "Tunneling conductance of amine-linked alkyl chains," *Nano Lett.*, vol. 8, pp. 1771–1777, 2008. 5
- [93] F. J. G. de Abajo, "Nonlocal effects in the plasmon of strongly interacting nanoparticles, dimers and waveguides," *J. Phys. Chem. C*, vol. 112, pp. 17983–17987, 2008. 5
- [94] P. Nordlander, C. Oubre, E. Prodan, K. Li, and M. I. Stockman, "Plasmon hybridization in nanoparticle dimers," *Nano Lett.*, vol. 4, pp. 899–903, 2004. 5, 5.1, 5.1
- [95] P. Nordlander and J. C. Tully, "Energy shifts and broadening of atomic levels outside metal surfaces," *Phys. Rev. B*, vol. 42, pp. 5564–5578, 1990. 5.2
- [96] M. W. Knight and N. J. Halas, "Nanoshells to nanoeggs to nanocups: Optical properties of reduced symmetry core-shell nanoparticles beyond the quasistatic limit," *New. J. Phys.*, vol. 10, p. 105006, 2008. 6.1, 6.1, 6.1
- [97] Y. P. Wu and P. Nordlander, "Plasmon hybridization in nanoshells with a nonconcentric core," *J. Chem. Phys.*, vol. 125, p. 124708, 2006. 6.1
- [98] D.-K. Lim, K.-S. Jeon, J.-H. Hwang, H. Kim, S. Kwon, Y. D. Suh, and J.-M. Nam, "Highly uniform and reproducible surface-enhanced raman scattering from dna-tailorable nanoparticles with 1-nm interior gap," *Nature Nanotech.*, vol. 6, pp. 452–460, 2011. 6.2

-
- [99] N. K. Grady, N. J. Halas, and P. Nordlander, "Influence of the dielectric function properties on the optical response of plasmon resonant metallic nanoparticles," *Chem. Phys. Lett.*, vol. 399, pp. 167–171, 2004. 8.1, 8.2
- [100] A. S. Grimault, A. Vial, and M. L. de la Chapelle, "Modeling of regular gold nanostructure arrays for sers applications using a 3d fdtd method," *Appl. Phys. B*, vol. 84, pp. 111–115, 2006. 8.1
- [101] S. Bruzzone, M. Malvaldi, G. P. Arrighini, and C. Guidotti, "Near-field and far-field scattering by bimetallic nanoshell systems," *J. Phys. Chem. B*, vol. 110, pp. 11050–11054, 2006. 8.1
- [102] K. L. Kelly, E. Coronado, L. L. Zhao, and G. C. Schatz, "The optical properties of metal nanoparticles: The influence of size, shape, and dielectric environment," *J. Phys. Chem. B*, vol. 107, pp. 668–677, 2003. 8.1
- [103] G. W. Bryant, F. J. G. de Abajo, and J. Aizpurua, "Mapping the plasmon resonances of metallic nanoantennas," *Nano Lett.*, vol. 8, pp. 631–636, 2008. 8.1
- [104] B. M. Ross and L. P. Lee, "Comparison of near- and far-field measures for plasmon resonance of metallic nanoparticles," *Opt. Lett.*, vol. 34, pp. 896–898, 2009. 8.1
- [105] E. Prodan and P. Nordlander, "Plasmon hybridization in spherical nanoparticles," *J. Chem. Phys.*, vol. 120, pp. 5444–5454, 2004. 8.1, 8.2
- [106] T. Ambjornsson, G. Mukhopadhyay, S. P. Apell, and M. Kall, "Resonant coupling between localized plasmons and anisotropic molecular coatings in ellipsoidal metal nanoparticles," *Phys. Rev. B*, vol. 73, p. 085412, 2006. 8.1
- [107] N. Liu, H. Guo, L. Fu, S. Kaiser, H. Schweizer, and H. Giessen, "Plasmon hybridization in stacked cut-wire metamaterials," *Adv. Mater.*, vol. 19, pp. 3628–3632, 2007. 8.1
- [108] N. Liu, S. Kaiser, and H. Giessen, "Magnetoinductive and electroinductive coupling in plasmonic metamaterial molecules," *Adv. Mat.*, vol. 20, pp. 4521–4525, 2008. 8.1
- [109] A. Moradi, "Plasmon hybridization in metallic nanotubes," *J. Phys. Chem. Solids*, vol. 69, pp. 2936–2938, 2008. 8.1
- [110] N. Liu, L. Langguth, T. Weiss, J. Kastel, M. Fleischhauer, T. Pfau, and H. Giessen, "Plasmonic analogue of electromagnetically induced transparency at the drude damping limit," *Nature Mat.*, vol. 8, pp. 758–762, 2009. 8.1

-
- [111] M. D. Turner, M. M. Hossain, and M. Gu, “The effects of retardation on plasmon hybridization within metallic nanostructures,” *New. J. Phys.*, vol. 12, p. 083062, 2010. 8.1
- [112] H. Liu, T. Li, S. M. Wang, and S. N. Zhu, “Hybridization effect in coupled metamaterials,” *Frontiers of Physics in China*, vol. 5, pp. 277–290, 2010. 8.1
- [113] T. J. Davis, D. E. Gomez, and K. C. Vernon, “Simple model for the hybridization of surface plasmon resonances in metallic nanoparticles,” *Nano Lett.*, vol. 10, pp. 2618–2625, 2010. 8.1
- [114] S. C. Yang, H. Kobori, C. L. He, M. H. Lin, H. Y. Chen, C. Li, M. Kanehara, T. Teranishi, and S. Gwo, “Plasmon hybridization in individual gold nanocrystal dimers: Direct observation of bright and dark modes,” *Nano Lett.*, vol. 10, pp. 632–637, 2010. 8.1
- [115] C. Radloff and N. J. Halas, “Plasmonic properties of concentric nanoshells,” *Nano Lett.*, vol. 4, pp. 1323–1327, 2004. 8.2